

Periodic Surface Modification by Femtosecond Laser Irradiation on Semiconductors

by

Rico S. Cahyadi

A dissertation submitted in partial fulfillment
of the requirements for the degree of
Doctor of Philosophy
(Materials Science and Engineering)
in The University of Michigan
2017

Doctoral Committee:

Professor Steven M. Yalisove, Chair
Assistant Professor John T. Heron
Professor Theodore B. Norris
Research Scientist Ben Torralva

Rico S. Cahyadi

ricobasc@umich.edu

ORCID iD: 0000-0002-1054-5368

© Rico S. Cahyadi 2017

All Rights Reserved

To my parents, Ali and Yani Cahyadi

ACKNOWLEDGEMENTS

I would like to thank my family and friends for their support during my time here at Ann Arbor. I specifically thank my advisor, Steve Yalisove, for his patience and optimism in guiding me through my doctoral study. Special thanks to Ben Torralva, for the numerous discussions in physics which I learn a lot from. To my colleagues, Keegan Schrider and Michael Abere, thank you for showing me the ins and outs of graduate research. I'm grateful for all the time we spent scratching our heads together. Finally, I would like to thank Haiping Sun for the numerous instrument trainings at MC² and Nadine Wang for all the help at LNF.

TABLE OF CONTENTS

DEDICATION	ii
ACKNOWLEDGEMENTS	iii
LIST OF FIGURES	vii
LIST OF APPENDICES	ix
ABSTRACT	x
CHAPTER	
I. Introduction	1
II. Literature Review	5
2.1 Ultrafast Laser Interaction with Matter	5
2.1.1 Ultrafast Laser Induced Structural Dynamics	8
2.1.2 Drude model	10
2.2 Laser Induced Periodic Surface Structures	11
2.2.1 Sipe Theory	11
2.2.2 LSFL Formation Mechanisms	13
2.2.3 HSFL Formation Mechanisms	14
2.3 Review on Relevant Optics	16
2.3.1 Fresnel Equations	16
2.3.2 Surface Plasmon Polariton Field	18
III. Experimental Details and Methods	21
3.1 Characterization of the Ultrafast Laser Beam Parameters	21
3.2 Focusing Conditions and The Rayleigh Length	23
3.3 The Definition and Determination of Damage Thresholds	24
3.4 Frequency Doubling of the Ti:Sapphire Laser	26

3.5	Sample Preparation and Parameters	29
3.5.1	Gold Mesa Samples	29
3.5.2	Silicon Step-Edge Samples	30
3.5.3	Chemical Etching of Samples	31
3.6	Vacuum Irradiation	32
3.7	Finite Element Frequency Domain Field Calculations	33
IV.	Ultrafast Laser Self-Interference with Concurrently Induced Surface Plasmon Polariton Field	36
4.1	Ultrafast Dynamics during Ultrafast Laser Irradiation on Silicon	37
4.1.1	Impact Ionization Contribution	39
4.1.2	Optical Properties of the Excited Surface	40
4.1.2.1	Free Carrier Response	40
4.1.2.2	Nonlinear Effects	42
4.1.2.3	Effective Absorption	43
4.1.3	Carrier Temperature	43
4.1.4	0-Dimensional Ultrafast Dynamics Simulation	45
4.2	SPP-Laser Interference Formalism	47
4.2.1	Laser Incidence Angle Dependence of LSFL Formation	49
4.3	Results and Discussions	50
4.3.1	Parameters at Silicon Melt Threshold	50
4.3.2	Angle Dependent LSFL Formation: Experimental Results	52
4.3.3	Angle Dependent LSFL Formation: Comparison with Theoretical Model	54
V.	Control and Mechanisms of Low Spatial Frequency Laser Induced Periodic Surface Structures Formation using Plasmonic Microstructures	59
5.1	TM Polarized Irradiations of Gold Mesa on Silicon	60
5.1.1	Periodicity Analysis	61
5.1.2	TM Irradiation Frequency Domain Simulation	63
5.1.3	SPP Coupling Mechanism on the Step Edge Structure	65
5.1.4	Specular Phase Matching Condition	67
5.2	TE Polarized Irradiations of Gold Mesa on Silicon	68
5.2.1	TE Irradiation Frequency domain Simulation	70
5.3	Fluence Dependence of the Formed LSFL Wavelength	72
5.4	2-Dimensional Periodic Structure Formations	75
5.4.1	Multiple SPP-Laser Interference	76
VI.	High Spatial Frequency Laser Induced Periodic Surface Structure Formation in Silicon: Laser Coupling with Point Defect Induced Islands	81

6.1	The Effect of Wavelength	82
6.1.1	Point Defect Generation	84
6.2	Modified Silicon Surface Morphologies in Vacuum	86
6.2.1	The Region of Silicon HSFL Formation	88
6.2.2	Island Growth and Bifurcation	90
6.2.3	The Influence of Silicon Native Oxide	94
6.3	HSFL Formation Mechanism: Sipe Model Interpretation	95
VII. Summary and Future Work		100
7.1	Structural Characterization of HSFL Formation on Silicon	102
7.2	Laser Induced Oxidation	103
7.3	HSFL Formation in Wide Band Gap Semiconductors: The Role of Coulomb Explosion	106
APPENDICES		109
BIBLIOGRAPHY		125

LIST OF FIGURES

Figure

2.1	Timescale of ultrafast laser-matter interaction	6
2.2	Surface roughness model within the Sipe Theory	12
2.3	Angle dependent reflectivity of silicon at 780 nm	17
2.4	Coupled TM field on a metal-dielectric interface	18
3.1	Silicon ablation and melt threshold curve at 780 nm	25
3.2	Calculated parameters for second harmonic generation with BBO	27
3.3	BBO crystal dimension and orientation	28
3.4	Experimental setup for frequency doubled beam	29
3.5	Gold mesa shapes and cross-section diagram	30
3.6	Vacuum irradiation setup	33
3.7	COMSOL simulation setup	35
4.1	Irradiation dynamics calculation diagram	45
4.2	SPP laser interference diagram	47
4.3	Calculated parameters at the threshold fluence of melt	51
4.4	Optical images of LSFL formation at various incidence angles	53
4.5	Active interference area and effective fluence definition	54
4.6	SPP wavelength map in the complex permittivity plane	56
4.7	LSFL wavelengths at various incident beam angles	57
5.1	LSFL formation on gold mesa on silicon using TM polarized beam	60
5.2	LSFL period distributions of 720 nm and 110 nm tall mesa TM-polarized irradiations	62
5.3	Gold mesa TM irradiation simulation results	64
5.4	SPP coupling mechanisms on gold mesa structures on silicon	65
5.5	Phase matching conditions at various mesa heights	67
5.6	LSFL formation on gold mesa on silicon using TE polarized beam	69
5.7	LSFL period distribution of 720 nm tall mesa TE-polarized irradiation	70
5.8	Gold mesa TE irradiation simulation results	71
5.9	LSFL wavelength dependence on fluence in the case of Au mesa TM irradiations	72
5.10	LSFL wavelength dependence on fluence in the case of Au mesa TE irradiations	74
5.11	Nanojets formation on triangular gold mesa	75

5.12	Periodicity comparison of nanojets formed on triangular gold mesa with multiple SPP-laser interference	77
5.13	Periodicity comparison of nanojets formed on hexagonal and square gold mesas with multiple SPP-laser interference	80
6.1	Silicon damage thresholds and morphologies at 390 nm and 780 nm wavelengths	83
6.2	Laser induced point defect generation scheme	85
6.3	Silicon nanostructure formation across fluences	87
6.4	AFM and FFT analysis of silicon HSFL formation	89
6.5	Stages of islands growth	91
6.6	Bifurcated islands morphology	93
6.7	The effect of pre-etching on islands formation threshold	94
6.8	Efficacy factor maps of silicon at 390 nm	97
6.9	Relative inhomogeneous intensity distribution maps of silicon islands at 390 nm	98
7.1	Cross-sectional TEM analysis of a nanocrystalline HSFL formation above the original surface	102
7.2	Tall Oxide Structure formation on silicon	104
7.3	Silicon island and HSFL formations in air environment	105
7.4	HSFL formation and evolution in SiC using 780 nm laser irradiation	107
7.5	SiC thresholds at 390 nm and 780 nm wavelengths	108

LIST OF APPENDICES

Appendix

A. Derivation of the Electric Field for Surface TM Wave Propagation . . . 110

B. Threshold Regression Curve Algorithm 112

C. 0-Dimensional Silicon Carrier Dynamics Calculation Algorithm 114

D. Fast Fourier Transform and Autocorrelation Algorithms 119

E. Sipe Efficacy Factor Formalism 122

ABSTRACT

Periodic Surface Modification by Femtosecond Laser Irradiation on Semiconductors

by

Rico S. Cahyadi

Chair: Steven M. Yalisove

This thesis focuses on the formation of laser induced periodic surface structures (LIPSS) on semiconductors by ultrafast laser irradiation, specifically on the observation of distinct LIPSS mechanisms and the modeling of its formation dynamics. In order to do so, experiments under various irradiation conditions and material systems were performed, and the subsequent material transformations were characterized using combinations of microscopy and chemical analysis techniques. Finally, the modeling of the irradiation dynamics is done both analytically and using finite element calculations.

The first part of the study discusses the direct involvement of surface plasmon polaritons (SPP) and its interference with the laser field in the early stage of low spatial frequency LIPSS (LSFL) formation. In semiconductors, the SPP mode is supported by a brief metallic state transition during an ultrafast laser pulse irradiation. We further show that the transient dynamics strongly relate to the final characteristics of LSFL being formed.

The second part of the study dwells more into the control of LSFL formation using plasmonic microstructures. Initialization of SPP field using a strong plasmonic

coupler such as gold yields high intensity LSFL formations, which is consistent with the SPP-laser interference mechanism. LSFL intensity and orientation is also shown to be related to the geometry of the microstructures. Further, a variety of 2D periodic surfaces were created using the interference of multiple SPP sources. Finally, near field diffraction is shown to be a dominating mechanism of LSFL formation in the case where SPP coupling is negligible.

The third part of the study analyzes a possible universal mechanism for high spatial frequency LIPSS (HSFL) formation involving point defect generation, diffusion, and accumulation in low band-gap semiconductors. We will examine the effect of laser frequency on possible point defect generation in silicon. Subsequently, we report periodic nanoscale island formation on Silicon previously observed only in compound semiconductors. Island formation is proposed to be the precursor for the subsequent HSFL evolution via light scattering in the near field.

All of the studies outlined above achieve the common goal of highlighting the coupled interplay between optically driven surface modification mechanisms with a dynamically changing material structure and properties under transient strong electromagnetic field. The entirety of which, results in a variety of characteristic periodic modulations on semiconductor surfaces we have come to observe.

CHAPTER I

Introduction

The nature of surface modification of materials under femtosecond laser irradiation has been an ongoing research topic due to the complexity of the cascading processes involved. Through ultrafast laser irradiation, a small amount of fluence on the order of mJ/cm^2 is typically delivered into the material system. Yet, the ultrashort pulse duration of the laser is able to induce a large intensity in the order of $10^{11} - 10^{14} \text{ W}/\text{cm}^2$. As a result, the electronic response of the irradiated materials becomes largely non steady state [1]. A large laser intensity is also able to drive a significant amount of carrier excitation on an otherwise weakly absorbing material such as silicon via nonlinear effects [2]. This, in turn, may lead to further generation of carriers through impact ionization [3] and electron tunneling [4].

As carrier dispersion behavior is modified due to many-body interactions, a material's band gap decreases [4, 5]. Moreover, the promotion of electrons into the anti-bonding states induces destabilization of the lattice structure at room temperature [6], which, at a significant percentage of valence electrons excited (about 10% [7]), leads to the closing of the band gap [8]. As "cold" ions drift from its original lattice space, nonthermal laser melting and point defect generation could occur [6, 9–11]. At a substantially large fluence applied, materials could subsequently be removed via liquid spallation [12, 13] and coulomb explosion [14, 15]. In femtosecond laser

ablation, energy coupling to the lattice occurs rapidly, thereby minimizing collateral thermal damage to the irradiated region surroundings. All of the processes outlined above induce permanent surface modifications to the material. Some, of which, may display periodic characteristics.

In this thesis, we will specifically examine the ultrafast laser-matter interactions leading to the formation of periodic surface structures. These structures are commonly characterized by one dimensional surface modulations with distinct periods near or below the wavelength of the laser, which are often referred to as laser induced periodic surface structures (LIPSS) [16, 17]. LIPSS have been an active field of research due to its ubiquity and complex formation mechanism. However, LIPSS formation dynamics in the ultrafast timescale has not been sufficiently investigated. As such, we attempt to present a comprehensive model of low spatial frequency LIPSS (LSFL) formation using single femtosecond laser pulse irradiations. Our approach is based on the well-known hypothesis of surface plasmon polariton (SPP) excitation and its interference with the incident laser on semiconductors [18, 19]. The result of our analysis further confirms SPP-laser interference to be the dominant formation mechanism of LSFL on semiconductors.

Understanding of the LSFL formation mechanism is essential for its well-controlled fabrication and subsequent future applications. Possible LSFL applications range from metal coloration [20] to superhydrophobic surfaces [21]. Following our investigation on the SPP-laser interference mechanism, we demonstrate engineering control of the LSFL formation using prefabricated gold microstructures on silicon. As field enhancement is induced by SPP coupling on gold, a substantial increase in the formed LSFL intensity is observed. Moreover, by utilizing multiple SPP sources, we are able to form 2 dimensional periodic surface structures on gold in the form of nanojets. In the case where it is unlikely for SPP to be coupled, however, we still observe LSFL formation due to near field diffraction [22]. This result further demonstrates that the

LSFL formation mechanism consists of multiple competing optically driven phenomena, which depend largely on the geometry of the irradiated material's surface.

The formation of high spatial frequency LIPSS (HSFL) on silicon will also be one of the focuses of this thesis. In the current literature, HSFL formation mechanism on semiconductors is still highly under debate [16]. Recent studies have suggested the inclusion of point defect generation and diffusion in the HSFL formation dynamics [10, 11]. The hypothesis is supported by a recent observation of periodic island-like nanostructures formation below the threshold of permanent damage in GaAs, which subsequently evolve into HSFL via light coupling [11]. In our study, we show the extent of island and HSFL formation in silicon, further supporting the argument. In addition, parallels drawn from similar periodic nanostructure formation using ion beam radiation [23, 24] suggests that high stress states may drive the laser induced island formation, which is consistent with the point defect based mechanism. While the evolution of islands into HSFL has been phenomenologically observed, further analysis of its dynamics is still needed. Here, we also present a possible explanation to the islands-HSFL evolution involving inhomogeneous energy absorption [25].

To summarize, the goals of this thesis include:

1. To present a comprehensive model of LSFL formation on semiconductor based on SPP-Laser interference, which includes the relationship between the dynamics of generated electron plasma and the final characteristics of LSFL produced.
2. To demonstrate control over LSFL formation based on the aforementioned model and engineer other possible periodic surface configurations using pre-fabricated plasmonic microstructures.
3. To establish the condition where the SPP-driven model breaks down and determine other possible competing LSFL mechanisms.
4. To examine periodic nanostructure formation on silicon and its relation to the

point defect generation mechanism.

5. To develop a model for the mechanism and dynamics of HSFL formation on silicon.

The significance of this thesis lies in the fundamental understanding of laser-matter interactions in the early irradiation timescale leading to the formation of periodic structures. The dynamics of the interactions are largely affected by significant changes in the carrier and lattice behaviors, which are observable through the changes in optical properties, band structure, and, subsequently, modified surface geometries. The scientific implications being, the observation of periodic structure formations correlates largely to well-studied optical phenomena such as SPP excitation, diffraction, and band gap collapse, as well as fundamental materials kinetics such as point defect generation and diffusion. As such, given enough understanding, laser induced periodic structure formation may serve as powerful characterization and engineering tools, among other applications.

CHAPTER II

Literature Review

A review on theories and results relevant to the thesis topic is presented in this chapter. Emphasis is put on processes occurring within and/or close to the timescale of laser pulse duration to highlight the early stages of LIPSS formation dynamics. This chapter also presents a brief summary of LIPSS morphologies and their corresponding mechanisms in the literature.

2.1 Ultrafast Laser Interaction with Matter

The interaction between a femtosecond laser pulse and semiconductors starts with carrier excitation. For a photon energy larger than the bandgap of the material, valence electrons can be excited to the conduction band via single photon (linear) absorption. In the case of indirect gap materials such as silicon, the process has to be accompanied by a phonon transition to conserve momentum. For wide bandgap materials, multi-photon absorption is required to excite carriers. This is achievable by femtosecond laser irradiation considering the high intensity delivered by the pulse. At high laser intensity, multi-photon absorption may even dominate over linear absorption [2]. Concurrent with carrier excitation, electrons at the conduction band can freely absorb another photon, which further increases their energy. Free electrons with kinetic energy larger than the bandgap may further promote valence electrons to

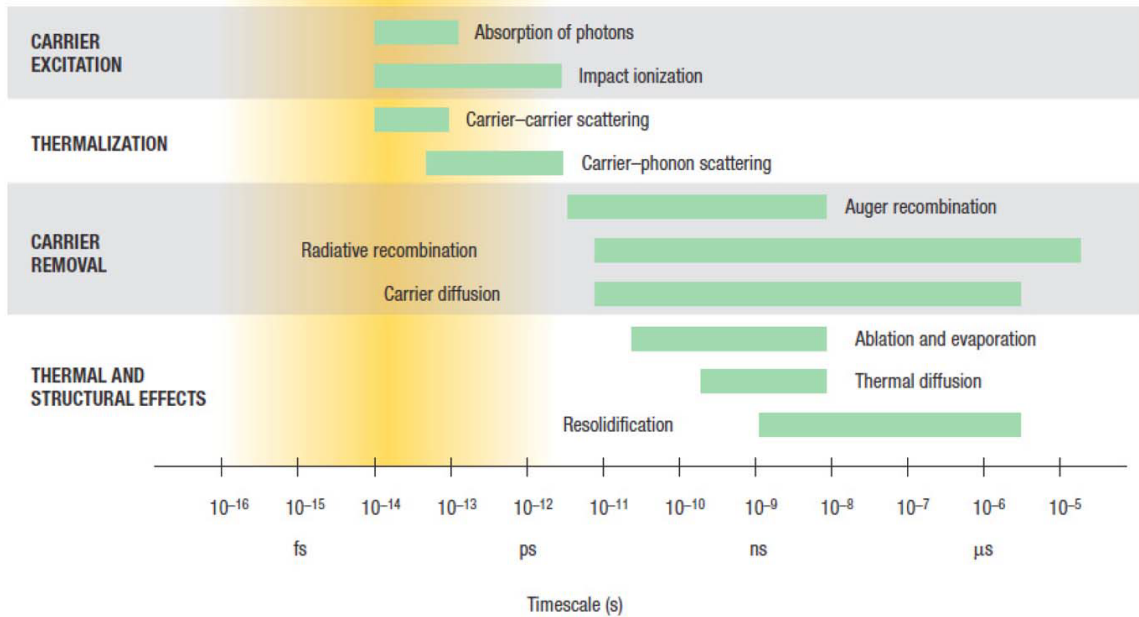


Figure 2.1: Timescales of various carrier and lattice processes following an ultrafast laser pulse irradiation. Adapted from [1]

the conduction band through impact ionization. Note that the notion of free electrons within the duration of the pulse may be a generalization considering the excited carriers initially remain coherent with the electromagnetic field before dephasing effects start to occur [26].

Immediately after excitation, carriers redistribute their energy through carrier-carrier and carrier-phonon scattering processes. Carrier-carrier scattering occurs almost immediately after excitation in the order of 10 fs [27]. Although, it may take about a few hundreds of femtoseconds before the carriers are Fermi-Dirac distributed and thermalized [28]. The total amount of energy of the carriers itself does not change during the process. In contrast, carrier-phonon scattering decreases the total energy of carriers through phonon emission, in which energy is transferred to the lattice. This process may occur within the same band valleys (intravalley) or across different band valleys (intervalley). The energy carried by the phonons itself are tiny considering the mass of electron. Therefore, carriers and lattice reaches thermal equilibrium only

after several picoseconds [1].

The discrepancy between the initial carrier and lattice thermal energies is the basis of the two-temperature model [29–31]. In the model, the energy of carriers increases through laser absorption and initially remains within the carrier system. Subsequent carrier-carrier scattering causes the redistribution of the carrier energy, which results in the carriers and lattice having two distinct temperatures. Note that this assumption is only valid once the thermalization of carriers is finished, or else the carrier temperature distribution would be too complex to be described by a single characteristic value [30]. The lattice itself is assumed to remain at room temperature. This is reasonable for femtosecond laser irradiation considering that longitudinal optical (LO) phonon emission time at carrier densities larger than 10^{18} cm^{-3} has been reported to be at least 165 fs or more in GaAs [32] (longer than the pulse duration used in this study). Once thermalized, hot electrons would reach temperature exceeding 10^4 K [33] and transfers its energy back to the lattice until thermal equilibrium between the two systems is achieved.

Once carriers and lattice reach thermal equilibrium, excess carriers would be removed through recombination and diffusion processes. Carrier recombination can either be a radiative process, which emits a photon, or a non-radiative process, such as in the case of Auger recombination. In Auger recombination, electron relaxation to the valence band releases excess energy, which excites another electron higher in the conduction band. Consequently, the total energy in the carrier system will remain constant, while the amount of excited carriers decreases. In contrast, the carrier diffusion process does not decrease the total amount of excited carriers in the system. However, carrier density would still effectively decrease within the initial photoexcited region.

2.1.1 Ultrafast Laser Induced Structural Dynamics

Energy transfer from the carrier system to the lattice is mainly driven by excited carrier coupling with optical phonon modes [34, 35]. The lattice then may heat up to the point of melt given that sufficient amount of energy is being supplied. This purely thermal framework of laser induced structural transformation assumes that phonon emission process occurs relatively quickly compared to the duration of the laser pulse. Thermal equilibration between carriers and lattice itself may take around tens of picoseconds after irradiation [1]. For this reason, a thermal model sufficiently explains sub-nanosecond or longer duration laser pulse irradiation of materials [36].

For picosecond and femtosecond laser irradiations, however, studies have long suggested that the excitation of dense electron-hole plasma may directly result in lattice disorder due to the subsequent decrease in the atomic binding potential [37–39]. This so called plasma annealing or ultrafast melting process is supported by the observation of a liquid-like surface in silicon and GaAs within less than one picosecond after a femtosecond laser irradiation [40–42], too fast for any substantial thermal effect to take place. Further, in a supporting pump-probe study, the lattice structure of a silicon surface is shown to lose its cubic order within 150 fs after a femtosecond laser pulse irradiation above the melt threshold evidenced by a vanishing second harmonic signal [43].

In a series of experiments conducted on GaAs [8, 44–46], semiconductor to metal transition is observed over several picoseconds after irradiation. This semiconductor to metal transition has been attributed to the modification of band structure in the framework of ultrafast melting. Lattice disorder arises due to the inertial destabilization of "cold" lattice ions, forming an intermediate state between a solid and a liquid [9], which causes the band gap to narrow and eventually closes. The phenomenon is often referred to as band gap collapse. Interestingly, this effect is shown to be structurally reversible after hundreds of nanoseconds [1] when looking at the change in the

dielectric function of the material just below the threshold of melt [8, 44]. bandgap collapse continued to be observed above melt [36, 47], but the original dielectric function disappears noting the obvious permanent structural changes [8, 45].

Separate theoretical studies concerning structural response under an intense laser pulse have confirmed that the electronic band gap decreases as the excited carrier density increases and can vanish when around 10% of valence electrons are excited [7, 48, 49]. The predicted band gap collapse carrier density is fairly consistent with experimental values [2, 36], in which they should be close to the carrier density at the threshold fluence of melt. Above the melt threshold, carrier-phonon scatterings continue to transfer energy to the lattice following carrier thermalization and may cause rapid melting. A large thermal gradient between the solid-liquid interface leads to rapid resolidification and can result in an amorphous structure being formed.

At an even higher irradiation fluence than melt, ultrafast laser ablation may occur in the form of liquid spallation. Initially, rapid melting of the materials surface creates a large pressure gradient between the air-liquid and the liquid-solid interfaces due to the superheated liquid remaining in constant volume. A subsequent tensile wave is launched starting from the surface as the material expands [30], which drives void nucleation within the liquid phase. Ensuing coalescence of voids along the interface causes the separation and ejection of the liquid layer [12, 13]. The abrupt nature of void coalescence and the following liquid spallation creates a characteristic quasi-smooth surface of an ultrafast laser ablation crater. In the case of an extremely high fluence irradiation, rapid heating may cause direct expulsion of surface region into a two phase liquid vapor mixture [13]. Such process is referred to as phase explosion. Note that the conventional ablation mechanism discussed above does not quite apply for dielectrics and wide band-gap semiconductors, where electronically driven mechanism such as Coulomb explosion is more likely to occur [14, 15].

2.1.2 Drude model

In a highly excited semiconductor, the excited electron density becomes large enough that its optical properties are mostly characterized by the free carrier response of the dense electron-hole plasma generated by the laser field [2, 50, 51]. In this thesis, Drude model is used to account for the free carrier response of an irradiated material. The assumptions within the Drude model includes [52]:

1. No electron-electron and electron-ion interactions are considered.
2. Collisions between electron and lattice (damping) are instantaneous with the probability $1/\tau$, where τ is the mean collision time of electrons.
3. Electrons loses energy only through collision events and becomes thermally equilibrated with its surroundings.

According to the Drude model formalism, the change in dielectric function due to free carrier response $\Delta\epsilon_{fcr}$ is as follows:

$$\Delta\epsilon_{fcr} = -\frac{\omega_p^2}{\omega(\omega + i/\tau_D)} \quad (2.1)$$

Where,

$$\omega_p = \sqrt{\frac{Nq^2}{\epsilon_0 m_{opt}^* m_e}} \quad (2.2)$$

is the plasma frequency, ϵ_0 is the permittivity of vacuum, q is the elementary charge ω is the laser angular frequency, m_{opt}^* is the optical mass of carriers, m_e is the electron rest mass, and N is the carrier density. Equation (2.1) essentially describes the motion of atomic dipoles under an oscillating field without the presence of restoring force (i.e. free electron). Note that although the variables such as m_{opt}^* and τ_D can be intuitively defined, their values do not explain exact physical processes. For instance, the Drude

mean collision time τ_D still assumes instantaneous collision events. While, in a more realistic view, carrier waves would dephase or "slowly collide" when encountering atomic potential and other carriers [53]. On the other hand, m_{opt}^* is conceived as a classical simplification of electronic motion through the potentials of the lattice and its singular value corresponds to an ensemble average of effective masses over the band structure [54]. Even so, the heuristic approach provided by the Drude model has been reported to yield excellent agreement with experimental results on highly excited semiconductors [2, 39].

2.2 Laser Induced Periodic Surface Structures

Periodic corrugations on semiconductors due to laser irradiation were first reported more than 5 decades ago by Birnbaum [55]. Since then, numerous occurrences of LIPSS have been observed on virtually all types of materials ranging from metals to dielectrics [16, 17]. LIPSS are most commonly classified into 2 main types based on their periodicity: low spatial frequency LIPSS (LSFL) for structures with period close to the laser wavelength λ and high spatial frequency LIPSS (HSFL) for structures with period less than 0.5λ [56]. Both types of LIPSS have been reported to form either parallel or perpendicular to the laser polarization [16]. The characteristic laser polarization and wavelength dependence of LIPSS implies a largely optically coupled mechanism of their formation from the start. Below we will review some of LIPSS formation mechanisms proposed in the literature.

2.2.1 Sipe Theory

One of the most prominent theories explaining the origin of LIPSS was proposed by Sipe and coworkers in 1982 [25]. The Sipe theory is constructed from a first principle calculation of surface scattered wave on random rough surfaces. In the derivation, the medium is separated into two coupled regions, the homogeneous bulk

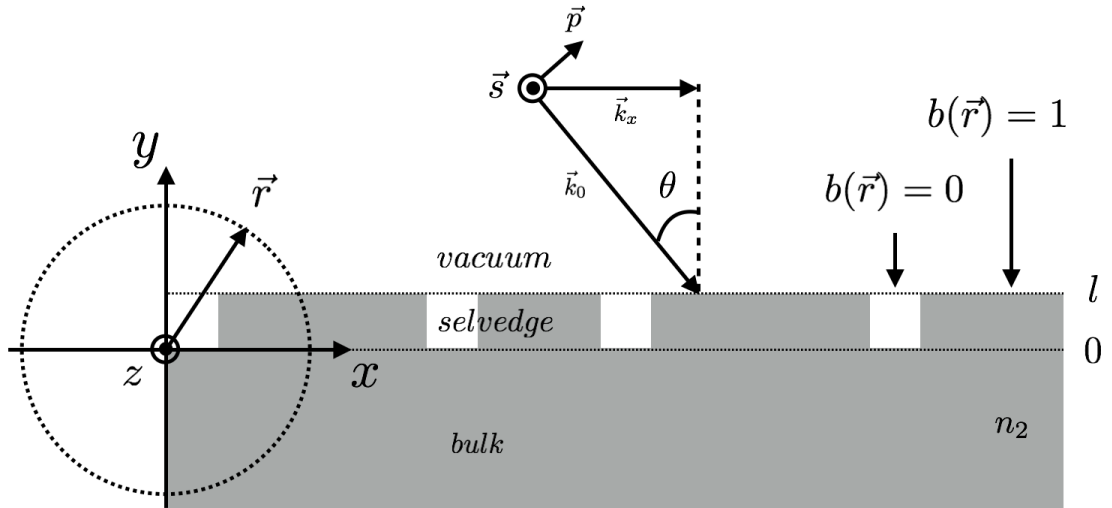


Figure 2.2: Surface roughness as modeled by the Sipe theory. The system is divided into three coupled regions: vacuum (air), selvedge, and bulk. The laser wavevector $\vec{k}_0 = 2\pi/\lambda \vec{u}$, where \vec{u} is the unit vector of the incident beam.

and the selvedge (fig. 2.2). The selvedge region contained within $0 < y < l_s$, where $l_s \ll \lambda$, have the same properties as the bulk where surface roughness is present. The surface roughness is then modeled as a binary function $b(\vec{r})$ in space domain with $b(\vec{r}) = 0, 1$ for unfilled part or "vacuum" and filled material region. As such, in the selvedge region, $n_2(\vec{r}) = n_2 b(\vec{r})$, where n_2 is the bulk refractive index. The central result following the interference between the scattered and refracted fields yields the following relation:

$$I(\vec{k}) \propto \eta(\vec{k}; \vec{k}_x) |b(\vec{k})| \quad (2.3)$$

in which, the total absorbed intensity $I(\vec{k})$ is proportional to the product of the efficacy factor $\eta(\vec{k}; \vec{k}_x)$ and the absolute amplitude of surface roughness $|b(\vec{k})|$. The efficacy factor is defined as a response function describing the magnitude of inhomogeneous absorption at frequency coordinate \vec{k} for an incident field with wavevector \vec{k}_x parallel to the rough surface. Characteristically, the function $\eta(\vec{k}; \vec{k}_x)$ exhibits sharp

peaks where conditions $|\vec{k}_x \pm \vec{k}| = |\vec{k}_0|$, $|\vec{k}_x \pm \vec{k}| = |\vec{k}_0|n_2$ are met. Hence, when a random slowly varying $|b(\vec{k})|$ is present, $I(\vec{k})$ is commonly viewed as being independent of surface roughness. It has to be noted that in the case where the dielectric function of the bulk materials becomes metallic, the efficacy factor does predict sharp resonant peaks due to surface plasmon coupling. Sipe Theory has been widely successful in explaining LSFL formation for a large range of materials [57]. However, it has not been particularly effective in explaining HSFL formation in general [56]. Note also that Sipe theory only applies for surfaces that are fairly smooth to begin with and cannot account for LIPSS formation at large surface structures such as a step-edge.

2.2.2 LSFL Formation Mechanisms

LSFL have been studied to form under a large range of laser pulse duration. This includes continuous wave (CW) [57, 58], nanoseconds [59–61], picoseconds [62–64], and femtoseconds [65–67]. The possibility of LSFL formation using a CW laser may indicate a formation mechanism that is largely unaffected by the surface morphology changes during laser exposure. In other words, ideally, it can be a steady state process (as in the case with the Sipe theory). However, the dynamics of such process may dramatically change for irradiations with nanosecond or shorter pulse duration. For one, LSFL are inherently structured lattice damage in the form of melt and/or ablation. Hence, after each laser pulse, the surface morphology and optical properties of the material continue to evolve. For instance, the periodicity of LSFL has been reported to decrease with increasing number of laser pulses applied [18, 68]. This behavior has been attributed to the grating coupled surface plasmon mechanism, in which the shift in the LSFL periodicity is related to the change in the phase matching condition due to the deepening of the grating like corrugations [18]. The details to the explanation, unfortunately, has been purely qualitative due to the complexity of the actual process.

The involvement of surface plasmon polaritons (SPP) mentioned above is an established concept [19, 69], owing to the fact that most LSFL form perpendicular to the laser polarization [16]. In semiconductors and dielectrics, the hypothesis is supported by the evidence of a transient metallic plasma generation due to free carrier response within the duration of a femtosecond laser pulse [2, 70, 71]. A coupled SPP field would interfere with incident light to produce LSFL with wavevector [18]

$$\vec{k}_{LSFL} = \vec{k}_x - \vec{k}_{SPP} \quad (2.4)$$

where \vec{k}_x is the laser wavevector component parallel to the surface, and \vec{k}_{SPP} is the wavevector of the propagating SPP field along the surface. This hypothesis will be the basis of the LSFL formation mechanism discussed in Chapter IV.

A different type of LSFL oriented parallel to the laser polarization are less common and are observed almost exclusively in dielectrics [72, 73]. This type of LSFL has typical wavelengths of $\Lambda_{LSFL} \sim \lambda/n_2$ [74]. The mechanism of its formation can be attributed to the radiation remnants phenomenon, which is a non radiative mode predicted by the Sipe model [75]. The discussion of this mechanism, unfortunately, is outside the scope of this thesis. Parallel LSFL has also been observed in silicon following a single pulse irradiation of a step edge [76]. The mechanism, which is related to near-field diffraction, will be discussed in detail in Chapter V.

2.2.3 HSFL Formation Mechanisms

In contrast to LSFL, HSFL formation has been exclusively picosecond and femtosecond laser irradiation phenomena [16, 17]. HSFL typically requires a large number of exposures at lower fluence relative to the LSFL formation. There has not been a reported HSFL formation using a single pulse laser irradiation. There are at least two distinct HSFL morphologies observed in the literature. In the case of dielectrics and

wide bandgap materials, perpendicular HSFL commonly form deep below the surface resembling Bragg-grating like morphology [77–80]. Their formation is accompanied by materials removal to some degree evidenced by cross-sectional observation [81–83] and the amount of debris generated. Competing mechanisms for this type of HSFL formation include nanoplasma generation [77, 82, 84], second harmonic generation [78], Mie scattering [79], and grating-splitting via resonant to non-resonant surface plasmon transition [18]. This type of HSFL formation is observed in 4H-SiC in this thesis and will be discussed further in Chapter VII.

Much shallower lamellar-like HSFL morphologies are observed in metals and low bandgap semiconductors [85–88]. Several formation mechanisms proposed for this type of HSFL include second harmonic generation [86, 89], and self organization due to spatial asymmetry of the initial carrier kinetic energy [90]. The latter mechanism brought about an interesting concept of taking into account possible involvement of lattice kinetics imposed by the laser irradiation. This idea is supported by the observation of periodic structures similar to HSFL generated by ion sputtering [91–93]. On a side note, HSFL also form with orientation parallel to the laser polarization [94–96], albeit sufficient explanation for their formation mechanism is still lacking. All things considered, it is very likely that multiple formation mechanisms exist and that their activation is very particular to the kind of materials system irradiated.

Another particular type of HSFL formation in GaAs has recently been reported by Abere and coworkers [11]. In their study, perpendicular HSFL is observed to have evolved from nanoscale bumps or islands generated at fluences below the threshold of melt. The island formation is proposed to be the result of point defect diffusion and accumulation due to cold lattice ion movements concurrent with massive carrier excitations induced by the laser. Cross-sectional transmission electron microscopy (TEM) data indicates that the growths of both islands and HSFL are epitaxial and little to no material is being removed during the process. This particular model is ini-

tially predicted to occur on silicon as well. Currently, perpendicular HSFL on silicon is only observed for near-infrared (NIR) laser irradiation using MHz high repetition rate laser [89, 97, 98]. The complete dynamics of the formation is still under debate. In Chapter VI, a report on Si HSFL formation with both parallel and perpendicular orientations to the laser polarization is presented. The structures, formed using a 1 KHz 390 nm laser, show similar islands to HSFL evolution characteristics observed previously in GaAs. The results offer substantial insights to the understanding of general HSFL formation dynamics in low bandgap semiconductors and the role of laser wavelength.

2.3 Review on Relevant Optics

2.3.1 Fresnel Equations

The Fresnel equations formalism is used to describe the surface reflectivity of a material in this work. Homogeneous optical properties are assumed for all mediums. Light incident on an interface between two mediums of differing refractive indices requires boundary conditions imposed by Maxwell's equation to be satisfied. Assuming non-magnetic materials, electric and magnetic field components on the two mediums parallel to the interface have to be continuous. As such, the incident, reflected, and refracted beams would lie on the same plane. Further, the incident beam angle θ_i equals to the reflected beam angle θ_r according to the law of reflection.

From the boundary conditions, the amplitude of the reflected and refracted fields would then be dependent on the state of polarization of the incident beam. In the case of transverse magnetic (TM) or p-polarized field, where the magnetic field component is parallel to the interface, the reflectivity R_p is found to be [99]:

$$R_p = \left| \frac{n_1 \cos \theta_t - n_2 \cos \theta_i}{n_1 \cos \theta_t + n_2 \cos \theta_i} \right|^2 \quad (2.5)$$

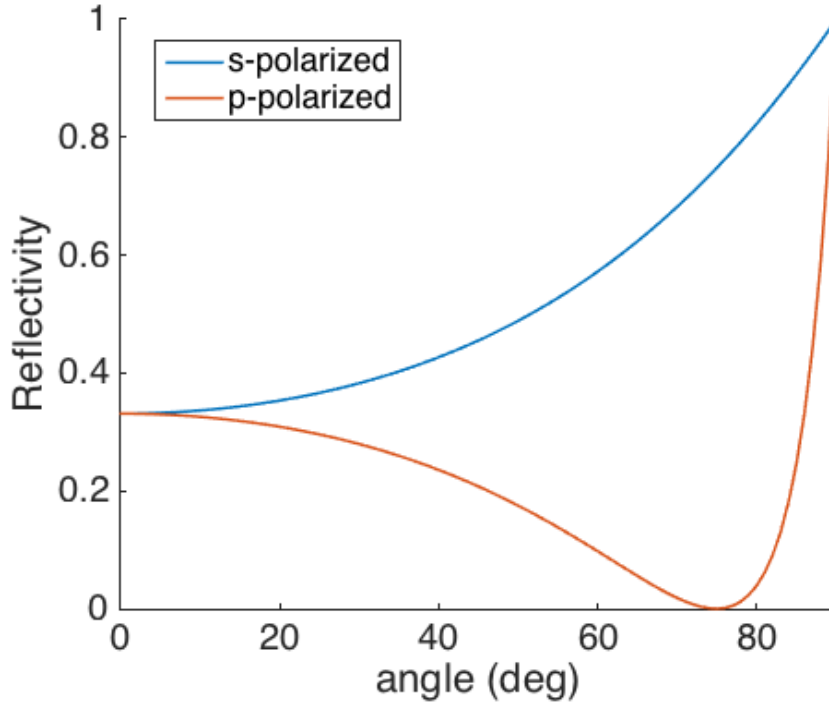


Figure 2.3: Angle dependent reflectivity of unexcited silicon at 780 nm wavelength for both s-polarized and p-polarized incident fields.

where, n_1 and n_2 are the refractive indices of mediums 1 and 2 respectively, and θ_t is the refracted beam angle. In the case of transverse electric (TE) or s-polarized field, where the electric field component is parallel to the interface, the reflectivity R_s is found to be:

$$R_s = \left| \frac{n_1 \cos \theta_i - n_2 \cos \theta_t}{n_1 \cos \theta_i + n_2 \cos \theta_t} \right|^2 \quad (2.6)$$

Both eqs. (2.5) and (2.6) are dependent only on θ_i when we take into account Snell's law $n_1 \sin \theta_i = n_2 \sin \theta_t$. The angle dependent reflectivity of intrinsic silicon for $\lambda = 780$ nm is shown in fig. 2.3. While s-polarized reflectivity continually increases with angle, p-polarized reflectivity decreases initially and reaches minimum at $\theta_B = \arctan(n_2/n_1) \approx 75^\circ$, also called the Brewster's angle.

2.3.2 Surface Plasmon Polariton Field

A surface plasmon polariton is characterized by a propagating electromagnetic field across an interface between a metal and a dielectric [100]. The field arises from the oscillation of the surface charge density (i.e. surface plasmon) due to the coupling of incident photons (hence the term polariton). We begin by examining the coupling of TM field to an interface shown in fig. 2.4 [101]. The TM waves propagating in the x direction signifying a surface plasmon polariton field at the metal dielectric interface. The amplitude of the SPP field decays exponentially in the y directions and along the propagation direction.

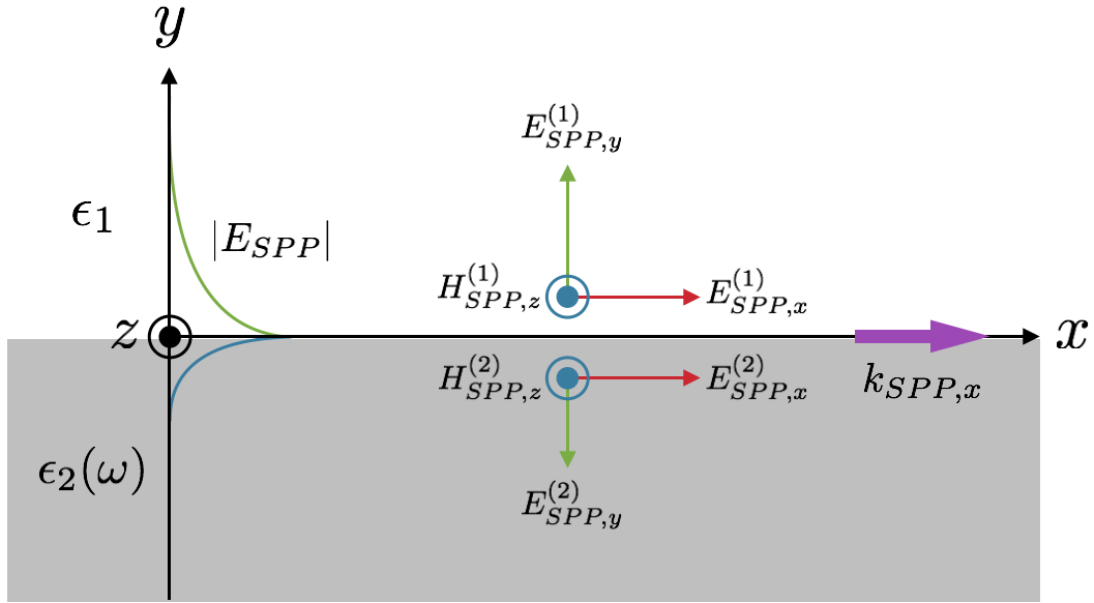


Figure 2.4: TM field propagating in the x direction implying surface plasmon polariton field at the metal dielectric interface. The amplitude of the SPP field decays exponentially in the y directions and along the propagation direction.

The solutions to the Maxwell's equations are expected to yield the following mag-

netic fields in each medium:

$$\vec{H}_{SPP}^{(1)}(x, y, t) = (0, 0, A)e^{i(k_{SPP,x}x + k_{SPP,y}^{(1)}y - \omega t)} \quad (2.7a)$$

$$\vec{H}_{SPP}^{(2)}(x, y, t) = (0, 0, B)e^{i(k_{SPP,x}x - k_{SPP,y}^{(2)}y - \omega t)} \quad (2.7b)$$

where A and B are the magnetic field amplitudes. Following Ampere's law, we find that the corresponding electric fields are as follows (see appendix A):

$$\vec{E}_{SPP}^{(1)}(x, y, t) = -\frac{A}{\omega\epsilon_1}(k_{SPP,y}^{(1)}, -k_{SPP,x}, 0)e^{i(k_{SPP,x}x + k_{SPP,y}^{(1)}y - \omega t)} \quad (2.8a)$$

$$\vec{E}_{SPP}^{(2)}(x, y, t) = -\frac{B}{\omega\epsilon_2(\omega)}(-k_{SPP,y}^{(2)}, -k_{SPP,x}, 0)e^{i(k_{SPP,x}x - k_{SPP,y}^{(2)}y - \omega t)} \quad (2.8b)$$

Boundary conditions imposed by Maxwell's equations require the continuity of tangential components of the electric and the magnetic fields (due to the absence of net current density). This implies that $k_{SPP,x}$ must be equal within the metallic and dielectric mediums. Hence, at the interface $y = 0$, eqs. (2.8a) and (2.8b) above would yield the following relation:

$$\frac{k_{SPP,y}^{(2)}}{k_{SPP,y}^{(1)}} = -\frac{\epsilon_2(\omega)}{\epsilon_1} \quad (2.9)$$

In order to obtain a decaying function away from the metal-dielectric interface, as in the case of a localized surface electromagnetic field, $k_{SPP,y}^{(2)}$ and $k_{SPP,y}^{(1)}$ have to be both positive and imaginary. The consequence of the requirement implies a negative real part of $\epsilon_2(\omega)$ (since ϵ_1 is always positive). If ϵ_1 is the permittivity of air or vacuum, then $Re(\epsilon_2(\omega)) < -1$. Taking into account the momentum conservation criteria that

have to be satisfied in each medium:

$$(k_{SPP,x})^2 + (k_{SPP,y}^{(1)})^2 = \epsilon_1 \left(\frac{\omega}{c}\right)^2 \quad (2.10a)$$

$$(k_{SPP,x})^2 + (k_{SPP,y}^{(2)})^2 = \epsilon_2(\omega) \left(\frac{\omega}{c}\right)^2 \quad (2.10b)$$

Combining eqs. (2.10a) to (2.10b) yields the following SPP dispersion relation:

$$k_{SPP,x} = \frac{2\pi}{\lambda} \left(\frac{\epsilon_1 \epsilon_2(\omega)}{\epsilon_1 + \epsilon_2(\omega)} \right)^{1/2} \quad (2.11)$$

Since $\epsilon_2(\omega)$ is inherently complex for most metals, we would expect complex values of $k_{SPP,x}$, $k_{SPP,y}^{(2)}$, and $k_{SPP,y}^{(1)}$, which explains the propagating and decaying nature of SPP fields parallel and normal to the interface. Note that eq. (2.11) also implies that $k_{SPP,x}$ is always larger than the laser wavevector $2\pi/\lambda$, which means that additional momentum matching processes have to take place in order for the SPP mode to couple to the material surface. The coupling mechanism of SPP on a step-edge surface will be discussed further in section 5.1.3. Following the same derivation, a TE field coupled to a metal-dielectric interface would yield the following relation:

$$(k_{SPP,y}^{(2)} + k_{SPP,y}^{(1)})A = 0 \quad (2.12)$$

Since both components have to be positive, the field amplitude $A = B$ has to be 0. Hence, a localized surface electromagnetic field cannot exist in this case.

CHAPTER III

Experimental Details and Methods

3.1 Characterization of the Ultrafast Laser Beam Parameters

Ultrafast laser pulses used in all of the experiments are generated from a chirped pulse amplified (CPA) Ti:sapphire based laser system (Clark MXR CPA-2001). The final output yield a 780 nm wavelength, ~ 150 fs full width half maximum (FWHM) pulse width beam at 1 kHz repetition rate.

The temporal profile of the pulse are achieved through intensity autocorrelation. The ultrafast laser pulse intensity I can be modeled with a Gaussian function as follows

$$I(t) = I_0 e^{-4 \ln 2 \left(\frac{t}{t_p}\right)^2} \quad (3.1)$$

Here, I_0 denotes the peak intensity and t_p is the pulse width at FWHM. When dealing with a pulsed laser system (especially ultrashort laser pulses), it is often more convenient to evaluate the laser energy density in terms of a time independent

quantity such as fluence. Fluence F is calculated by integrating Intensity over time

$$F = \int_{-\infty}^{\infty} I(t)dt \quad (3.2)$$

evaluating eqs. (3.1) and (3.2), fluence can be expressed as

$$F = \sqrt{\frac{\pi}{4 \ln 2}} t_p I_o \quad (3.3)$$

The spatial profile of the beam can be imaged using a CCD camera (WincamD UCD-12) (for details see [102]). The imaged beam at focus follows a quasi-symmetrical gaussian distribution. The fluence of a single pulse can then be defined by the following relation

$$F(x, y) = F_p e^{-2 \frac{(x^2+y^2)}{w_o^2}} \quad (3.4)$$

where F_p is the peak fluence, and $w_0 =$ the beam radius at $1/e^2$ of the peak fluence (i.e. beam waist). Integrating eq. (3.4) in both x and y directions yields the total energy of a single pulse

$$E_{pulse} = F_p \frac{\pi}{2} w_o^2 \quad (3.5)$$

The corresponding laser power P is measured using a thermal volume absorber (Ophir Optics). E_{pulse} can then be found from P/f_{rep} , where f_{rep} is the pulse repetition rate of the laser. The final expression for F_p is as follows

$$F_p = \frac{2P}{\pi w_o^2 f_{rep}} \quad (3.6)$$

Note that the expression πw_0^2 describes the circular beam area at $1/e^2$ of the

peak beam intensity. In practice, non-circular beam shapes are commonly attained. Therefore πw_0^2 may be replaced by the effective area A_{eff} of the beam instead. Depending on the focusing elements used, the beam waist at the focal point can also be calculated as follows:

$$w_o = \frac{2\lambda f}{\pi D} \quad (3.7)$$

where λ = laser wavelength, f = focal length of the focusing element, and D = diameter of the incident collimated beam. Several factors contribute to the deviation of the experimentally measured beam waist from the theoretical calculation based on eq. (3.7): spherical aberration of the focusing element and the quality of the Gaussian beam, which is affected by diffraction during propagation and general imperfections in the optical alignment within the laser system and in the experimental setups.

3.2 Focusing Conditions and The Rayleigh Length

The determination of focal point of a focused beam in real applications is, unfortunately, not as straightforward as a simple geometrical derivation, especially when dealing with Gaussian beams. Firstly, spherical aberration may increase the depth of focus of the beam but causes distortion of the beam image. Another thing to note, commercially sourced focusing elements only provide optical specifications for general usage, of which the values cannot be taken as is. Therefore, the focal point has to be measured empirically at the start of every experiment to minimize error. We can then define the beam at the focal point to have the smallest measured effective area. This is valid for optical beam measurements such as using the CCD beam profiler. Consequently, an ideal Gaussian beam would yield its highest intensity at the focal point as well. Hence, a sample surface positioned at the focal point of the beam would yield the largest damage area at above the damage thresholds. A reliable method to

find the focal point position relative to the sample surface position then would be to induce damage on the sample at varying distances on the beam propagation axis. The variation in the damage area itself is more easily seen close to the damage threshold. A non consistent damage pattern with respect to the beam position would indicate a couple of conditions: a non-ideal Gaussian beam shape and/or laser output instability. As a reliable rule of thumb, Rayleigh length relates to the depth of focus of a Gaussian beam, where the wavefront of the beam can be approximated as planar to a certain extent. It is defined by:

$$Z_R = \frac{\pi\omega_0^2}{\lambda} \quad (3.8)$$

It is clear from eq. (3.8) that the depth of focus increases with the spot size of the beam. This relation is useful in determining tolerable deviation from the true focal position when calibrating the irradiation setup.

3.3 The Definition and Determination of Damage Thresholds

Materials may undergo permanent structural transformations when irradiated with a single laser pulse of high enough fluence. Two main types of damage relevant to this thesis are melt and ablation. Melt defines the lost of crystallinity of the material at time infinity after irradiation. This is typically accompanied by the change in reflectivity of the irradiated material region [103]. Ablation, on the other hand, is accompanied by a net removal of material via expulsion. An ablation crater is commonly visible above a certain peak fluence and its edge corresponds closely to the fluence at threshold.

Following a gaussian intensity profile, the radius of the damaged area formed at

a certain peak fluence would vary according to the relation [104]:

$$r = \omega_0 \sqrt{\frac{1}{2} \ln\left(\frac{F}{F_{Th}}\right)} \quad (3.9)$$

Where F_{Th} defines the fluence at threshold. It is straightforward to measure the area of the damage using optical microscopy. Radius of the damage, in reality, would be an effective value due to the quasi-circular beam profile. Calibration of the image scale is done separately depending on the instrument and magnification used, but it is always a good practice to independently measure a well known reference sample to begin with.

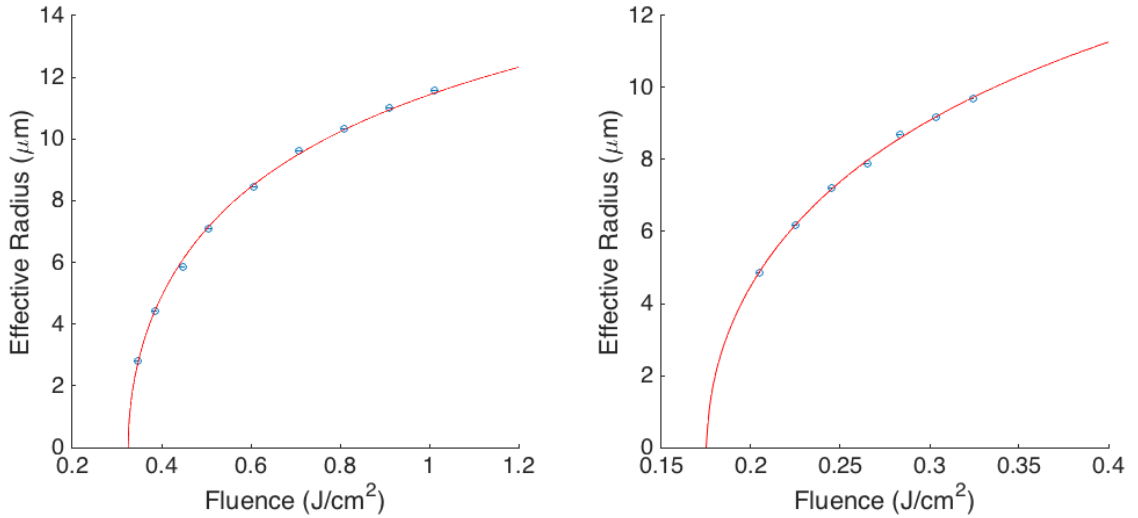


Figure 3.1: Two parameter fit curves of ablation (left) and melt (right) thresholds of Silicon at 780 nm irradiation.

The determination of threshold is then done by measuring arrays of damage areas at fluences above the threshold of single pulse laser irradiations. The best fit curve of the measured data would follow eq. (3.9) and determine the two varying parameters ω_0 and F_{Th} . (For an example curve fitting code in MATLAB see appendix B). Since ω_0 could already be determined independently using a beam profiler camera, (see section

3.1) the fitted value may serve as a reference to the goodness of the fit. Ideally, Both measured and calculated values of ω_0 should be identical. As an example, below are the two parameter fit curves of melt and ablation threshold of silicon at 780 nm irradiations. The calculated ablation and melt thresholds are 0.32 ± 0.02 J/cm² and 0.18 ± 0.01 J/cm², respectively. Since both Silicon thresholds are well characterized within our experimental conditions, their values may serve as an indicator of whether the laser is performing to specifications.

3.4 Frequency Doubling of the Ti:Sapphire Laser

Doubling the fundamental frequency of the laser is done through second harmonic generation (SHG) using a beta-barium borate (BBO) crystal. SHG is a two-photon process occurring in mediums lacking inversion symmetry since it relies on the second order susceptibility $\chi^{(2)}$. The second order nonlinear polarization term can be written as [105]:

$$P^{(2)}(t) = \epsilon_0 \chi^{(2)} E(t)^2 \quad (3.10)$$

Assuming electric field in the form of:

$$E(t) = E e^{i\omega t} + E^* e^{-i\omega t} \quad (3.11)$$

The second order polarization term becomes:

$$P^{(2)}(t) = \epsilon_0 \chi^{(2)} (E^2 e^{i2\omega t} + E^{*2} e^{-i2\omega t} + 2|E|^2) \quad (3.12)$$

We find that the resulting term above shows oscillations at twice the original laser frequency. From a physical perspective, incoming waves are coherently scattered into higher energy virtual states which then radiates into higher energy photons.

Therefore, in order to achieve large order of second harmonic (SH) transition, the input and SH waves have to be in phase with one another. Phase matching challenges in the frequency doubling process come from the inherent dispersion of the doubling crystal. It is then crucial to propagate the beam along the direction of the crystal where both input and SH pulses travel at the same phase velocity.

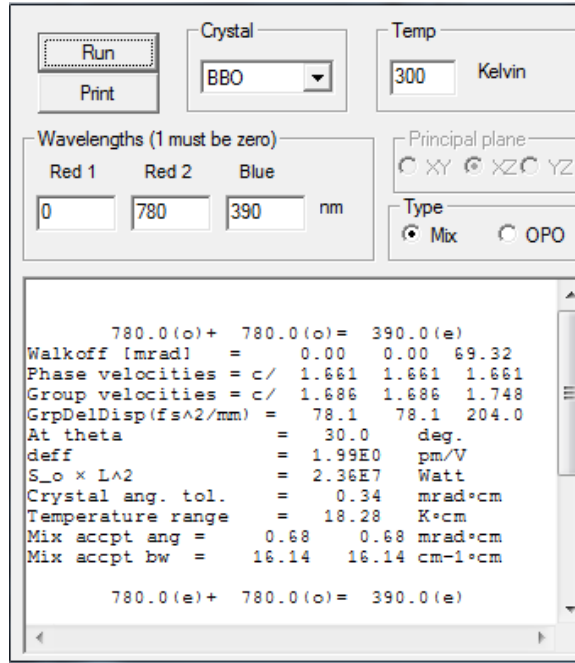


Figure 3.2: Calculated parameters for 780 nm - 780 nm frequency mixing in BBO crystal (using SNLO software).

Freely distributed software SNLO [106] was used to calculate the optimal BBO crystal angle θ for phase matching. At 780 nm input wavelength, optimal $\theta = 30^\circ$ (type I) with input pulse traveling along the ordinary axis and the SH pulse along the extraordinary axis. Although phase velocity mismatch between the input and SH pulses can be effectively compensated, both beam still travel different group velocity (with SH pulse being slower). The group velocity mismatch (GVM) between the pulses effectively decreases the amount of supported bandwidth of the SH transition and thus the doubling efficiency [107]. Using the calculated accepted bandwidth by SNLO (mix accept bw), we can then determine the maximum crystal thickness for

efficient frequency doubling (see the help section of [106]). A 150 fs laser pulse at 780 nm has a bandwidth¹ of 97.85 cm^{-1} . Therefore, the crystal thickness L has to be less than 1.65 mm.

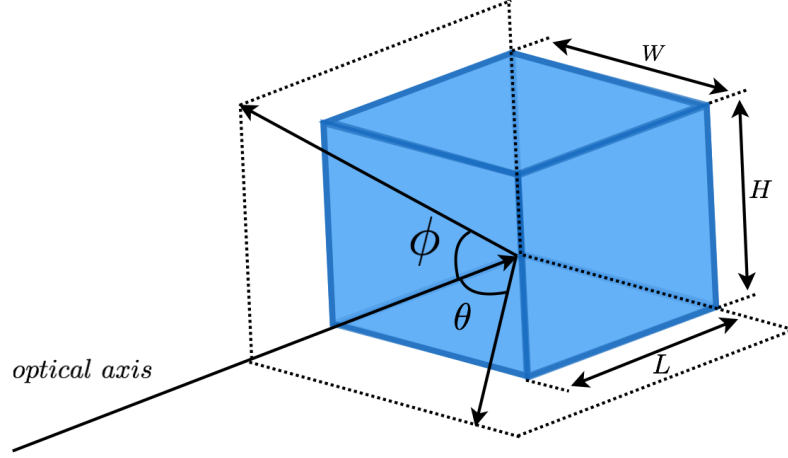


Figure 3.3: Diagram of BBO crystal dimension and orientation.

Type I BBO crystal (Eksma Optics) with $\theta/\phi = 29.2^\circ/90^\circ$ cut, $W = H = 10$ mm, and $L = 0.5$ mm was used in our experiments. Initial collimated beam has a diameter larger (>10 mm) than the BBO crystal used. 2x beam reducer effectively reduces the diameter of the beam by half in order to avoid any clipping of the beam. Since the crystal angle used is not exact to the calculation, additional crystal tilt $\Delta\theta$ is necessary to further compensate the phase mismatch. This further increases the walk-off angle of the generated SH pulse, and so the offset between the propagation axes of the input and the SH beams has to be kept in mind when aligning the lens. The beam output after the BBO will be a mixture of the input and SH pulses. A bandpass filter centered around 390 nm sufficiently attenuates 780 wavelength pulses and allow only the frequency doubled pulse to pass through. A SHG conversion

¹The bandwidth is calculated based on a Gaussian transform limited pulse. The time bandwidth product of a Gaussian pulse follows $t_p \Delta f_p \approx 0.44$, where Δf_p is the frequency bandwidth. In units of cm^{-1} , the bandwidth equals $\Delta f_p/c$, where c is the speed of light.

efficiency of 12% at 0.1 mJ pulse energy is achieved in our experiments.

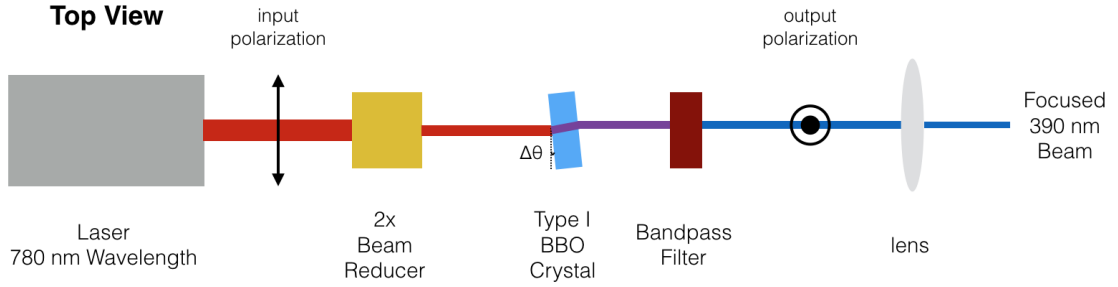


Figure 3.4: Experimental setup for frequency doubled beam.

The spot size calculation of the frequency doubled beam is done using the two parameter fit method outlined in section 3.3. Note that focused beam profiling using a WincamD CCD camera (section 3.1) is not recommended due to the low sensitivity of the camera sensor at 390 nm wavelength.

3.5 Sample Preparation and Parameters

3.5.1 Gold Mesa Samples

Gold mesa samples were fabricated by Sandia National Laboratory using standard photolithography and lift-off techniques (for complete details see [102]). A variety of microstructure shapes were fabricated as shown in fig. 3.5. All of the microstructures consist of 10 nm titanium intermediate layer in between the deposited gold and silicon (100) substrate to prevent de-lamination. Mesas of various heights h were irradiated in the experiments ($h = 100, 390, 585, 720, \text{ and } 975 \text{ nm}$). Ideally, the mesas would have vertical step-edges. However, due to lift-off procedure, the step-edge has a tilt of up to 20° relative to the surface normal. In Chapter V, we will discuss how the mesa geometries, particularly the height and the tilt of the step-edge will affect the coupling strength of the SPP and the subsequent LSFL formed.

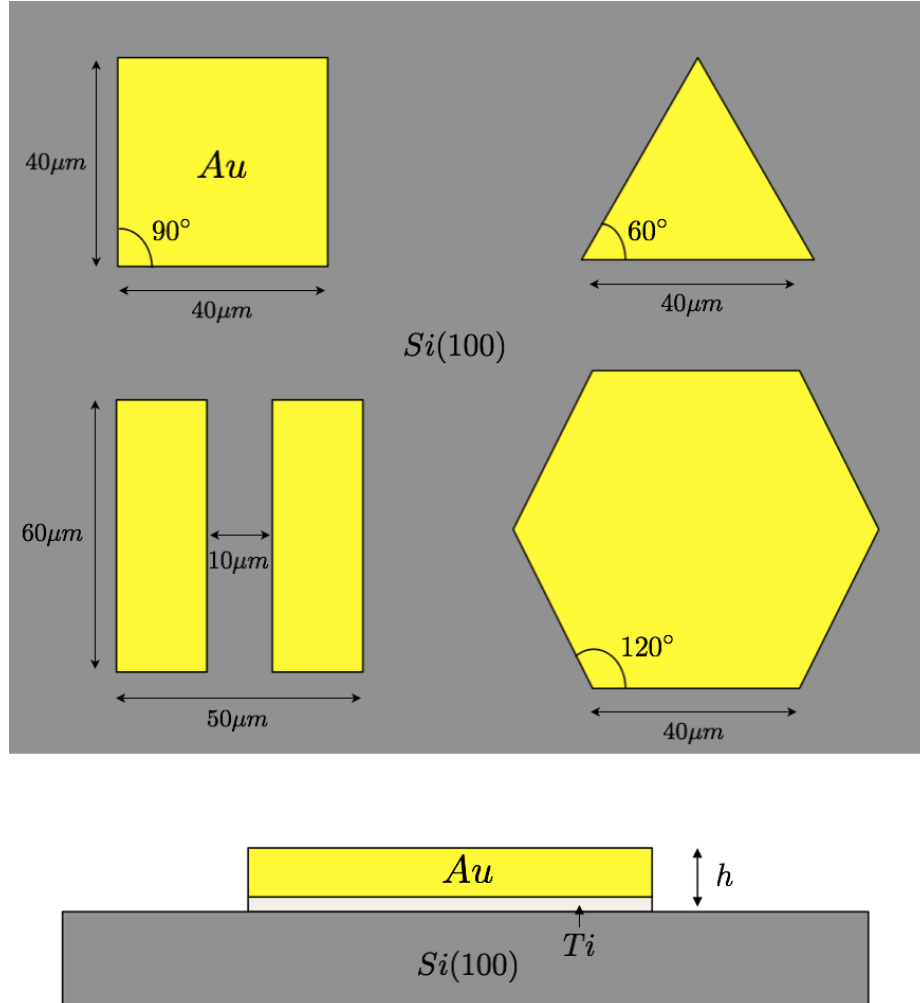


Figure 3.5: Diagrams of various shapes of the fabricated gold mesas (top) and their cross-section (bottom).

3.5.2 Silicon Step-Edge Samples

Silicon step-edge structures were fabricated at the Lurie Nanofabrication Facility (LNF). The final height h of the features was measured to be 590 ± 20 nm. Pre-irradiation, all samples were treated with HF solution to remove any oxide formed during the fabrication process and other surface contamination that might be present. In this section, we will briefly outline the fabrication process. To start, a mask outlining the shapes of the microstructure was obtained. The mask consists of a glass substrate with selectively etched chrome film via photolithography. The chrome

acts as the absorbing medium for the subsequent photoresist exposure on the silicon substrate. The silicon step features were achieved using reactive ion etching (RIE) in order to create a flat sidewall profile. Since the patterned mask was intended for lift-off procedures, an image reversal process was necessary to obtain the correct photoresist template.

Clean 4" silicon wafers were first vapor primed using hexamethyldisilazane (HMDS) to improve the photoresist adhesion to the substrate. Then, SPR220 photoresist (Dow Chemicals) was spin-coated on the substrates to achieve a layer thickness of ~ 2 μm . Initial softbake at 115 °C reduced the solvent content of the photoresist. Next, near-UV exposure under the mask template created regions of soluble photoresist (positive). Image reversal of the photoresist was done by flooding NH_3 gas at 90 °C in order to cross-link the soluble photoresist region. As the reversed photoresist image became inert (negative), the subsequent flood exposure of near-UV light formed soluble photoresist at the remaining untreated areas. Another post exposure bake at 115 °C further cross-linked the reversed negative resist. Finally, the entire photoresist layer was treated using AZ series developer causing the positive resist to be removed. The exposed silicon surface could then be anisotropically etched using HBr gas via RIE process forming step edge features. The remaining leftover photoresist was easily cleaned using O_2 plasma treatment.

3.5.3 Chemical Etching of Samples

In order to remove oxide on its surface before irradiation, silicon substrates were treated using 10:1 mixture of 49% hydrofluoric acid (HF) solution and deionized (DI) H_2O . The reported etching rate of single crystal silicon using 10:1 HF solution is 23 nm/min [108]. Since silicon native oxide thickness is on the order of a few nm [109], the minimum etching time would be less than 1 minute. HF treatment of silicon would lead to H-terminated surface which passivates the surface from further oxidation in

air [110]. Following hydrogen passivation, silicon surface has been reported to remain atomically pristine for up to 15 minutes in ambient condition [111].

The chemical treatment of SiC post-irradiation were done using a 1:1 mixture of buffered HF and HNO₃ (HNA). 1:1 HNA solution has been studied to etch a-SiC and oxides at a rapid rate: HNO₃ acts as an oxidizing agent for both silicon and carbon atoms, while HF effectively etches the subsequent silicon oxides formed [108]. The reported etch rates for a-SiC is 300 nm/min [112]. Much slower etching rate is achieved for poly-crystalline and single crystalline SiC [113]. All samples were etched at room temperature for 5 minutes. This ensures that only single-crystal SiC remains during subsequent characterization.

Regarding safety procedure, HF and HNA solution has to be contained using appropriate plastic containers (polyethylene, polystyrene, etc). All treatment steps have to be done inside an adequately ventilated fume hood to contain any hazardous vapor. Minimum amount of PPE (apron, double nitrile gloves, face shield) has to be worn at all times during the processes. It is recommended that the treated samples are rinsed a minimum of 2 times using adequate amount of DI water. For complete standard operating procedure (SOP) see [114].

3.6 Vacuum Irradiation

Multi-pulse femtosecond laser irradiation of silicon has been observed to induce oxidation [115]. Particularly in this thesis, we will show laser induced formations of tall oxide mounds on silicon with heights reaching up to 10 μm (Chapter VII). The formation of oxides poses a challenge in characterizing the evolution of islands and HSFL on silicon. Moreover, the existence of native oxide on silicon [109] pre-irradiation would have an effect on the hypothesized point defect or atomic diffusion toward the surface. The native oxide layer can be removed by chemical etching processes (see section 3.5.3). In order to prevent further oxidation, irradiation of

silicon samples were done inside a mini vacuum platform as shown in figure 3.6. The glass window functions as an entry for the focused laser beam, of which it has to be as close as possible to the focusing element to prevent any non-linear effects at high intensity. The turbo pump (Pfeiffer Vacuum HiCube) connected to the chamber is capable of achieving high vacuum pressure in the order of 10^{-6} torr. Focal position of the focused beam would change depending on the focusing power of the lens and the window thickness. Therefore, further calibration of the sample surface position to match the beam focal point has to be done.

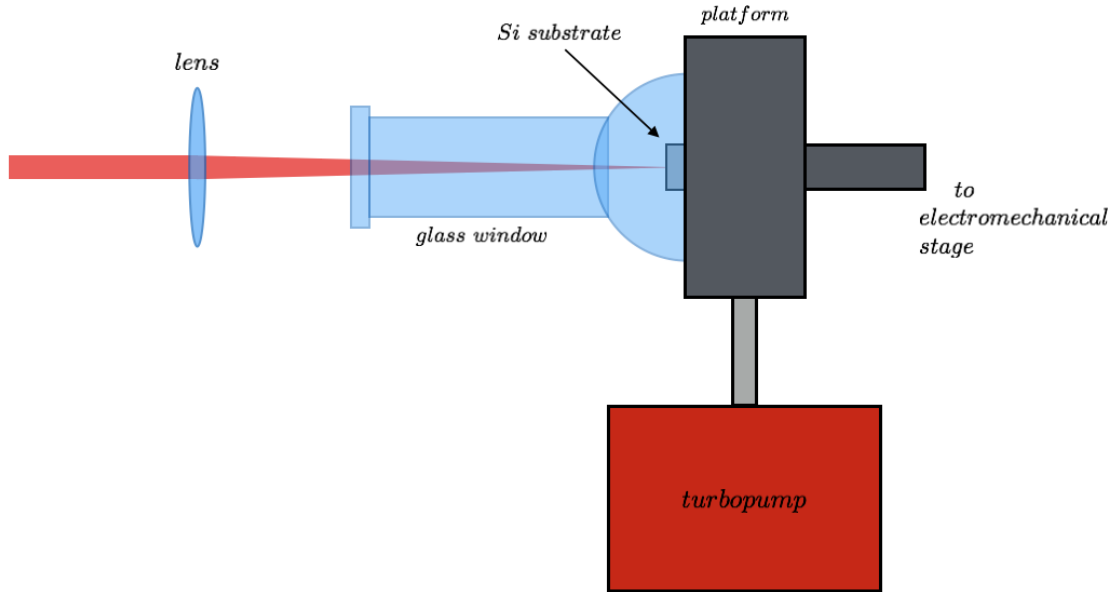


Figure 3.6: Diagram of experimental setup for irradiation of silicon in vacuum

3.7 Finite Element Frequency Domain Field Calculations

Finite element calculations of gold microstructure irradiations on silicon are performed in the frequency domain using COMSOL. The simulated geometry follows that of the cross-section of the gold mesas as shown in fig. 3.7 with a step-edge tilt of 17° . The mesa height h is varied according to the experimental samples (see section 3.5.1). Perfectly matched layer (PML) was used as absorbing boundaries outside

of the material regions. All regions were meshed with a maximum feature size of $\lambda/16$. The intrinsic dielectric function of materials were obtained from [116], while the excited materials dielectric function were calculated and discussed in Chapter V. The incident Gaussian electric field takes the following form:

$$E(x, y) = E_0 \frac{w_0}{w(y)} e^{-\frac{x^2}{w(y)^2}} e^{i[k_0 y - \phi_G(y) + \frac{k_0 x^2}{2R(y)}]} \quad (3.13)$$

where E_0 is the electric field amplitude (normalized), $w(y)$ is the beam radius, $R(y)$ is the beam curvature, and $\phi_G(y)$ is the Gouy phase shift [117]. the position dependent functions are defined as follows:

$$w(y) = w_0 \sqrt{1 + \left(\frac{y}{z_R}\right)^2} \quad (3.14)$$

$$R(y) = \begin{cases} y(1 + (\frac{z_R}{y})^2) & \text{for } -10^{10} \times z_R < y \leq -10^8 \times z_R \\ 10^8 \times z_R & \text{for } -10^8 \times z_R < y \leq 10^8 \times z_R \\ y(1 + (\frac{z_R}{y})^2) & \text{for } 10^8 \times z_R < y \leq 10^{10} \times z_R \end{cases} \quad (3.15)$$

$$\phi_G(y) = -\arctan\left(\frac{y}{z_R}\right) \quad (3.16)$$

where $z_R =$ Rayleigh length (see section 3.2). Two types of polarization orientations were simulated: along the x-direction (P_{\perp}) and along the z-direction (P_{\parallel}).

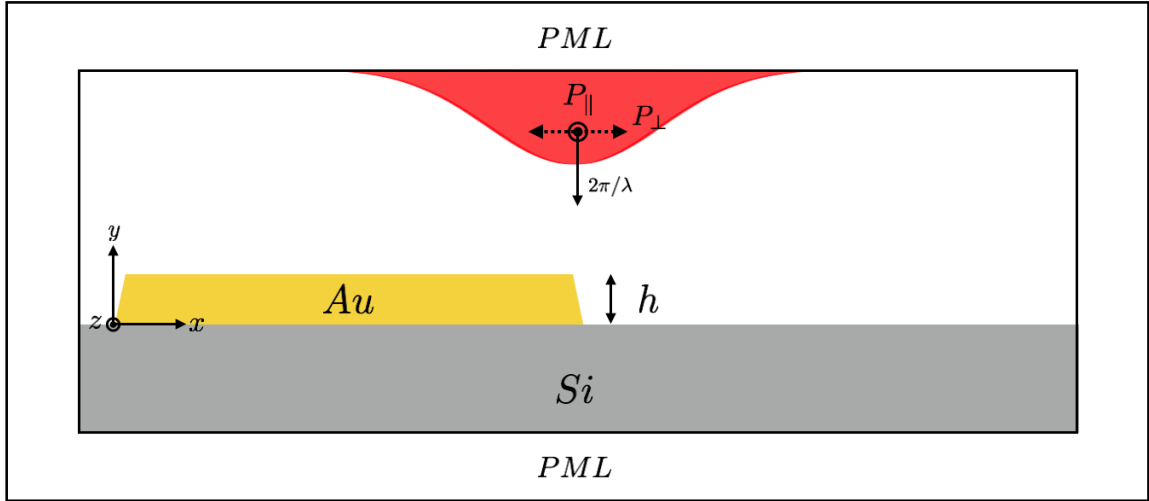


Figure 3.7: COMSOL simulation setup showing the cross-sectional geometry of the gold mesa with height h . A Gaussian light source with wavevector $2\pi/\lambda$ is used. Two polarization directions along the x-direction (P_{\perp}) and z-direction (P_{\parallel}) are shown.

CHAPTER IV

Ultrafast Laser Self-Interference with Concurrently Induced Surface Plasmon Polariton Field

The excitation of SPPs have long been proposed to be one of the main mechanisms of LSFL formation [18, 19, 25, 69]. However, the complete dynamics of SPP excitation leading to the formation of LSFL are rarely explored. SPP interference with an incident laser field has been suggested in the literature [18], albeit the quantitative explanation to the process has not been explicitly laid out, especially at the early stage of the process. The goal of this chapter then is to provide quantitative as well as physical interpretations to the LSFL formation based on the SPP-laser interference hypothesis. We will argue that SPP-laser interference is the main mechanism of LSFL formation in general.

LSFL formation on semiconductors are ubiquitous [16, 17]. This is very interesting considering that intrinsic semiconductor properties do not typically support SPP modes [100]. Therefore, several crucial factors have to be considered in order to support our hypothesis:

1. The excited carrier density of the irradiated material at the surface has to be large enough to induce metallic transition.

2. SPP modes have to be coupled at the materials interface via some momentum matching mechanisms.
3. SPPs have to be generated within the laser pulse duration.
4. At the same time, the irradiation fluence has to be large enough to alter the surface morphology via melting and/or ablation processes.

The above points will be the basis of the model for LSFL formation used in this thesis.

4.1 Ultrafast Dynamics during Ultrafast Laser Irradiation on Silicon

Carrier excitation in semiconductors can be driven by linear and nonlinear absorption processes [118]. The lowest order nonlinear process involves two-photon absorption (TPA), of which the absorbed intensity is proportional to the square of the laser intensity. The total absorbed intensity I then follows the differential equation:

$$\frac{\partial I}{\partial z} = -\alpha I - \beta I^2 \quad (4.1)$$

The linear absorption coefficient α includes contributions from both inter-band carrier transition and free carrier absorption (intra-band transition). Hence, $\alpha = \alpha_0 + \alpha_{fca}$ where α_0 is the linear inter-band absorption coefficient and α_{fca} is the free carrier absorption coefficient [2]. Meanwhile, the TPA coefficient β is commonly small and the TPA contribution only becomes significant at high enough irradiated laser intensity. In silicon, for instance, the value of β reported in the literature varies roughly between 1.5 cm/GW and 9 cm/GW [119–121] at 800 nm. Meanwhile, at 620 nm the value of β is determined to be around 38 cm/GW [122, 123], which is considerably higher.

The excited carrier density N can be deduced from the total number of absorbed photons by the linear and nonlinear inter-band carrier transition processes and is represented by the following differential equation [2].

$$\frac{\partial}{\partial t}N(t) = \left[\alpha_o + \frac{1}{2}\beta I(t) \right] \frac{I(t)}{\hbar\omega} \quad (4.2)$$

where $\hbar\omega$ denotes the photon energy. Note that eq. (4.2) neglects any recombination process happening within the duration of the pulse. By integrating eq. (4.2) and using eq. (3.3) to define fluence, the expression for carrier density can be written as:

$$N = \frac{F(1 - R)}{\hbar\omega} \left[\alpha_o + \frac{\beta F(1 - R)}{2\sqrt{2\pi}t_p} \right] \quad (4.3)$$

The factor $(1 - R)$ accounts for the fraction of total energy absorbed with R being the effective reflectance of the material.

The assumption proves fairly reasonable in the case of ultrafast laser irradiation of silicon at 620 nm [2]. For irradiation at near infrared (NIR) wavelengths, however, the calculated carrier density using eq. (4.3) does not correlate very well with the actual irradiation fluence. For instance, Bonse et al. calculated a carrier density of $6.7 \times 10^{21} \text{ cm}^{-3}$ at 0.42 J/cm^2 at the fluence of 0.42 J/cm^2 using an 800 nm wavelength laser [19]. The value equals to 3% of the total valence electron in silicon (with valence electron density N_0 of silicon being $2 \times 10^{21} \text{ cm}^{-3}$). Considering that the melt threshold fluence reported by the same research group is 0.27 J/cm^2 [124], the estimated carrier density is likely to be too low.

A substantial number of theoretical studies have hypothesized that around 10% of valence electron has to be excited in order to induce band gap collapse [7, 48, 49]. Experimental studies have also observed that bandgap collapse can occur slightly below the melt threshold [8, 44]. Moreover, in a recent molecular dynamics (MD) study by Lian et al., the melting of silicon by ultrafast laser irradiation has been largely

attributed to the non-thermal plasma annealing process [6]. In their calculation, the lattice temperature stays well below the melting temperature of silicon during lattice destabilization. The study also predicts that around 10% of valence electrons has to be excited in order to induce melt, consistent with previous experimental and theoretical results. While optically excited carrier density itself cannot be directly measured by experiment¹, it is reasonable to conclude that at least 10% of valence electrons has to be excited above the bandgap collapse and melt thresholds, considering prior discussions.

4.1.1 Impact Ionization Contribution

Free electrons with kinetic energy higher than the band gap may promote valence electrons to the conduction band through impact ionization (see section 2.1). The probability of impact ionization itself is dependent upon the carrier density. The process also depends on the increase of free electron energy through intra-band absorption. Impact ionization contribution to the plasma generation by ultrafast laser is often omitted due to the complexity of the process. However, a study conducted by Pronko et al. have noted that impact ionization might dominate the carrier excitation process above the critical plasma density in silicon [3]. Their explanation may provide a correction to the underestimated carrier density value of silicon previously discussed in the literature. A simplification to the contribution of impact ionization on the excited carrier density is used in our calculation as follows [125, 126]:

$$\frac{\partial}{\partial t}N(t) = \Phi_I I(t)N(t) \quad (4.4)$$

¹In addition, an accurate interpretation of the carrier density from experimental values may require: a more physically meaningful model of the dielectric function (i.e. an amendment to the Drude model) and the inclusion of a more complete many-body formalisms in the carrier dynamics model used.

where Φ_I is the impact ionization coefficient, which is assumed to be constant. The value of Φ_I is reported to be $21.2 \text{ cm}^2/\text{J}$ for silicon at 786 nm wavelength [3, 125].

4.1.2 Optical Properties of the Excited Surface

Due to the large amount of excited carriers during ultrafast laser irradiation, the optical properties of the surface would depend largely on the free carrier response. In addition, high intensity achievable by ultrafast laser pulse would induce nonlinear effects [125]. The combined contributions of the responses described above would yield a perturbed form of the dielectric function as follows:

$$\epsilon_2 = \epsilon_g + \Delta\epsilon_{fcr} + \Delta\epsilon_{NL} \quad (4.5)$$

where ϵ_g is the initial unexcited material dielectric function ($13.764 + 0.056i$ for silicon at 780 nm [116]), $\Delta\epsilon_{fcr}$ and $\Delta\epsilon_{NL}$ are the free carrier response and nonlinear effect contributions to the change in the dielectric function, respectively. Within eq. (4.5), changes due to TPA will be taken into account by the inclusion of $\Delta\epsilon_{NL}$. Whereas, changes due to linear interband absorption commonly described by the Lorentz oscillator model is neglected. This assumption is valid considering the high level of carrier excitations in our experiments, where a TPA mechanism has been shown to dominate the interband transition process [2].

4.1.2.1 Free Carrier Response

The change in the dielectric function due to free carrier response $\Delta\epsilon_{fcr}$ can be described by the Drude model and is given by eq. (2.1). The Drude function depends on three main parameters: the carrier density N , the optical mass of carriers m_{opt}^* , and the Drude damping time τ_D . The carrier density increases with time via inter-band absorption and impact ionization processes according to eq. (4.2) and eq.

(4.4). The Drude damping time describes the mean collision time of carriers (see section 2.1.2). Hence, τ_D ideally depends upon N and carrier temperature T_e [127, 128]. Unfortunately, the dependence of τ_D on both parameters are complicated. The value of τ_D , however, has been treated as a constant and shows a good agreement with experimental results. τ_D is reported to be in the order of 1 fs for a highly excited silicon [2, 129].

The optical mass can be described as a function of carrier temperature and density [54, 130, 131]. A derivation of the optical mass from first principle calculation has been done with great accuracy up to the carrier density of 10^{22} cm^{-3} [54, 130, 131]. No experimental result on m_{opt}^* has been reported for a carrier density higher 10^{22} cm^{-3} . Further approximation of m_{opt}^* beyond $N = 10^{22} \text{ cm}^{-3}$ would require a more accurate model of the band structure due the failure of nonparabolic band approximation as the the Fermi energy E_F becomes increasingly large. This, however, is outside the scope of our study. For the sake of simplicity, the value of m_{opt}^* used in our calculation would only depend on temperature and follows a linear fit according to the theoretical calculation done by Riffe [54]. The assumption would be accurate in the nondegenerate limit where carrier temperature is high or carrier density is low. In that case, m_{opt}^* would be independent of carrier density. The temperature dependent function of m_{opt}^* is then given as follows:

$$m_{opt}^* = m_{opt,0}^* + m_s T_e \quad (4.6)$$

where $m_{opt,0}^* = 0.14$ is the fitted optical mass at absolute 0, and $m_s = 3.2 \times 10^{-5} \text{ K}^{-1}$ is the slope of the linear fit.

4.1.2.2 Nonlinear Effects

Crystal systems with inversion symmetry such as silicon do not exhibit second order nonlinear characteristics. Hence, we consider only third order nonlinear effects in our calculation. An incident electric field $E(t)$ would then induce a polarization in the form

$$P(t) = \epsilon_0(\chi^{(1)}E(t) + \chi^{(3)}E^3(t)) \quad (4.7)$$

where $\chi^{(1)}$ and $\chi^{(3)}$ are the first and third order susceptibility, respectively. The third order polarization comprises of a variety of processes involving three photons, one of which being self phase modulation (SPM). The process is characterized by an intensity dependent change in the refractive index given by the Kerr coefficient n_{22} . Taking into account only SPM, frequency components expansion of the third order nonlinear term in would yield a corresponding polarization [132]

$$P(t) = \epsilon_0(\chi^{(1)} + \frac{3}{4}\chi^{(3)}|E(t)|^2)E(t) \quad (4.8)$$

The term inside the bracket in eq. (4.8) can be defined as the effective susceptibility χ_{eff} of the material. Since $\chi^{(1)}$ inherently describes linear intra and interband processes, the change in the dielectric function due to nonlinear effects will be

$$\Delta\epsilon_{NL} = \frac{3}{4}\chi^{(3)}|E(t)|^2 \quad (4.9)$$

where $|E_0(t)|^2$ is the square amplitude of the time-varying electric field, which can be obtained using the intensity function described in eq. (3.1):

$$|E(t)|^2 = \frac{2}{\epsilon_0 c Re(n_2)} I(t) \quad (4.10)$$

where c is the speed of light in vacuum. The real and imaginary parts of $\chi^{(3)}$ are related to n_{22} and β , respectively [105, 133]

$$\text{Re}(\chi^{(3)}) = \frac{4}{3}c\text{Re}(n_2)^2\epsilon_0 n_{22} \quad (4.11a)$$

$$\text{Im}(\chi^{(3)}) = \frac{2c^2\text{Re}(n_2)^2\epsilon_0}{3\omega}\beta \quad (4.11b)$$

The positive $\text{Im}(\chi^{(3)})$ pertains to the field damping due to nonlinear absorption.

4.1.2.3 Effective Absorption

In order to calculate the total energy density $U(t)$ of the system, we also define an effective absorption coefficient α_{eff} that will include the contributions of both intra and interband transition processes [125]

$$\alpha_{eff} = \frac{4\pi\text{Im}(n_2)}{\lambda} \quad (4.12)$$

Assuming the absorbed energy remains within the initial irradiated region during the laser pulse (i.e. neglecting thermal conduction), the rate of change of $U(t)$ is then

$$\frac{\partial U(t)}{\partial t} = \alpha_{eff}I(t) \quad (4.13)$$

4.1.3 Carrier Temperature

Within the two-temperature model, any carrier-phonon scattering during the laser pulse is neglected, and the lattice is kept at room temperature. Hence, laser absorption will only increase the energy of electrons. The energy density of carriers u is defined as [52]

$$u = \int_{-\infty}^{\infty} g(\mathcal{E})\mathcal{E}f(\mathcal{E})d\mathcal{E} \quad (4.14)$$

where $g(\mathcal{E})$ gives the density of states (DOS) at energy level \mathcal{E} , and $f(\mathcal{E})$ is the Fermi-Dirac distribution. Assuming a free electron gas (FEG) model², $g(\mathcal{E})$ can be written as

$$g(\mathcal{E}) = \frac{8\pi\sqrt{2}}{h^3} m^{*3/2} \sqrt{\mathcal{E} - \mathcal{E}_c} \quad (4.15)$$

where h is the Planck's constant, m^* is the effective mass for DOS calculation ($m^* = 1.08$ for silicon), and E_c is the energy level at the conduction band edge. The Fermi-Dirac distribution is defined as follows:

$$f(\mathcal{E}) = \frac{1}{e^{(E-\mu)/k_b T_e} + 1} \quad (4.16)$$

where k_b is the Boltzmann constant, and μ is the chemical potential. Note that the chemical potential is a function of N and T_e (at $T_e = 0$, μ is equal to the Fermi energy \mathcal{E}_F). We can subsequently characterize the carrier heat capacity C_e by taking the gradient of u with respect to T_e at constant N [52]

$$C_e(T_e) = \left(\frac{\partial u}{\partial T_e} \right)_N \quad (4.17)$$

The carrier temperature would then be equal to the excess energy density of the free carriers divided by the C_e as follows:

$$T_e = \frac{U(t) - N E_g}{C_e} \quad (4.18)$$

where E_g is the bandgap. At high level of excitation, E_g will narrow due to the increase in many-body interactions [4, 134, 135]. The bandgap approximately decreases

²For the sake of simplicity. In a semiconductor state with low Fermi level, this would be a good approximation.

proportional to the cubic root of the carrier density. For silicon, [136]

$$E_g(N) = 1.12 - 1.5 \times 10^{-8} N^{1/3} eV \quad (4.19)$$

4.1.4 0-Dimensional Ultrafast Dynamics Simulation

Putting everything together we can construct a time dependent calculation of the carrier dynamics during an incident ultrafast laser pulse. The steps are illustrated in a simplified diagram below:

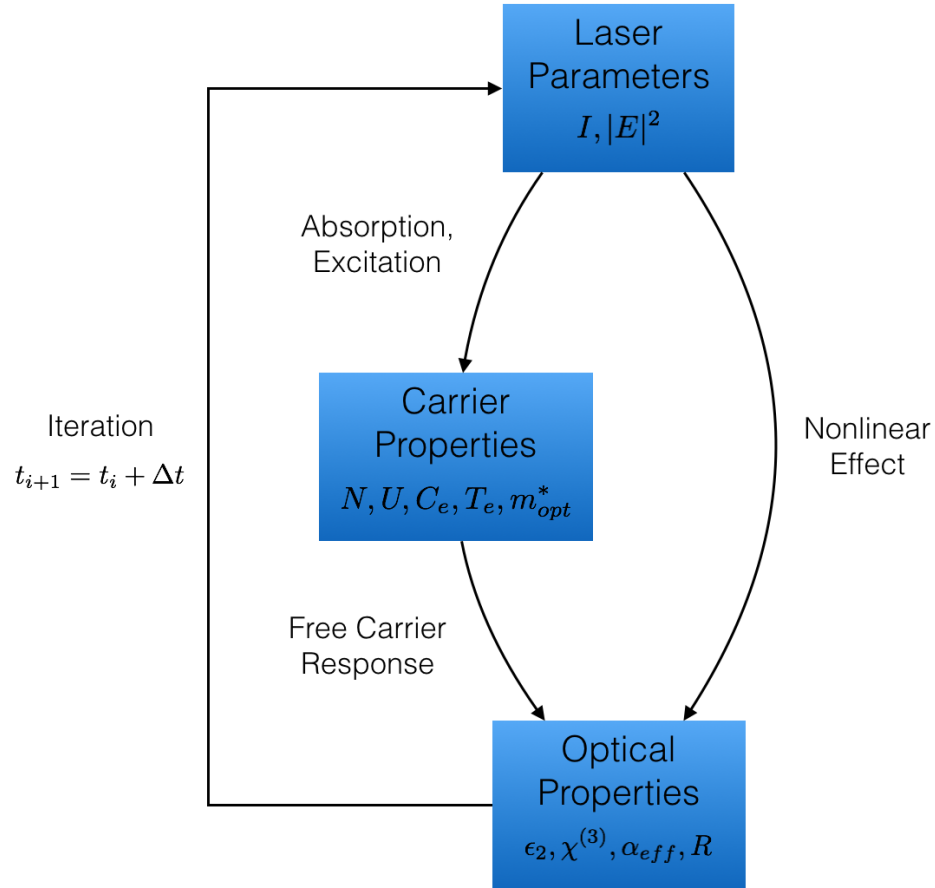


Figure 4.1: Diagram of the ultrafast laser irradiation dynamics simulation outlined in this chapter. The arrows illustrate the processes occurring and the direction of the calculation steps. t_i indicates the time at increment i separated by Δt .

A working algorithm for the simulation written in MATLAB can be found in

appendix C. In summary, the main assumptions used in the calculation are as follows:

1. Calculations are performed on a point at the surface of the material only (0-dimensional).
2. Two-temperature model (temperature of the carrier and lattice systems are treated separately).
3. Free electron gas model for DOS calculation
4. Linear and nonlinear dielectric responses are instantaneous.

Due to the 0-dimensionality of our calculations, no spatially dependent processes are taken into account. This includes neglecting any thermal conduction and carrier diffusion processes. We would argue that the processes are negligible within the pulse duration. In addition, since the SPP field is confined heavily at the surface³, carrier dynamics below the surface would not contribute strongly to the SPP properties. Regarding the use of the two-temperature model, carriers are assumed to have a well defined temperature at all times during the simulation. As such, thermalization of carriers is assumed to be fast relative to the timescale of the pulse duration. This assumption is also important if the carriers' energy state distribution are to be defined by the Fermi-Dirac statistics.

The carrier thermalization time has been observed to be inversely proportional to the carrier density [137, 138]. This is due to the increase in inelastic scattering probability between the carriers as carrier density increases [137]. In addition, carrier-phonon scattering rate also decreases due to screening effects when more free electrons are being generated [139]. In that case, carrier-carrier scattering becomes dominant. This further justifies the exclusion of carrier recombination processes during the laser pulse as carrier relaxation rate also consequently decreases with increasing N [139].

³In a good conductor such as Gold, SPP decay length below the surface is about 25 nm at 780 nm wavelength. As we are exciting silicon to a very high level, the decay length would be comparable.

4.2 SPP-Laser Interference Formalism

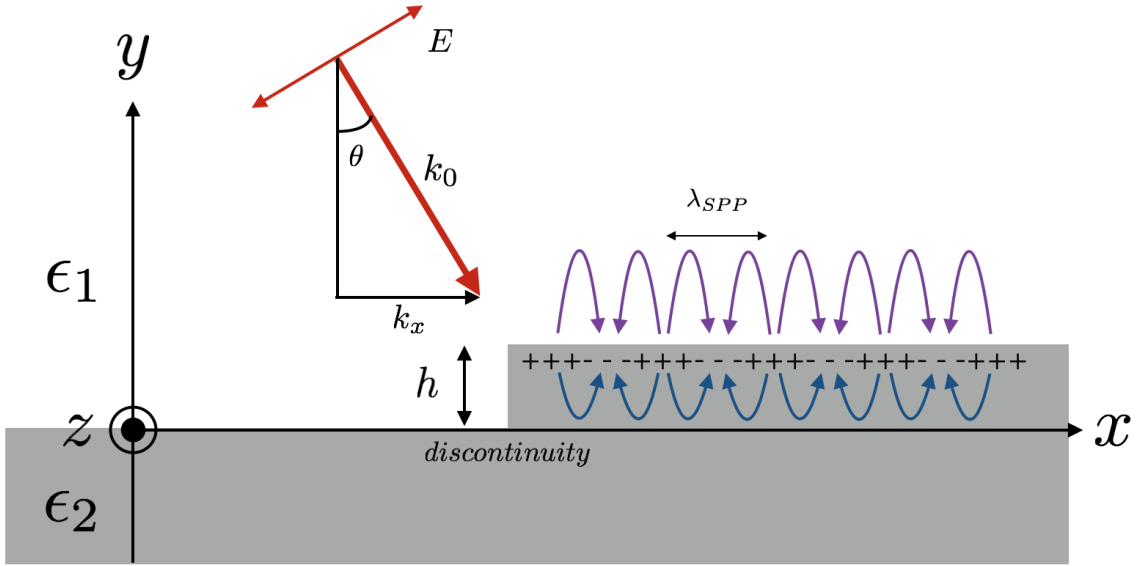


Figure 4.2: SPP-Laser interference diagram showing the propagation direction of each field. SPP is coupled by the surface discontinuity.

An SPP mode requires sufficient amount of momentum for it to be excited on a conducting surface. The momentum matching condition can be met by a propagating laser field in free space through coupling with surface discontinuities or roughness. We will discuss SPP coupling mechanisms further in chapter V. For now, we will assume that SPP will always be excited when the condition $Re(\epsilon_2(\omega)) < -1$ is satisfied. An SPP field may interfere with the incident laser above the surface within the duration of the laser pulse. In that case, a periodic laser intensity will arrive on the materials surface leading to selective ablation and subsequently forms LSFL. This is supported by a time-resolved study conducted by Murphy et al., in which LSFL is shown to form at around 50 ps after the pulse corresponding to the timescale of ultrafast ablation [140]

Consider a plane wave source incident at an angle θ on a surface as illustrated in

fig. 4.2. The laser field E_{laser} then takes the form

$$\vec{E}_{laser}(x, y, t, \theta) = E_0(\cos \theta, \sin \theta, 0)e^{i(k_x x - k_y y - \omega t)} \quad (4.20)$$

where $k_x = k_0 \sin \theta$ and $k_y = k_0 \cos \theta$. The coupled SPP field above the surface is given by eq. (2.8a). We can then evaluate the resulting intensity from the interference between the SPP and the laser field. The total intensity given by

$$I_t(x, y, t, \theta) \propto |\vec{E}_t(x, y, t, \theta)|^2 \quad (4.21)$$

where $\vec{E}_t = \vec{E}_{SPP}^{(1)} + \vec{E}_{laser}$. The solution to eq. (4.21) is as follows:

$$\begin{aligned} I_t(x, y, \theta) \propto & E_0^2 + \left(\frac{AD}{\omega\epsilon_1}\right)^2 (Re[k_{SPP,y}^{(1)}]^2 + Im[k_{SPP,y}^{(1)}]^2 + Re[k_{SPP,x}^2] + Im[k_{SPP,x}^2]) \\ & + \frac{2ADE_0}{\omega\epsilon_1} (\cos \theta (-Re[k_{SPP,y}^{(1)}] \cos \phi + Im[k_{SPP,y}^{(1)}] \sin \phi) \\ & + \sin \theta (-Re[k_{SPP,x}] \cos \phi + Im[k_{SPP,x}] \sin \phi)) \end{aligned} \quad (4.22)$$

where $\phi = (Re[k_{SPP,x}] - k_x)x + (Re[k_{SPP,y}^{(1)}] + k_y)y$ signifies the phase of the periodic intensity and $D = e^{-Im[k_{SPP,x}]x - Im[k_{SPP,y}^{(1)}]y}$ signifies the decay function of the SPP field.

One notable thing about the solution given by eq. (4.22) is that the function is time independent. This means that the periodic intensity maxima and minima positions stay localized at the surface. This is important to the dynamics of LSFL formation considering that we would expect a localized energy distribution for a selective ablation process to occur in the first place. The time independent nature of eq. (4.22) itself is contained within the derivation of the solution. The laser and the SPP both have the same driving frequency since they are coupled with one another.

Thus, the sum of their fields should have a constant magnitude⁴ at a point in space at all times.

For a normal incidence irradiation ($\theta = 0$), eq. (4.22) shows that the periodic intensity varies proportional to $-Re[k_{SPP,y}^{(1)}] \cos \phi + Im[k_{SPP,y}^{(1)}] \sin \phi$ (other terms either vanish or non-varying). And since $Re[k_{SPP,y}^{(1)}]$ is commonly much smaller than $Im[k_{SPP,y}^{(1)}]$ (for good conductors), we can safely neglect it in most cases. Therefore, the periodic intensity will have a phase of approximately $\phi = (Re[k_{SPP,x}] - k_x)x + (Re[k_{SPP,y}^{(1)}] + k_x)y$. The second part of the term vanishes at $y = 0$ and $k_x = 0$ for a normal incidence irradiation. Thus, the wavelength Λ of the periodic intensity distribution is found to be

$$\Lambda \approx \frac{2\pi}{k_{SPP,x}} = \lambda_{SPP} \quad (4.23)$$

The SPP wavelength λ_{SPP} has been predicted to correlate directly with the LSFL wavelength λ_{LSFL} [18, 19]. Therefore, eq. (4.23) implies that the periodic intensity distribution due to the SPP-Laser interference subsequently forms LSFL through selective ablation.

4.2.1 Laser Incidence Angle Dependence of LSFL Formation

Since the periodic intensity function has an effective wavenumber $2\pi/\Lambda = Re[k_{SPP,x}] - k_x$, λ_{LSFL} will be dependent upon the incidence angle. Note that the relation $2\pi/\Lambda = Re[k_{SPP,x}] - k_x$ is essentially equivalent to eq. (2.4) reported in the literature with only a difference in spatial reference frame. Using $k_x = k_0 \sin \theta$, we can then derive λ_{LSFL} as a function of θ as follows

$$\lambda_{LSFL}(\theta) = \frac{\lambda}{\frac{\lambda}{\lambda_{SPP}} - \sin \theta} \quad (4.24)$$

⁴In the case of an incident plane wave. For a Gaussian pulse, the magnitude would be modulated by the pulse envelope.

we define the range of the incidence angle to be $-90 \leq \theta \leq 90$. For $-90 \leq \theta \leq 0$, the laser field travels at an opposite direction to the propagating SPP field with respect to the surface. As a result, the net phase is varying at a higher frequency. The opposite happens for $0 \leq \theta \leq 90$, and a lower frequency spatial modulation is obtained.

4.3 Results and Discussions

4.3.1 Parameters at Silicon Melt Threshold

As outlined at the beginning of section 4.1, experimental and theoretical evidence have indicated that at least 10% of the valence electrons have to be excited at the threshold fluence of melt in semiconductors. We will use the value as a reference for the subsequent carrier dynamics calculations. This justification is reasonable considering the inherent uncertainties posed by the assumptions used in our model. Ultimately, we will discuss whether the calculated parameters using our model are within the reasonable limit of the values suggested in the literature.

The melt threshold of silicon used in the calculation is 0.2 J/cm^2 . Although this value is slightly above the average threshold value observed in our experiments at 780 nm wavelength (see fig. 3.1), it is still well within the range of the reported melt threshold in the literature [121]. The simulated pulse intensity follows a Gaussian profile as described by eq. (3.1). Figure 4.3 shows the calculated laser and material surface parameters at melt. A time step of 0.1 fs was used to achieve calculation convergence. Two main variables were optimized in the calculation to yield the results: TPA coefficient β and Drude scattering time τ_D . This is justifiable considering the value of β has not been well characterized in the literature at our irradiation wavelength, while, as explained in section 4.1.2.1, τ_D is treated as an effective value.

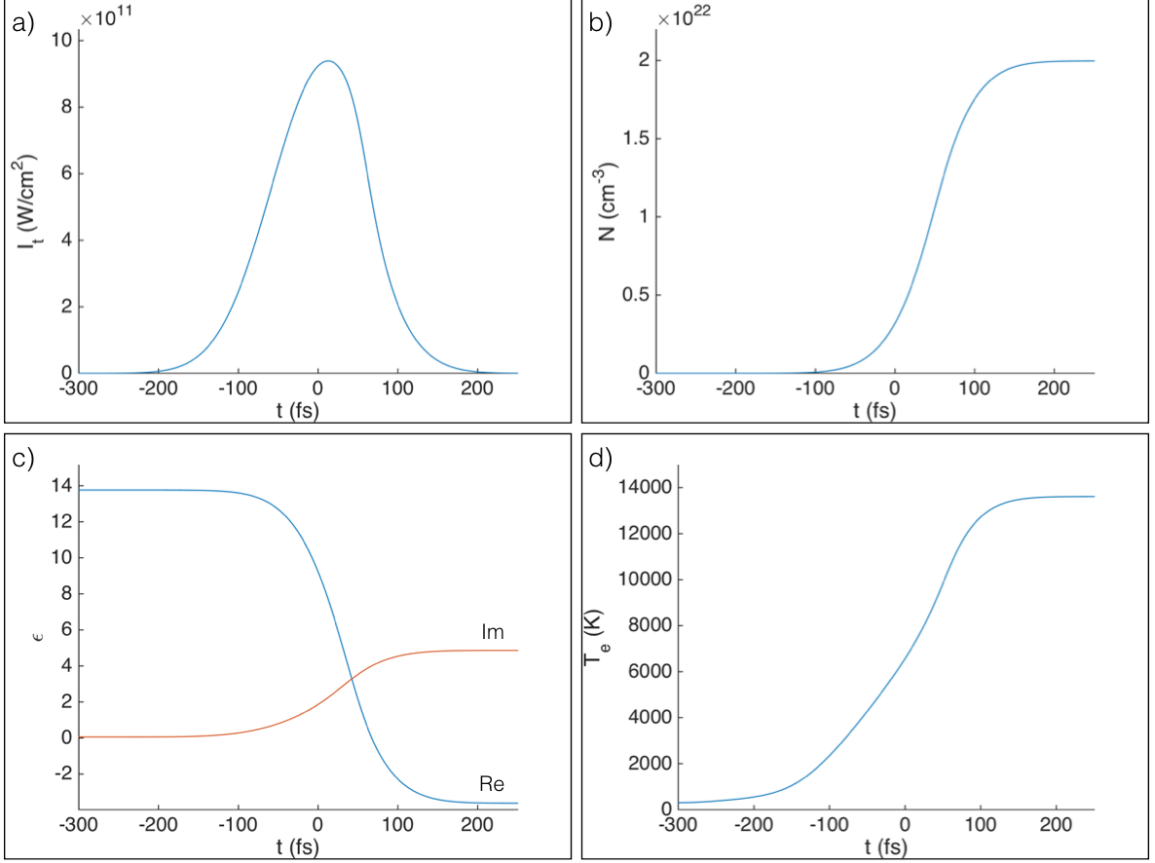


Figure 4.3: Simulated time dependent laser and material parameters at fluence = 0.2 J/cm^2 : a) transmitted laser intensity at the surface b) carrier density c) material's permittivity d) carrier temperature.

A maximum carrier density of $2 \times 10^{22} \text{ cm}^{-3}$ or 10% of valence electrons (fig. 4.3b) is achieved at $\beta = 15.5 \text{ cm/GW}$ and $\tau_D = 1.5 \text{ fs}$. The determined β value is larger than the currently accepted value in literature (see section 4.1). Several reasons may contribute to the overestimation. Firstly, since m_{opt}^* used in the calculation is only a function of temperature, it is underestimated at high N (section 4.1.2.1). This drives the plasma frequency ω_p to be higher than its actual value, which causes the calculated reflectivity to be effectively overestimated. Secondly, due to the 0-dimensional treatment of the calculation, we neglect the effect of spatially varying optical properties below the surface. Since a laser excited material is most reflective at the surface, omitting multiple scattering effects below the surface also leads to

an overestimated reflectivity [2]. In both cases, β becomes large to compensate for the loss of transmitted intensity. Nevertheless, $\beta = 15.5 \text{ cm/GW}$ at 780 nm is not unreasonable considering it still falls between the reported values at 620 nm and 800 nm [119–123].

As expected at the melt threshold, excited carrier density would reach a critical value where the optical properties of the surface turn metallic. This is indicated by a negative real part of the permittivity at the end of the pulse (fig. 4.3c). It has to be re-emphasized, however, that this is a purely carrier response contribution. The contribution of lattice motion to the change in the electronic structure is delayed, and in general mirrors the phonon emission timescale [1, 4]. Therefore, a pure carrier response formalism still gives a good enough approximation within the duration of the laser pulse. Finally, the carrier temperature at the end of the pulse is determined to be about 14000K (fig. 4.3d), which is within the carrier temperature range expected at the melt fluence of silicon [6, 141]. Considering that the chosen β and τ_D values yield fairly reasonable calculated materials parameters at melt, we will assume that the same values apply for carrier dynamic calculations involving LSFL formation.

4.3.2 Angle Dependent LSFL Formation: Experimental Results

Single pulse irradiations of silicon step edge surfaces at $F_p = 0.75 \text{ J/cm}^2$ yield LSFL of increasing periods at steeper incidence beam angles θ (fig. 4.4)⁵. This is consistent with the initial prediction given by eq. (4.24). Curiously, no LSFL form at $\theta = 50^\circ$. LSFL contrasts do return for θ larger than 50° . The explanation for the anomaly has yet to be determined. Dark horizontal contrasts are also observed to superimpose the formed LSFL structure. The nature of this contrast, too, requires further examination.

All of the LSFL form with surprisingly uniform periodicity (long range order)

⁵Note that the peak fluence is kept constant at varying incidence angle. The spot size of the beam varies with the incidence angle following $\pi w_0^2 / \cos \theta$, assuming an ideal elliptical beam shape.

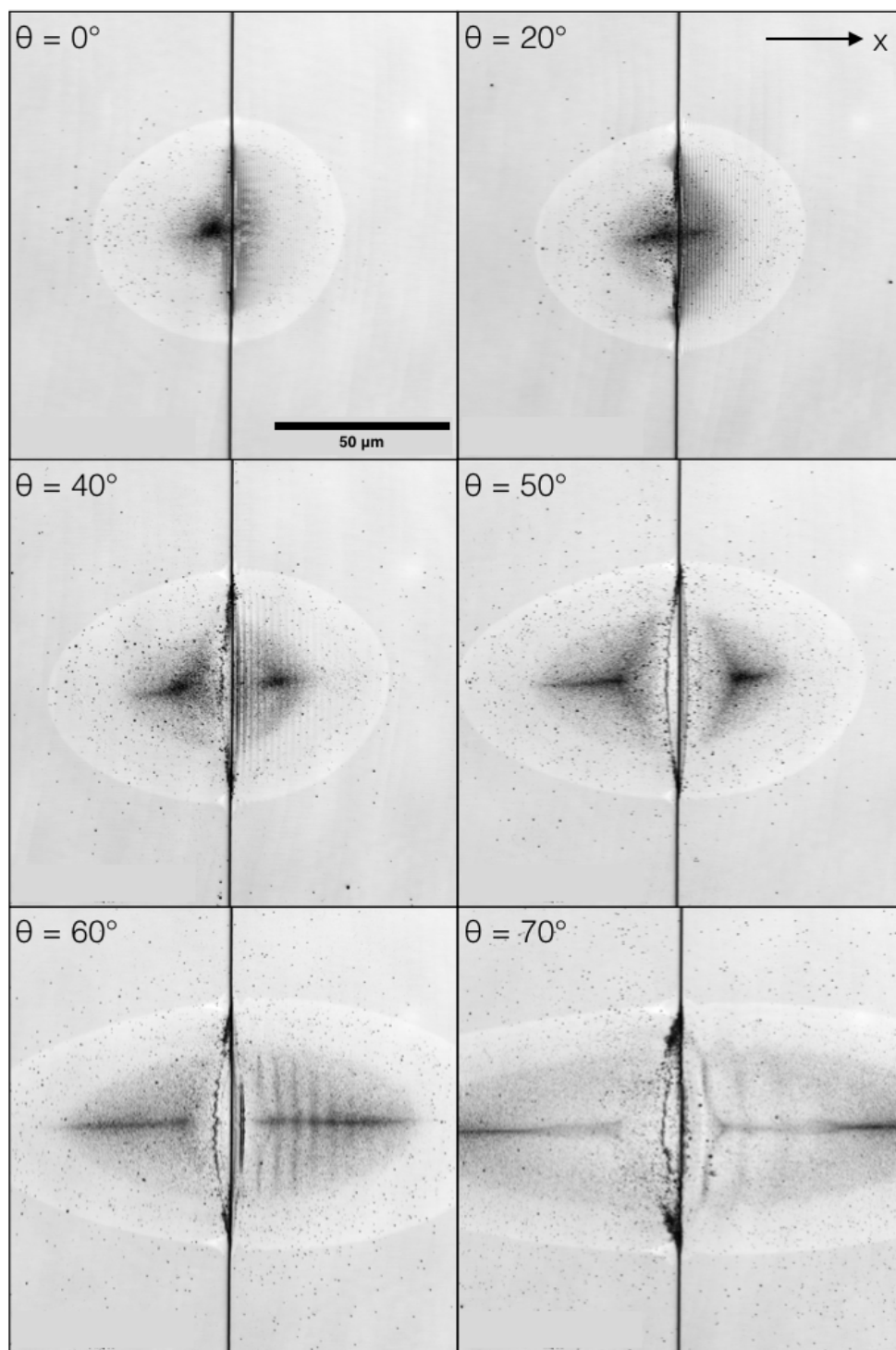


Figure 4.4: LSFL formation at various incidence angles θ on silicon step edge surface. The geometry of the irradiation follows the diagram shown by fig. 4.2 with $h = 585$ nm. The beam spot is centered at the step edge with a peak fluence of 0.75 J/cm^2 . Laser polarization is oriented along the x-direction.

despite a Gaussian distributed local fluence. This is a characteristic of SPP dispersion at high plasma frequency, where $k_{SPP,x} \rightarrow k_x$ as $Re[\epsilon_2] \rightarrow -\infty$ [100]. As such, λ_{SPP} becomes less effected by the change in fluence above a certain fluence regime. For the sake of simplicity, we will treat λ_{LSFL} as an average value. Assessment of the LSFL periodicities is done by 1-dimensional FFT analysis across the formed LSFL region. The detail to the FFT method used will be discussed further in section 5.1.1. Normal incidence irradiations form LSFL with a period of 753 ± 2 nm. While the largest LSFL period observed at $\theta = 70^\circ$ is 10 ± 2 μm .

4.3.3 Angle Dependent LSFL Formation: Comparison with Theoretical Model

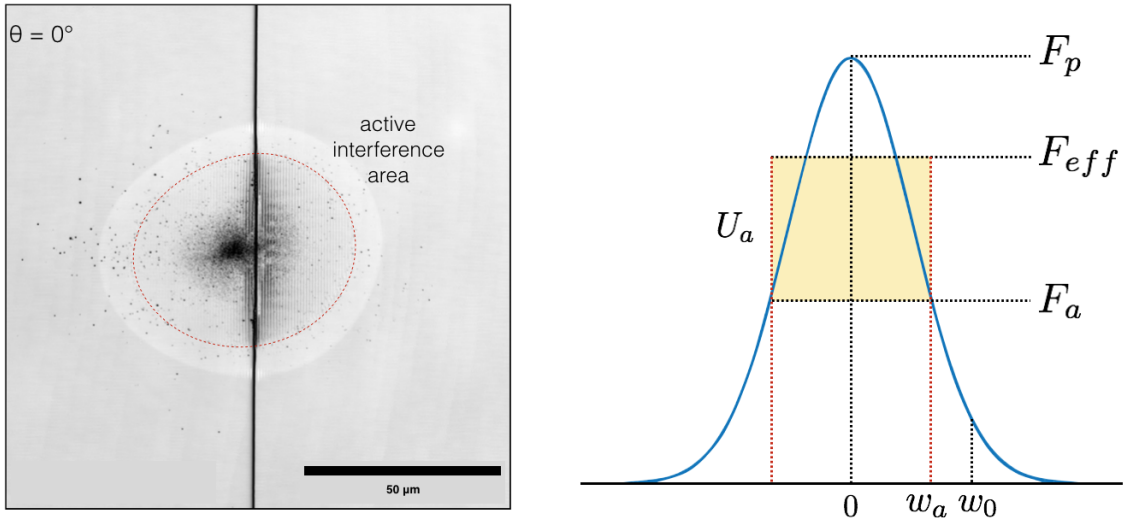


Figure 4.5: (left) Active interference area with average radius w_a and local fluence F_a at w_a . (right) Gaussian spatial profile showing the effective fluence F_{eff} .

Since the beam follows a Gaussian spatial profile, an effective fluence F_{eff} has to be defined to represent an average optical response leading to the LSFL formation. Hence, we specify an active interference area of radius w_a where LSFL formations occur (fig. 4.5). In this area we will assume a uniform optical properties across the active region. This is reasonable considering the slowly varying λ_{LSFL} observed.

The effective fluence F_{eff} is then defined as the average value of the Gaussian fluence profile within the active region:

$$F_{eff} = \frac{1}{2w_a} \left(\int_{-w_a}^{w_a} F_p e^{-2(\frac{x}{w_0})^2} dx \right) \quad (4.25)$$

where the integral inside the bracket represents the total energy per unit length U_a . In the case of normal incidence irradiation at peak fluence $F_p = 0.75 \text{ J/cm}^2$ and beam spot size $w_0 = 43 \text{ }\mu\text{m}$ (fig. 4.5), the active interference area radius $w_a = 26 \text{ }\mu\text{m}$. This gives an F_{eff} of 0.6 J/cm^2 . We will be using this effective fluence value in our theoretical LSFL wavelength calculation.

Following eq. (4.24), we note that λ_{SPP} will depend on the SPP dispersion relation given by eq. (2.11). However, as the dielectric constant continues to change with time due to the increase in carrier density (and consequently, the plasma frequency), the SPP wavelength would not have a well-defined value. In addition, using the excited permittivity calculated at the end of the pulse would not be reasonable⁶ considering that SPP and laser interference has to occur within a time window during the laser pulse. Hence, we define an effective time of interference τ_{eff} , when the optical properties would correlate to the observed LSFL wavelength.

Based on eq. (2.11), we can construct a map of all possible complex permittivity values that yield the observed LSFL wavelength of 753 nm at normal incidence irradiation (fig. 4.6). A plot of the time varying parametric ϵ_2 curve would ideally intersect a point corresponding to the observed SPP wavelength at τ_{eff} . Hence, we determine an ideal ϵ_2 of $-10.4 + 6.9i$ at $\tau_{eff} = -18 \text{ fs}$ for the interference. Note that τ_{eff} is very close to the peak intensity of the Gaussian pulse located at 0 fs, which is expected considering the largest energy absorption would occur near the peak intensity. As such, we will assume that the chosen τ_{eff} applies to all calculations at other incidence

⁶As in the case for the calculations done in Refs. [19, 142]

angles. The calculated ϵ_2 corresponds to a plasma frequency ω_p of 1.23×10^{16} Hz (or 0.08 fs), which is much faster than the laser pulse duration (150 fs). Therefore, SPP coupling within the pulse duration is reasonable.

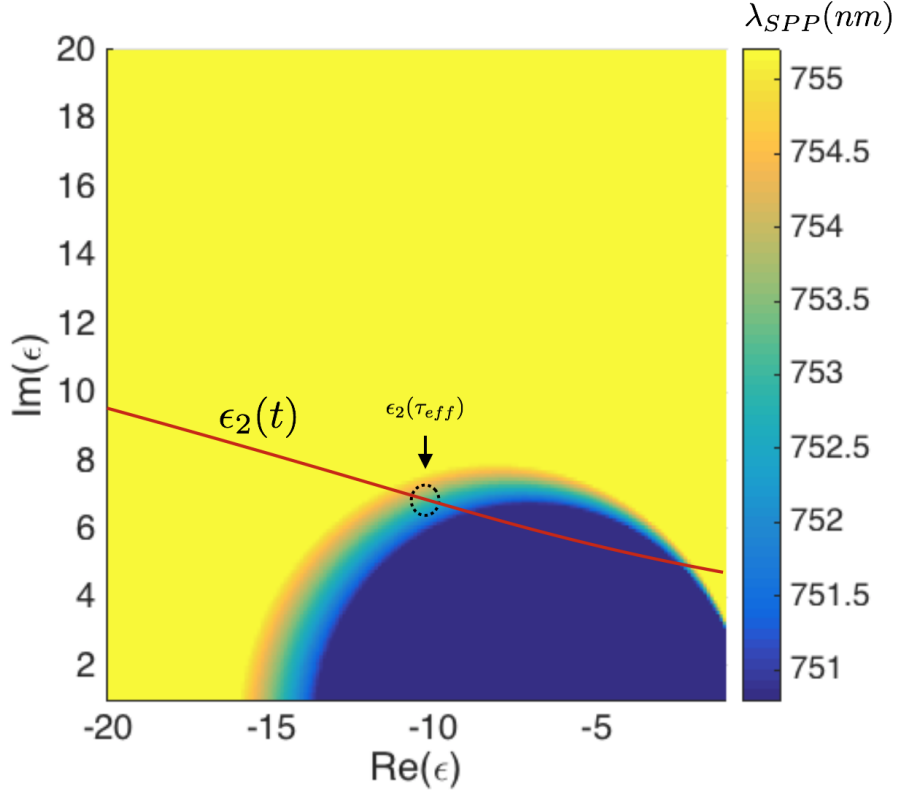


Figure 4.6: SPP wavelength map in the complex permittivity plane with the calculated time varying silicon permittivity ϵ_2 at $F_{eff} = 0.6$ J/cm² and normal incidence. The effective interference time τ_{eff} is determined to be at the point silicon permittivity curve yields the average observed LSFL (and SPP) wavelength (753 nm).

As we have discussed prior, calculations at other incidence angles are performed on the assumption that a constant τ_{eff} is determined empirically from observation at normal incidence irradiation. The calculated as well as the measured λ_{LSFL} are presented in fig. 4.7. Each measured data point contains an average from three sample images. The calculated λ_{LSFL} using our model show very good agreements with experiment, especially around $\theta = 10 - 30^\circ$. At larger θ , the calculated values become slightly underestimated. This might be due to several main reasons.

First, at our irradiation fluence, the simulated chemical potential μ reaches upwards of 3.5 eV at τ_{eff} . Hence, the band structure model used in determining the heat capacity of our carrier system becomes less adequate. Even more so at higher θ approaching the Brewster's angle, where the reflectivity approaches 0. A complete band structure model is needed to yield a more accurate result. However, this might not be practical either considering band structure modification occurs within the duration of the pulse due to many body interactions of the carriers [4].

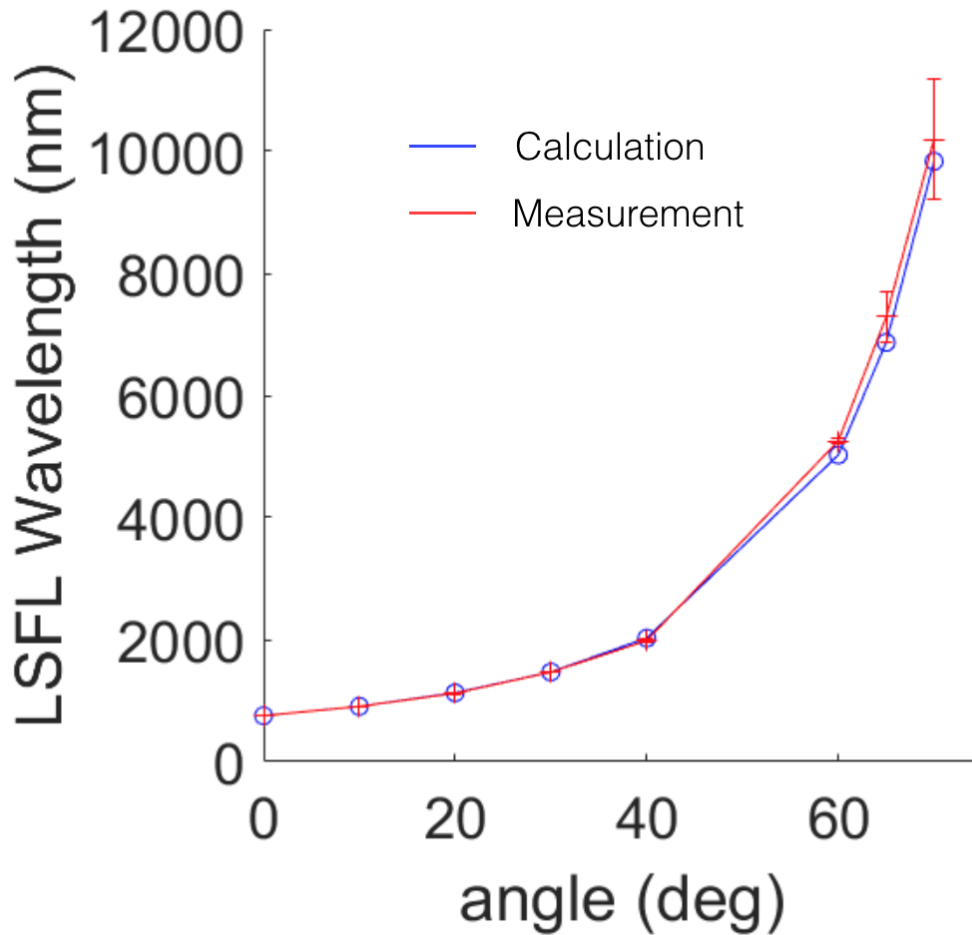


Figure 4.7: Theoretical and experimental LSLF wavelengths on silicon by single pulse irradiations at 780 nm.

Second, the implication of a dynamic band structure variation within the pulse duration may include additional carrier excitation processes. It has been shown that

electron tunneling may become important for laser intensity larger than 10^{12} W/cm² [4]. In addition, the contribution of impact ionization in our model may also change at higher excitation fluence, considering we only assume a constant ionization coefficient obtained from a linear fit (section 4.1.1).

Third, as we have discussed in section 4.3.1, β is likely to be overestimated in our model since we neglect spatial dependencies in our system. Finally, τ_{eff} is likely to be intensity, and consequently θ , dependent. Deriving its value from the data obtained at normal incidence irradiation would definitely cause increasing errors at larger θ . However, the experimental measurements already yield increasing uncertainties at larger θ to begin with. Hence, the assumption yields the minimum error possible. Since the LSFL formation dynamics is inherently complex and happens at an ultrafast timescale, an accurate treatment to the problem is still lacking and is limited by the current state of the art understanding of ultrafast laser-matter interactions. Nevertheless, our result shows that SPP laser interference gives an accurate prediction of the formed LSFL characteristics, which extends its validity as the dominant LSFL mechanism for semiconductors.

CHAPTER V

Control and Mechanisms of Low Spatial Frequency Laser Induced Periodic Surface Structures Formation using Plasmonic Microstructures

This chapter aims to demonstrate the extent of experimental control we can impose on LSFL formation based on the SPP-laser interference model outlined in chapter IV. So far, we have established a strong connection between the periodic intensity arriving on a silicon surface during an ultrafast laser pulse irradiation and the corresponding LSFL formation characteristics. Looking back at eq. (4.22), the periodically varying term has an amplitude that is proportional to the SPP magnetic field amplitude A . Therefore, we would expect a higher intensity LSFL structure when the SPP field is strong. Several factors affect the coupling of an SPP mode, one of them being the conductivity of the material. A good conductor such as gold satisfies the coupling requirement inherent in eq. (2.11) and therefore is an ideal plasmonic material. Note that $k_{SPP,x}$ is complex in metals, following a complex $\epsilon_2(\omega)$. Hence, the decay length of an SPP mode is described by the imaginary part of $k_{SPP,x}$, which is proportional to $Im[\epsilon_2(\omega)]$ (see [100] eq. 2.6). The intrinsic dielectric constant of gold at 780 nm is $-24.19 + 1.73i$ (interpolated from [116]), and since $|Re(\epsilon_2)| \gg Im(\epsilon_2(\omega))$, we would expect a low SPP loss and a strong SPP resonance for gold.

Following the above premise, gold mesa features are fabricated on silicon substrate as outlined in section 3.5.1. These structures serve as the initial SPP coupling surface. Single pulse exposures at 780 nm at the edge of the structure would yield LSFL, as observed in the case of silicon step edge structures. In this case, however, SPP field launched by the gold surface yields substantially stronger surface modulations. We will further observe the effect of structure geometry, polarization orientation, and fluence on the formed LSFL characteristics. Regarding irradiation polarization, we will observe LSFL formations where SPP are not possibly coupled to the materials surfaces. In that case, we argue that near field diffraction becomes the dominant LSFL formation mechanism instead. Finally, we will examine 2-dimensional periodic structure formations using the interference of multiple SPP coupling sources with the laser; furthering the extent of our surface modification capabilities.

5.1 TM Polarized Irradiations of Gold Mesa on Silicon

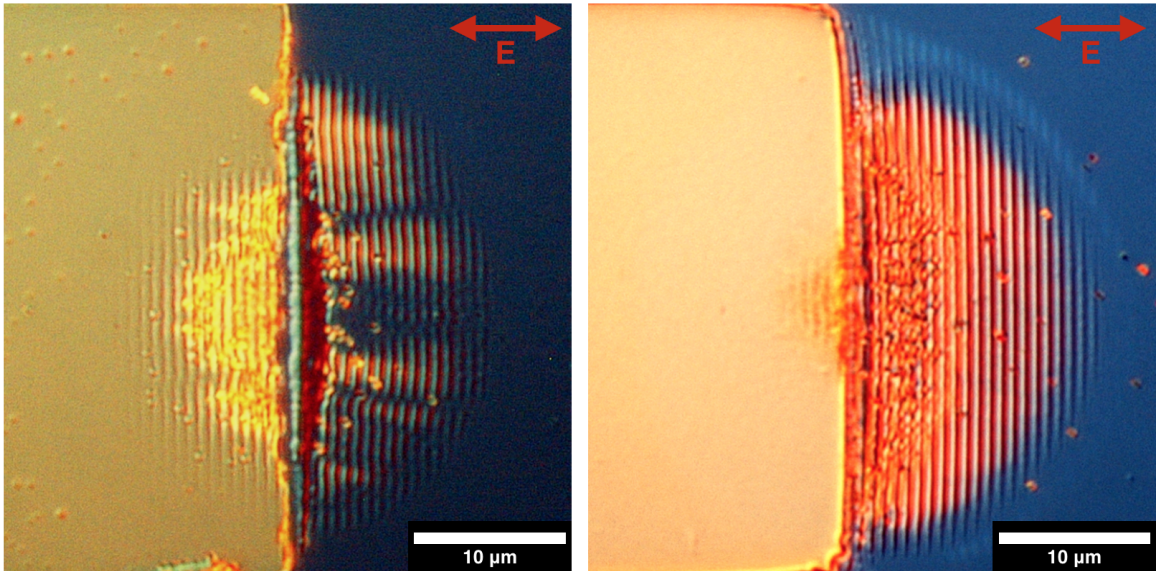


Figure 5.1: LSFL formation on 110 nm (left) and 720 nm (right) tall Au mesas on Si using single pulse TM polarized beam irradiations at $F = 0.75 \text{ J/cm}^2$. The beam is centered at the edge of the gold mesas.

We begin by examining single pulse irradiations with polarization perpendicular to the mesa structure’s edge. In this case, the magnetic field is parallel to the step edge. Therefore, we designate the familiar transverse magnetic (TM) term to the condition. LSFL formations on 110 nm and 720 nm tall mesas at $F = 0.75 \text{ J/cm}^2$ and normal incidence are shown in fig. 5.1. The formed LSFL amplitudes on the silicon substrate are on the order of 100 nm [76]. A massive increase in the LSFL visibility and area of formation on silicon can be observed as we go from 110 nm to 720 nm tall mesa. Curiously, a seemingly opposite behavior occurs on gold. We will discuss this phenomenon further in section 5.1.4.

5.1.1 Periodicity Analysis

A fast Fourier transform (FFT) is used to obtain the periodic distributions of the formed LSFL patterns. Calculations are performed along the wavevector of the LSFL at multiple adjacent positions. The FFT algorithm for the analysis used is shown in appendix D. It is important to note the limited capabilities of FFT analysis in this case. The frequency resolution Δf of a Fourier transform is denoted by:

$$\Delta f = \frac{1}{X} \tag{5.1}$$

where X is the total length of the sample. Due to the relatively small region of LSFL formed (spot size dependent), the frequency resolution of the Fourier transform will also be small. To resolve the issue, the frequency resolution can be increased by applying zero-padding to the data. Caution must be exercised, however, since zero padding inherently applies a sinc function convolution to the frequency domain representation. In addition, zero-padding would not add resolving power for distinguishing nearby hidden frequency peaks. Nevertheless, the method is valid for resolving LSFL periodicity considering that LSFL wavelengths observed in this study vary slowly

with local fluence.

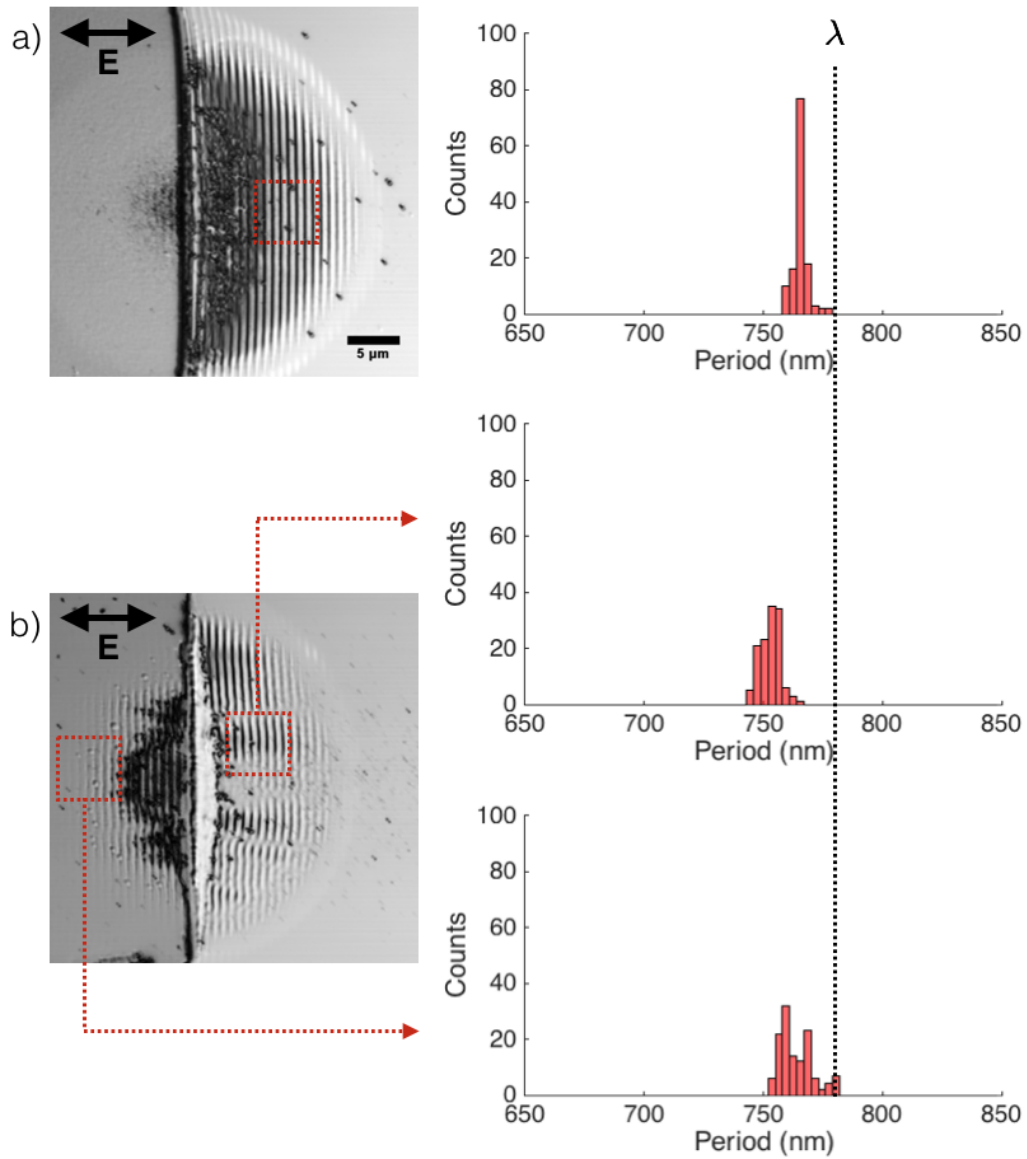


Figure 5.2: LSFSL period distributions resulting from single pulse TM-polarized irradiations ($F = 0.75 \text{ J/cm}^2$) of a) 720 nm tall mesa b) and c) 110 nm tall mesa. Periodicity analysis are performed at the boxed region. A faint LSFSL pattern is apparent on the gold surface in a). Unfortunately, its corresponding periodicity could not be resolved.

The calculated period distributions of the formed LSFSL in fig. 5.1 are presented in fig. 5.2. An average LSFSL period of $765 \pm 3 \text{ nm}$ on silicon is found for the case of the 720 nm tall mesa (fig. 5.2a), which is larger compared to the LSFSL period

observed on the silicon step edge irradiated at the same fluence (section 4.3.2). The increase in LSFL period in the presence of gold mesa structure can be attributed to the field enhancement produced at the gold edge. Localized plasma resonance produced by metals have been well-observed to increase the optical absorption of neighboring semiconductors [143, 144]. Hence, as the plasma frequency of silicon increases due to enhanced carrier generation rate, the SPP and subsequent LSFL wavelengths would also increase.

Figure 5.2b shows an average LSFL period of 753 ± 4 nm on silicon for 110 nm tall mesa irradiation. The decrease in period is directly related to the smaller gold step edge surface area, in which less energy would be confined by the surface plasmon mode resulting in a weaker field enhancement. A consequently weaker absorption is also evident when looking at the less well-defined optical contrast produced by the structure as well as smaller the LSFL area formed. Meanwhile, the LSFL period on gold is found to be 764 ± 7 nm (fig. 5.2b). The period is consistent with the theoretical intrinsic gold SPP wavelength at 780 nm, which equals to 764 nm (using eq. (2.11)).

5.1.2 TM Irradiation Frequency Domain Simulation

In order to further investigate the effect of gold mesa geometry on the intensity of LSFL formation, we utilize a finite element method (FEM) based electromagnetic field solver (COMSOL). The details of the method are outlined in section 3.7. As the calculations are performed in the frequency domain, material parameters are kept constant. An excited silicon permittivity of $-10.4 + 6.9i$ (at $F = 0.75$ J/cm²) is obtained from section 4.3.3. While, the permittivity of gold is kept at its intrinsic value ($-24.19 + 1.73i$). This is a reasonable assumption considering that gold carrier density increases by only a factor of ~ 1.5 at this fluence [145]. The incident beam waist w_0 used in all calculations is 10 μ m. Figure 5.3 shows the resulting periodic

intensities at the gold and silicon surfaces near the step-edge at various mesa heights. The periodic intensity is obtained from the x-component of the resulting electric field, which is the strongest field component interfering with the SPP.

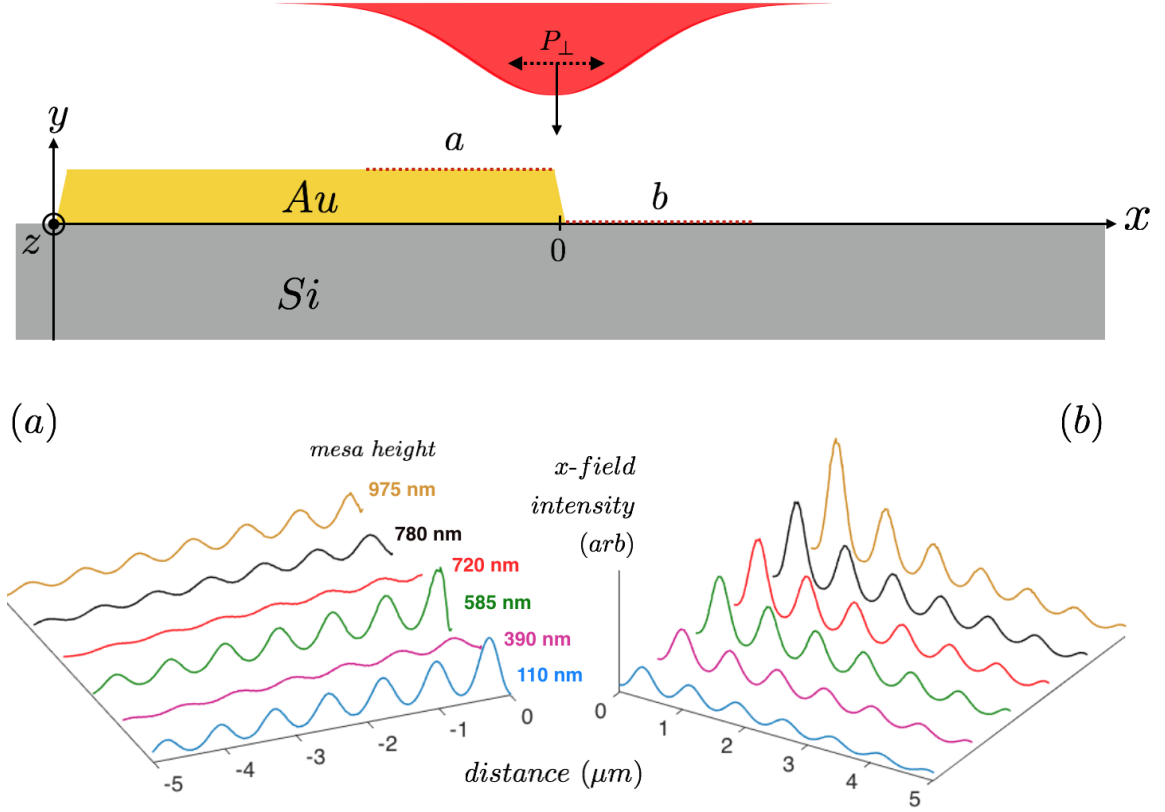


Figure 5.3: TM irradiation simulation results at various mesa heights showing relative intensity of the x-field on the a) gold and b) silicon surfaces. An increase in the periodic intensity amplitude is observed on the silicon surface at taller mesa height. Meanwhile, periodically varying amplitude is observed on the gold mesa surface.

Two different behaviors are shown on the silicon and gold surfaces. First, an increasing periodic intensity amplitude is observed on silicon surface as mesa height increases (fig. 5.3b). The result is consistent with the increase in the formed LSFL intensity on silicon at 720 nm shown in fig. 5.1. On the gold surface, a periodically varying amplitude is observed as mesa height increases (fig. 5.3b). The intensity amplitude of 110 nm tall mesa is shown to be significantly larger than 720 nm tall

mesa. This, again, matches with our experimental result, as LSFL formation has been shown to be stronger on the gold surface at 110 nm compared to 720 nm tall mesas (fig. 5.1). Note that, in both cases, the periods of the intensities are always less than the wavelength of the laser, consistent with the SPP-laser interference hypothesis.

5.1.3 SPP Coupling Mechanism on the Step Edge Structure

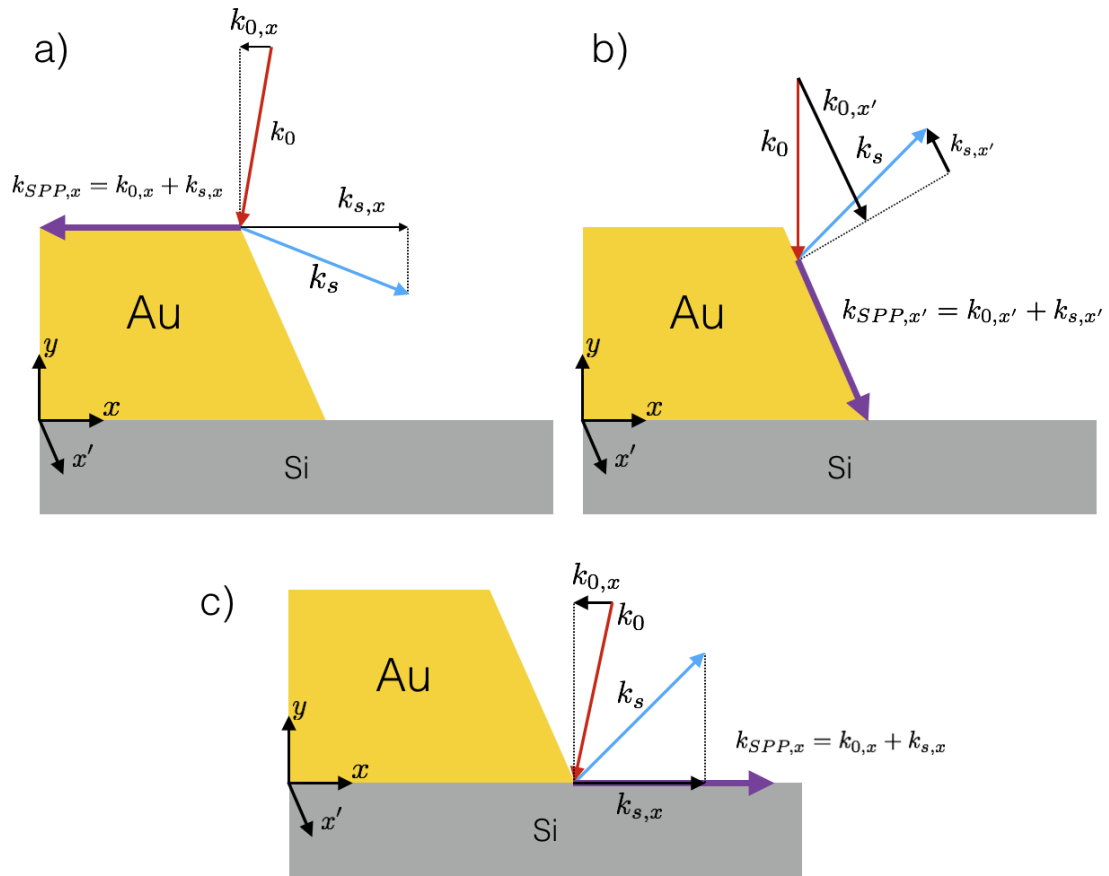


Figure 5.4: Diagrams showing possible SPP coupling mechanisms on gold mesa structures and a silicon substrate. In each case, k_{SPP} is larger than k_0 prompting a need for extra momentum provided by scattered light. The x' -axis is parallel to the step edge surface. Note that incident beam is focused. Hence, it has an incident wavevector distribution (i.e. not just at normal angle) related to the beam spot size. In other words, since photon travels straight in a homogeneous medium, a normal incident beam with finite spot size may transfer momentum parallel to the surface and is depicted by the non-normal incident wavevectors in a) and c).

SPPs have been well-known to couple at surface features or discontinuities [146]. Here, we present a simplified model of the SPP coupling processes at the step-edge feature to physically interpret the experimental and simulated results we have discussed so far (fig. 5.4). Since the SPP wavenumber k_{SPP} is always larger than the laser wavenumber k_0 (see section 2.3.2), additional momentum has to be supplied by way of light scattering for the SPP mode to couple. We utilize a simple conservation of momentum argument to explain the process. Scattered beam propagating in the opposite direction relative to the SPP propagation would yield additional momentum k_s ¹. Hence, the change in momentum provided by the incident and scattered beam would match the momentum required for SPP coupling.

In fig. 5.4a, SPP coupling occurs at the edge of the gold surface leading to the condition $k_{SPP,x} = k_{0,x} + k_{s,x}$ (note that since $k_{0,x}$ and $k_{s,x}$ have opposite directions against each other relative the coupled surface, the two wavenumbers are summed instead of subtracted), in which an SPP propagates along the negative x-axis. Another coupling process occurs on the gold step edge surface yielding SPP propagation in the positive x'-axis, which is parallel to the step edge surface (fig. 5.4b). Hence, additional local field will be concentrated at the silicon-gold interface. Empirically speaking, the coupled SPP field strength would be proportional to the metallic surface area [143, 144]. This explains the stronger field enhancement produced by a taller mesa structure. As the silicon surface undergoes metallic transition and is able to support SPP modes, coupling may also occur at the silicon-gold edge (fig. 5.4c). The direction of the SPP propagation is reversed on the silicon surface due to reflection at the step-edge, whose coefficient increases with step-edge height [147].

From the three coupling scenarios presented, SPP field strength at the silicon surface is hypothesized to increase with mesa height, which is exactly what we have

¹The scattered beam can be viewed as the consequence of interfering Huygens wavelets that needs to satisfy the boundary conditions imposed by the conducting step-edge geometry. Since the scattering surface is discontinuous, scattered beams will be generated in all directions.

observed empirically and through simulations. The SPP field strength at the gold surface, however, is affected more by the phase matching condition imposed by the step-edge geometry, which we will discuss shortly. Note that the coupling mechanisms outlined above is very much analogous to the grating assisted SPP coupling process. In the case of grating coupling, however, coherent scattering leads to well-defined diffraction orders.

5.1.4 Specular Phase Matching Condition

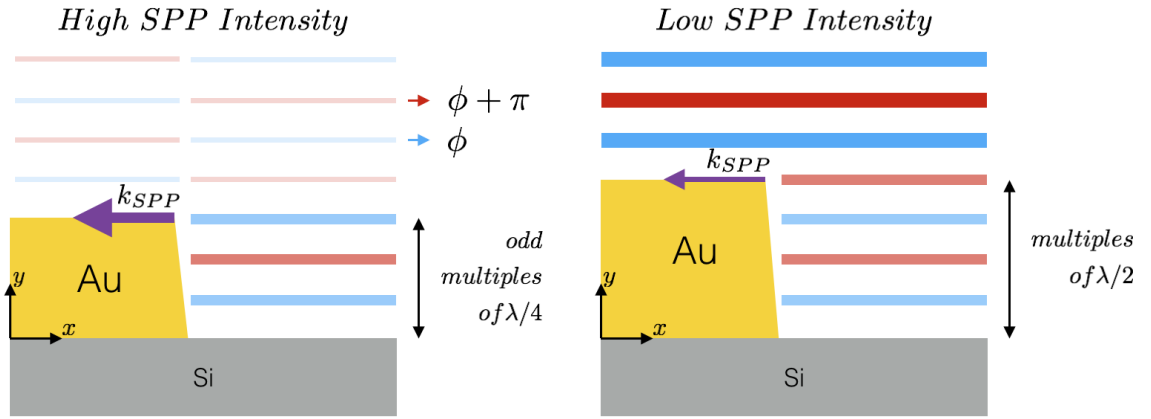


Figure 5.5: Diagram of phase matching conditions at various mesa heights leading to variations in the coupled SPP intensity. The blue and red lines represent the phases of the specularly reflected beams.

Corresponding to the simulated varying periodic intensity field on the gold surface, we construct an argument based on the phase matching of the specularly reflected beams from the gold and silicon surfaces² (fig. 5.5). Depending on the mesa height, the reflected beams would differ in phase. Hence, when the mesa height is close to $n\lambda/4$, where n is a positive odd integer, the reflected beams would interfere destructively. From a conservation of energy point of view, this leads to the increase in the scattered light intensity in all directions. Consequently, according to section 5.1.3, the coupled SPP field intensity would become larger. If, instead, the mesa height is close to

²Assuming that the silicon substrate is in a transient metallic state.

$n\lambda/2$, where n is a positive integer, the reflected beams would interfere constructively resulting in a weaker coupled SPP field intensity.

In both cases, the SPP intensity will be proportional to the formed LSFL amplitude as we have observed in fig. 5.1. Note that in the case of 110 nm tall mesa irradiation, the large calculated periodic intensity amplitude is not solely responsible for the enhanced LSFL formation on gold. Femtosecond laser damage threshold of gold thin films have been observed to decrease below the bulk value for thicknesses below 180 nm, due to a limited hot electron diffusion [148]. As such, a larger damage area is expected to begin with. However, we still observed a significant attenuation of LSFL intensity at 720 nm tall mesa above the gold damage threshold (~ 0.7 J/cm² at 780 nm), which matches with the simulated results. As a side note, the height dependencies we have established above are not exact, considering the non-ideal step-edge geometry of the mesa as well as the plane wave formalism used in the argument. Nevertheless, the formalism has been demonstrated to be valid in the case of mesa height below λ .

5.2 TE Polarized Irradiations of Gold Mesa on Silicon

When the beam polarization is oriented parallel to the mesa edge, a reduction in LSFL contrasts are observed for both 110 nm and 720 nm irradiated samples (fig. 5.6). In this case, ideally, SPPs would not be coupled (see section 2.3.2. As such, SPP-laser interference should not occur. We do, however, observe a well-defined LSFL formation on the 720 nm mesa sample. This suggests that other mechanisms not involving SPPs are taking place. Near field diffraction as a formation mechanism has been suggested by prior studies [22, 76]. Hence, in this section we will present extensions to the hypothesis.

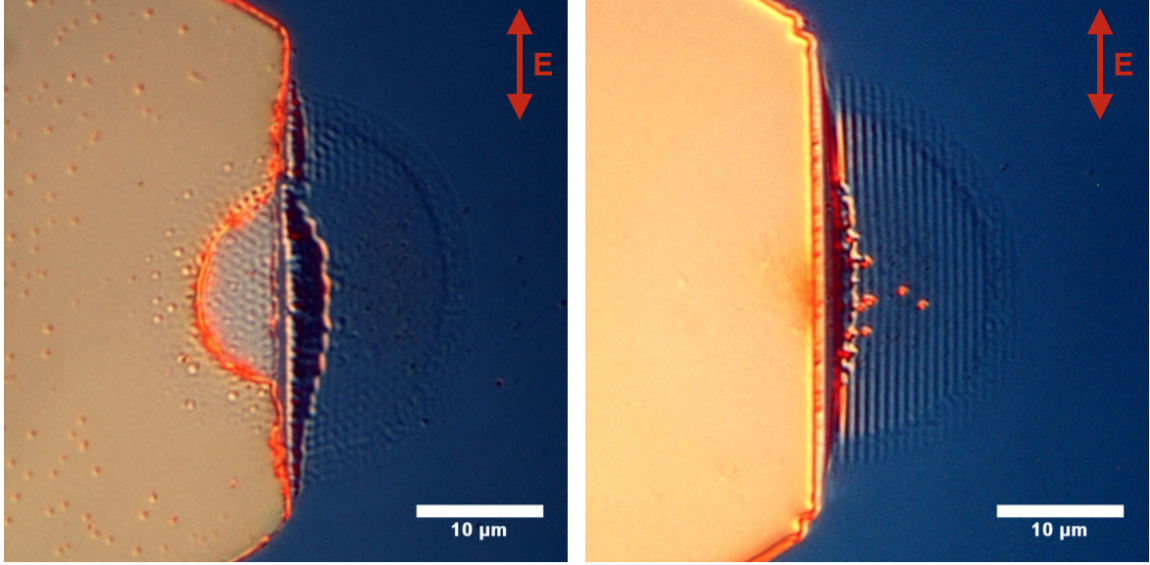


Figure 5.6: LSFL formation on 110 nm (left) and 720 nm (right) tall Au mesas on Si using single pulse TE polarized beam irradiations at $F = 0.75 \text{ J/cm}^2$. The beam is centered at the step edge of the gold mesa.

In the case of a 110 nm tall mesa sample, a clear LSFL pattern is not apparent. Instead, we observe crosshatch periodic contrasts on the edge of the ablation crater on silicon as well as the gold surface. The crosshatch patterns, however, are the result of multiple SPP interference, which are coupled at the edge of the hexagonal mesa sample (this effect has been shown in [76]). Accordingly, this effect is not apparent in the case of a 720 nm tall sample due to the weak SPP coupling at the gold surface (section 5.1.4).

The LSFL period distribution of the 720 nm mesa sample is shown in fig. 5.7. The distribution shows an average period of $778 \pm 4 \text{ nm}$, which is comparatively larger than the TM polarized irradiation result (fig. 5.2). Note that periodic components larger than the laser wavelength are measured. As we already discussed prior, this is improbable in the case of SPP-laser interference. We would then suggest that near field diffraction becomes the dominant mechanism of the LSFL formation.

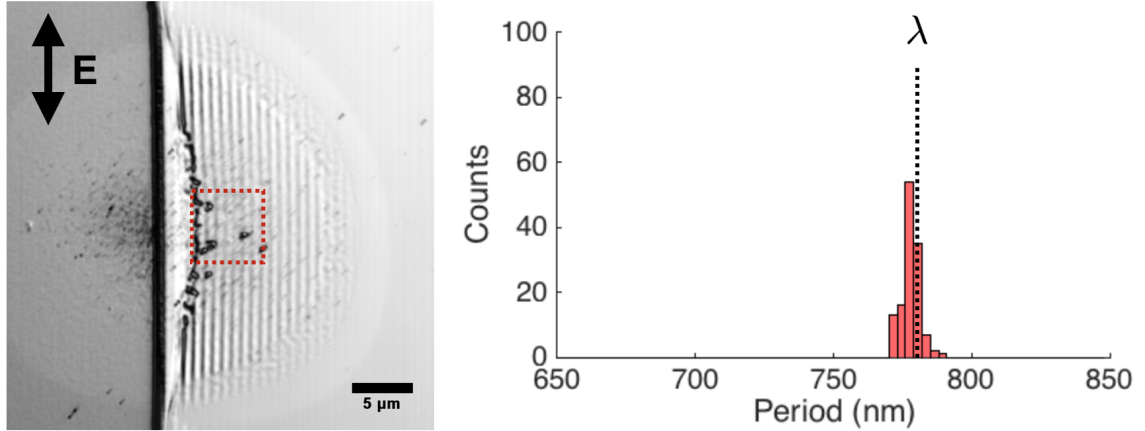


Figure 5.7: LSFL period distribution on silicon resulting from single pulse TE-polarized irradiations ($F = 0.75 \text{ J/cm}^2$) of a) 720 nm tall mesa. Periodicity analysis are performed at the boxed region. LSFL is shown to have periodic components larger than the laser wavelength.

5.2.1 TE Irradiation Frequency domain Simulation

Frequency domain simulations are performed with the laser polarization oriented along the z -axis fig. 5.8. The relative intensity is calculated from the z -component of the electric field. The resulting periodic intensity on silicon shows an increase in amplitude as the mesa height increases. For a mesa height of 110 nm, a periodic signal is barely apparent due to the short propagation distance to the silicon surface. For 720 nm tall mesa calculations, we observe a larger but quickly decaying periodic intensity amplitude. In general, the relative amplitudes observed in this case is much weaker than the TM simulation results, which is consistent with our experimental observations. The periods of the varying intensity are nonuniform and generally larger than the laser wavelength, which is characteristic of a diffraction pattern. It is then very likely that the formed LSFL characteristic we have observed in fig. 5.7 on silicon is related to the near field diffraction. As a side note, the calculated intensity on the gold surface shows no periodic variation (not shown), which indicates ordinary laser absorption.

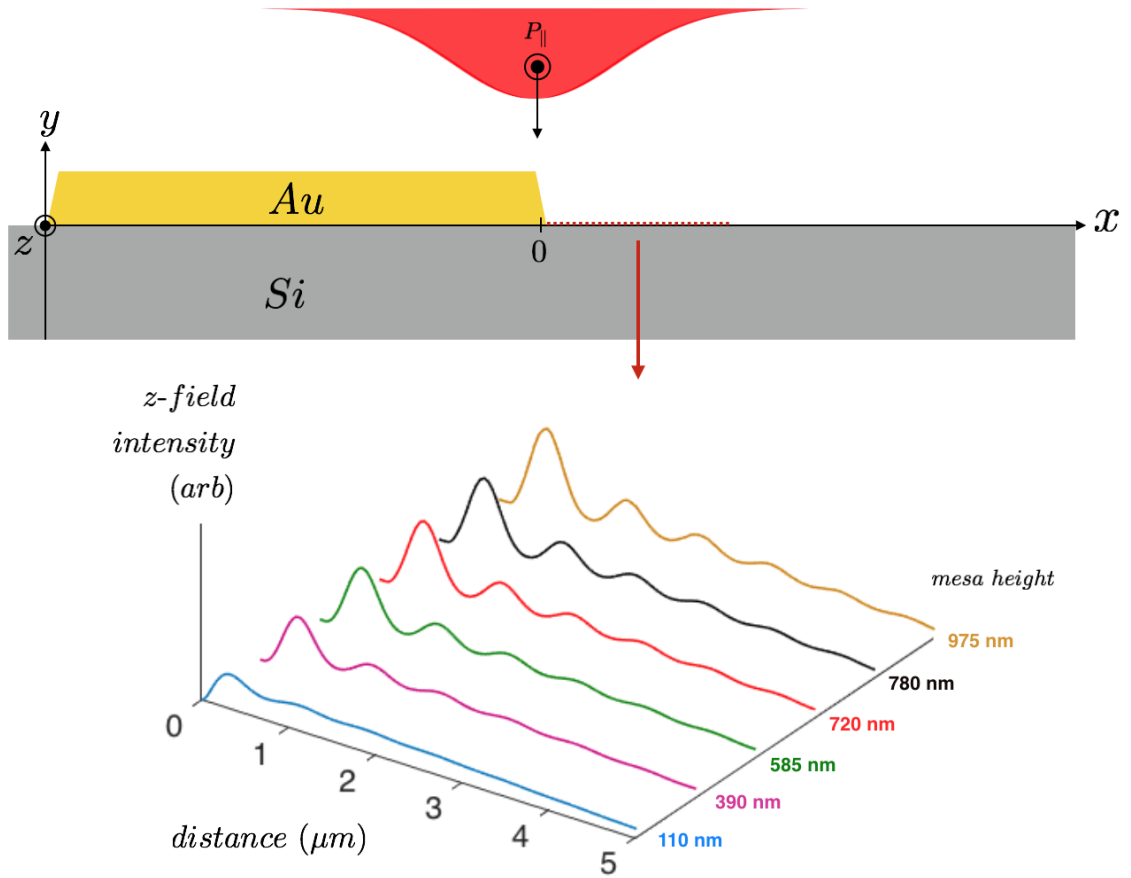


Figure 5.8: TE irradiation simulation results at various mesa heights showing relative intensity from the electric field along the z -direction on the silicon surface. An increase in the periodic intensity amplitude is observed as the mesa height increases. No periodic intensity variation is observed on the gold surface (not shown).

5.3 Fluence Dependence of the Formed LSFL Wavelength

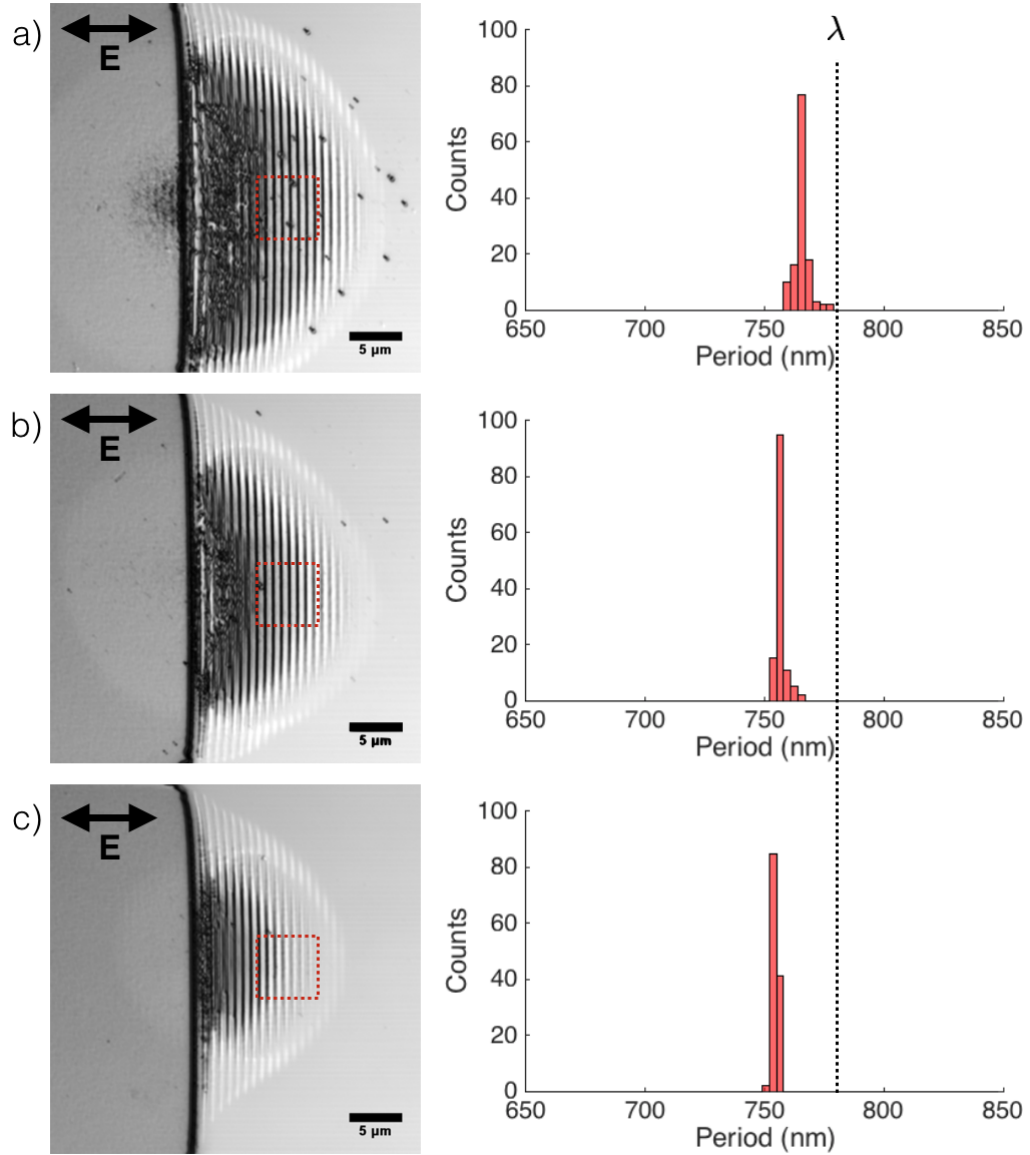


Figure 5.9: LSFL period distributions calculated at the boxed region for 720 nm tall Au mesa single pulse TM-polarized irradiation at a) $F = 0.75 \text{ J/cm}^2$, b) $F = 0.5 \text{ J/cm}^2$, c) $F = 0.3 \text{ J/cm}^2$. Period increase proportional to the beam fluence is observed.

According to eq. (2.11), the SPP wavelength, λ_{SPP} , will depend on the excited permittivity ϵ_2 of the material. As we have established in section 4.1.2, ϵ_2 varies with the degree of carrier excitation dictated largely by the free carrier response. In general,

as $Re[\epsilon_2]$ decreases so will $k_{SPP,x}$, which implies that λ_{SPP} and, subsequently, λ_{LSFL} would increase with fluence. Figure 5.9 shows LSFL formed at 3 different fluences by TM irradiation of 720 nm tall mesa samples. The evaluated regions are placed at the same distances away from the step edge³. Here, we observe the predicted increase in λ_{LSFL} as fluence increases. The average LSFL periods measured are 754 ± 1 nm, 757 ± 2 nm, and 765 ± 3 nm for $F = 0.3, 0.5,$ and 0.75 J/cm², respectively. Again, the periods are consistently found to be shorter than the laser wavelength.

In the case of TE irradiated samples, an opposite LSFL formation behavior on silicon is observed as fluence increases (fig. 5.9). The LSFL formed with average periods of 802 ± 4 nm, 787 ± 9 nm, and 778 ± 4 nm for $F = 0.3, 0.5,$ and 0.75 J/cm², respectively. The LSFL wavelengths are then generally equal or larger than the laser wavelength, reemphasizing the difference in the LSFL formation mechanism compared to the TM irradiation cases. The nature of the decreasing LSFL periods as fluence increases, however, is still unclear, since the varying intensity periods produced by near field diffraction typically only depends on the distance between the observation plane and the diffracting surface [99]. Nevertheless, a strong correlation of the formation mechanism to near field diffraction is apparent when taking into account the experimentally observed characteristics and previously discussed simulation results.

³This is done to ensure that the increase in local fluences between the three instances stays proportional to the increase in peak fluence. Unfortunately, the LSFL regions near the mesa edge are mostly not resolvable due to surface damage.

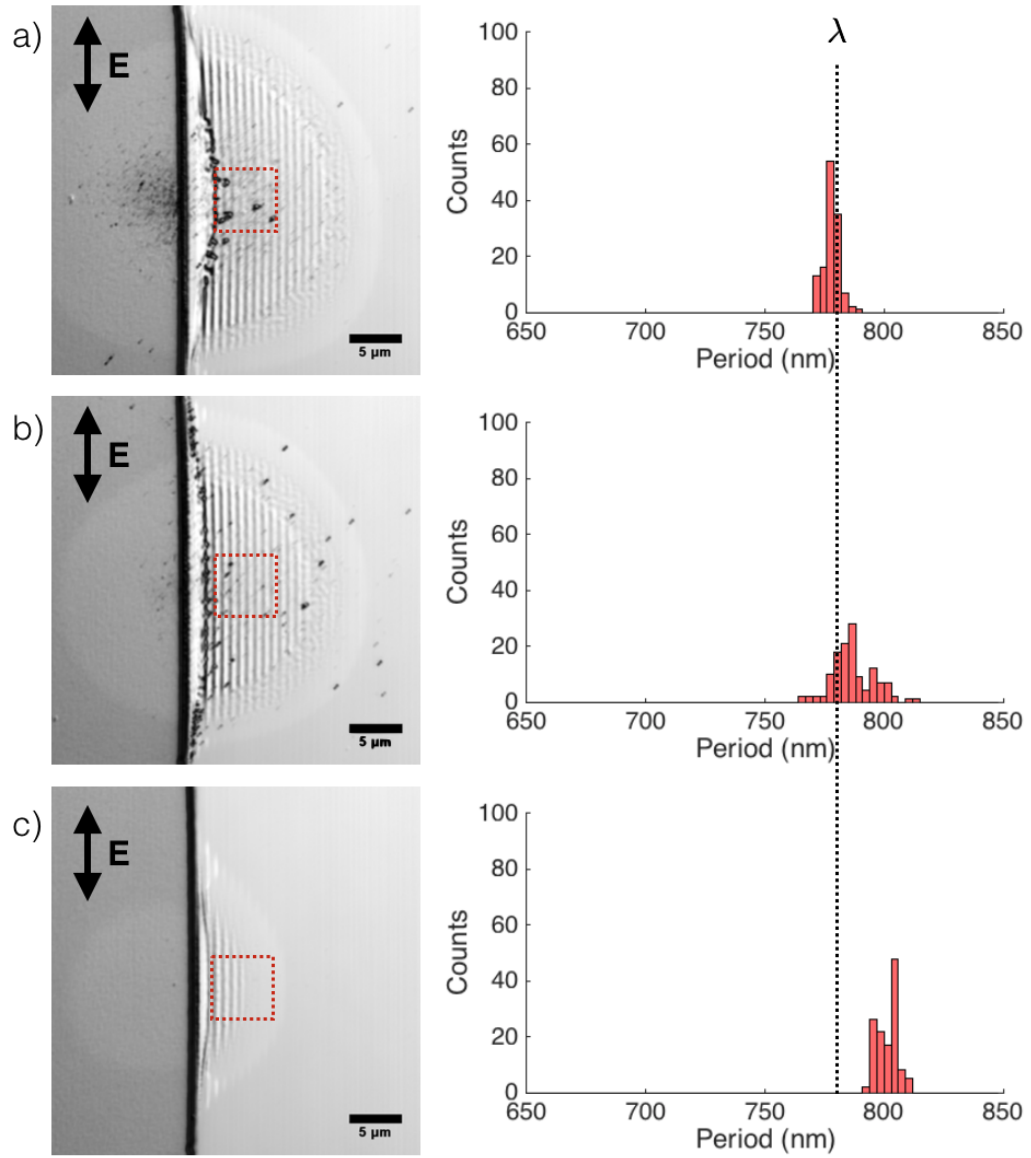


Figure 5.10: LSLFL period distributions calculated at the boxed region for 720 nm tall Au mesa single pulse TE-polarized irradiation at a) $F = 0.75 \text{ J/cm}^2$, b) $F = 0.5 \text{ J/cm}^2$, c) $F = 0.3 \text{ J/cm}^2$.

5.4 2-Dimensional Periodic Structure Formations

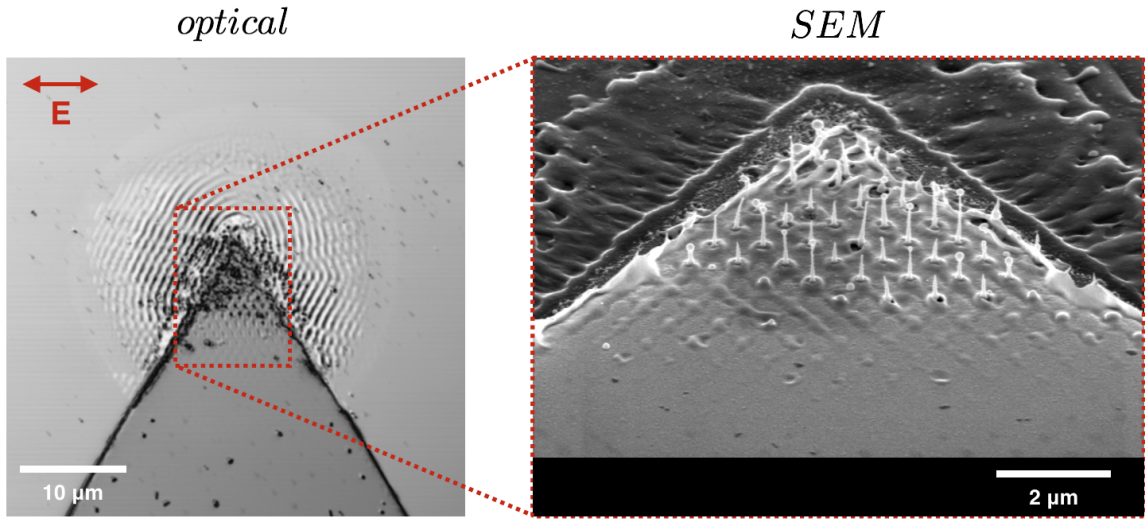


Figure 5.11: 110 nm tall triangular gold mesa irradiation at $F = 0.5 \text{ J/cm}^2$ showing the formation of periodic nanojets due to multiple SPP interference with the laser. The beam position is centered at the apex of the gold structure. SEM tilt is at 60° from surface normal.

Expanding on the theory of SPP-laser interference, the presence of multiple SPP sources has the possibility to yield 2-dimensional periodic structures. Figure 5.11 shows a single pulse irradiation of multiple gold edges oriented at angle $\gamma = 60^\circ$. Crosshatch patterns can be observed on the silicon substrate surface indicating SPP propagations from the two edges. This is possible due to SPP transmission across a shallow step-edge [147]. More interestingly, however, the crosshatch pattern form on gold shows a remarkable periodic alignment. Upon further observation using SEM, periodic gold nanojets are shown to form with heights reaching up to $1 \mu\text{m}$.

The formation of nanojets has been well-observed on thin gold films using single pulse femtosecond laser irradiations [149–151]. Possible formation mechanisms of the structure include Marangoni convection [149] and cavitation bubbles near free liquid surface [151]. In addition, nanojets has also been shown to form on surface plasmon-enhanced hotspots on gold [150]. In general, the irradiated gold films in the literature

and in our study show clear indications of melt. For instance, the formation of droplets at the end of the jets structure can be explained by the surface tension of liquid gold phase [152]. Considering the height of the nanojets, the irradiated gold has to stay molten for an extended period of time relative to the ultrafast timescale in order for a significant degree of convection to take place. This is reasonable considering, in gold, energy is transferred to the lattice relatively slowly due to a weak electron-phonon coupling [153]. Moreover, thermal diffusion to the bulk is also limited by the heterogenous interface. Hence, thermal energy is confined within the small volume of the film, which creates large compressive stress following a rapid expansion of the molten state. The above dynamics is further supported by a time-resolved study done by Unger et al., in which nanojets are observed to form after about 250 ns [151]. The observed formation time falls within the melt solidification timescale of ultrafast laser irradiated materials (fig. 2.1).

5.4.1 Multiple SPP-Laser Interference

The relative total intensity produced by interfering SPP and laser fields follows:

$$I_t \propto |\vec{E}_t|^2 \quad (5.2)$$

where $\vec{E}_t = \vec{E}_{SPP}^{(1)} + \vec{E}_{laser}$ is the total field. We can expand the formalism given by eq. (4.20) for the laser field and eq. (2.8a) for the SPP field (in the dielectric medium) to include additional z-coordinate. Hence, the incident laser field can now be written as:

$$\vec{E}_{laser}(x, y, z, t) = (E_0, 0, 0)e^{i(-k_y y - \omega t)} \quad (5.3a)$$

$$\vec{E}_{laser}(x, y, z, t) = (0, 0, E_0)e^{i(-k_y y - \omega t)} \quad (5.3b)$$

where $k_y = k_0 = 2\pi/\lambda$. Equation (5.3a) and eq. (5.3b) denotes incident fields with polarizations along the x and z-axes, respectively. SPP launched from multiple edges oriented at an angle γ is illustrated in fig. 5.12c. In the illustration, both SPP fields propagate in an opposing direction to each other on the x-z plane, while the laser field is coming into the page along the y-axis.

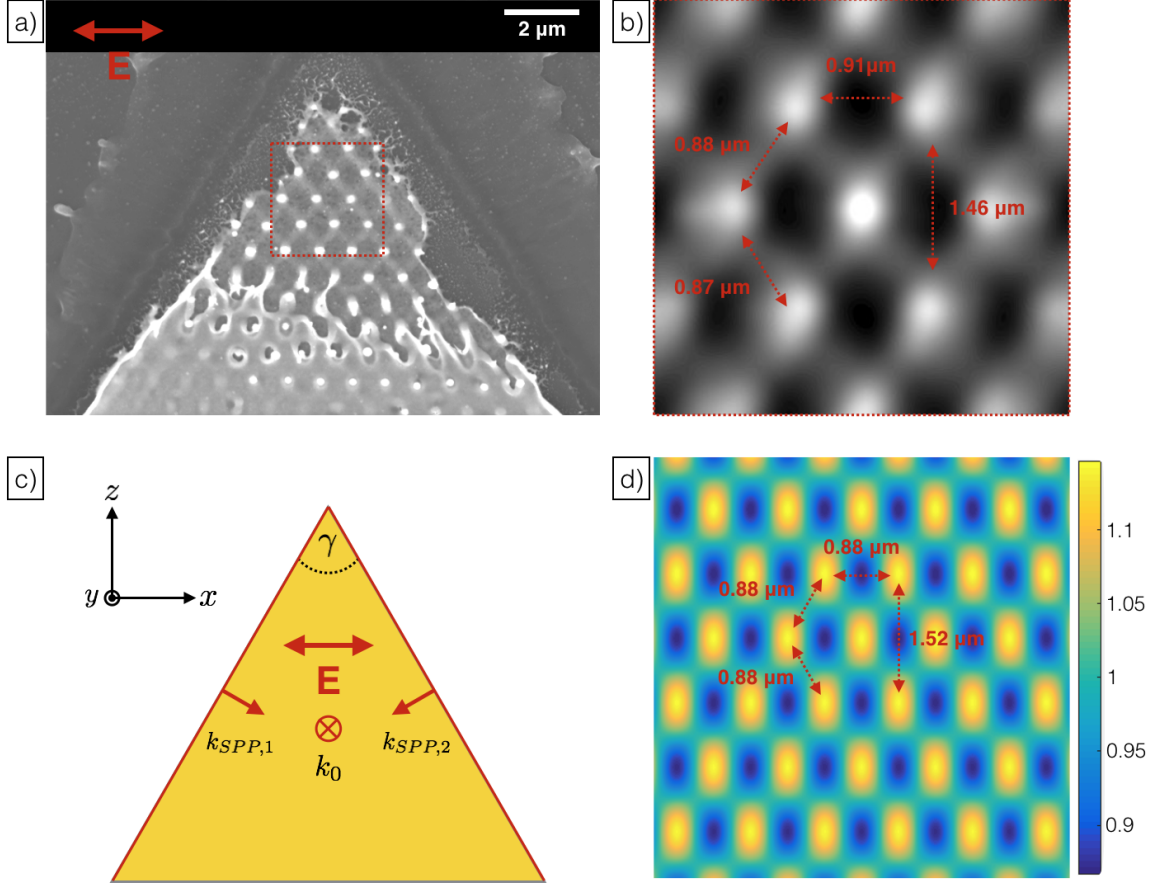


Figure 5.12: a) Nanojets formation on 110 nm tall triangular gold mesa at $F = 1 \text{ J/cm}^2$ using a single pulse irradiation. The beam position is centered at the apex of the mesa. b) Autocorrelation of the periodic structure performed on the boxed region showing hexagonal alignment. c) Multiple SPP-laser interference scheme. d) Corresponding intensity distribution obtained from interference calculation showing similar hexagonal pattern as the nanojets. The colorbar denotes intensity normalized to the laser amplitude.

In accordance with fig. 5.12c, the SPP fields can then be derived as follows:

$$\begin{aligned} \vec{E}_{SPP,1}^{(1)}(x, y, z, t) = & \\ - \frac{Ac}{\omega\epsilon_1\sqrt{1.086}} & (k_{SPP,y}^{(1)} \cos(\gamma/2), -k_{SPP,x} \cos(\gamma/2) + k_{SPP,z} \sin(\gamma/2), -k_{SPP,y}^{(1)} \sin(\gamma/2)) \\ & e^{i(k_{SPP,x}x + k_{SPP,y}^{(1)}y + k_{SPP,z}(z - z_{ub}) - \omega t)} \end{aligned} \quad (5.4a)$$

$$\begin{aligned} \vec{E}_{SPP,2}^{(1)}(x, y, z, t) = & \\ - \frac{Bc}{\omega\epsilon_1\sqrt{1.086}} & (k_{SPP,y}^{(1)} \cos(\gamma/2), -k_{SPP,x} \cos(\gamma/2) + k_{SPP,z} \sin(\gamma/2), -k_{SPP,y}^{(1)} \sin(\gamma/2)) \\ & e^{i(-k_{SPP,x}(x - x_{ub}) + k_{SPP,y}^{(1)}y + k_{SPP,z}(z - z_{ub}) - \omega t)} \end{aligned} \quad (5.4b)$$

where,

$$k_{SPP} = \frac{2\pi}{\lambda} \left(\frac{\epsilon_{gold}(\omega)}{1 + \epsilon_{gold}(\omega)} \right)^{1/2} \quad (5.5a)$$

$$k_{SPP,x} = k_{SPP} \cos(\gamma/2) \quad (5.5b)$$

$$k_{SPP,z} = -k_{SPP} \sin(\gamma/2) \quad (5.5c)$$

$$k_{SPP,y}^{(1)} = -\left(\left(\frac{\omega}{c} \right)^2 - (k_{SPP})^2 \right)^{1/2} \quad (5.5d)$$

x_{ub} and z_{ub} denote the upper boundaries of the simulated x and z coordinates. An extra term $c/\sqrt{(1.086)}^4$ is added to eq. (5.4a) and eq. (5.4b) in order to normalize the SPP fields to the laser field amplitude E_0 . The intensity distribution $I_t(x, z)$ at the gold surface calculated using $E_0 = 1$, $A = B = 0.2^5$, and $\gamma = 60^\circ$ is shown in fig. 5.12d. The intensity is obtained from the total field component parallel to the x-z plane (parallel to the polarization of the laser). Figure 5.12a shows another gold nanojets formation at $F = 1 \text{ J/cm}^2$ and $\gamma = 60^\circ$. A corresponding autocorrelation image

⁴ c is the speed of light

⁵Assuming a coupling efficiency of $A^2/E_0 \sim 4\%$ at each edge.

is presented in fig. 5.12b, which includes average nanojets spacings measurement. The alignment and spacings of the nanojets show very good agreements with the theoretically calculated intensity distribution.

Further irradiation of hexagonal ($\gamma = 120^\circ$) and square ($\gamma = 90^\circ$) gold mesas show nanojets formation of different 2D periodic alignments (fig. 5.13). Again, the measured spacings of the nanojets matches reasonably with the theoretical calculation in both cases. Note that in fig. 5.13a, the calculated intensity distribution is identical to the one showed in fig. 5.12 due to the symmetry of the calculation. In addition, the calculated periodic intensity amplitudes reach up to 35% of E_0 using the parameters specified, which would be sufficient to induce localized hotspots resulting in the nanojets formation.

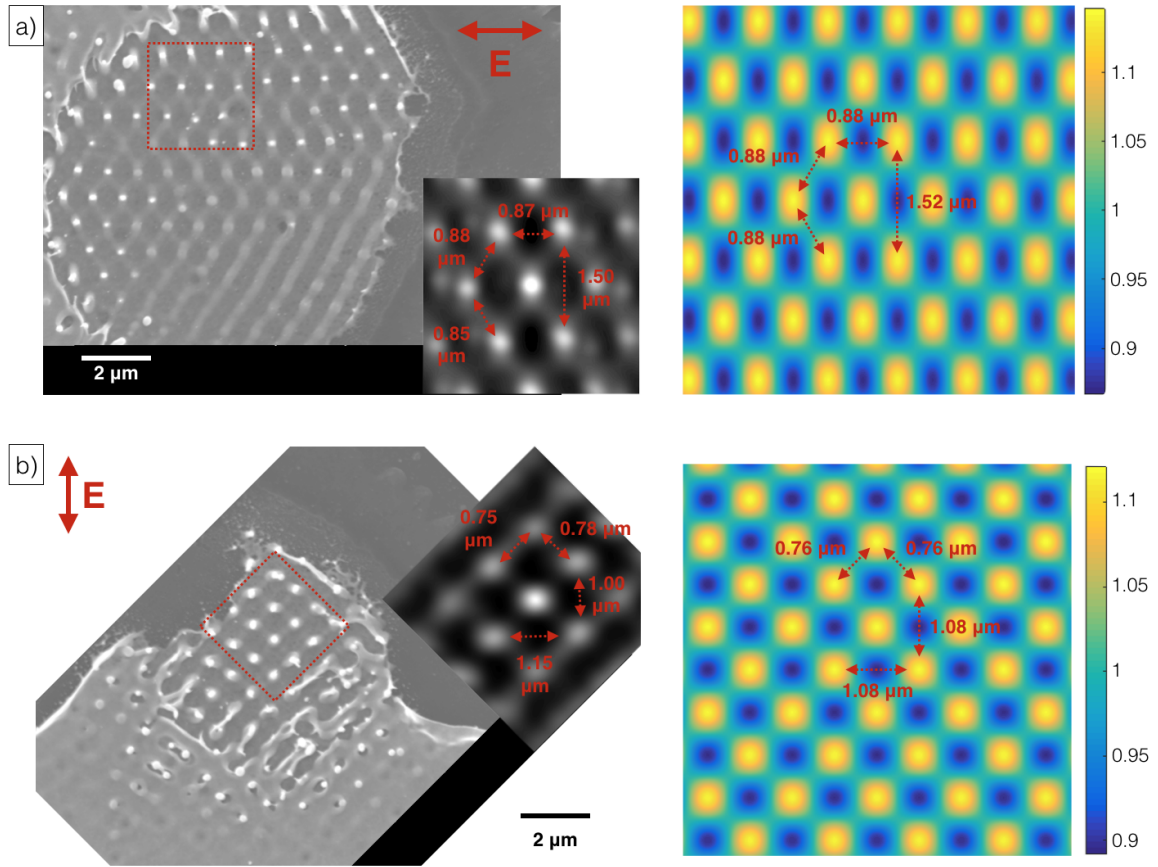


Figure 5.13: Nan jets formation on 100 nm tall a) hexagonal b) square gold mesas at $F =$ a) 1 J/cm^2 b) 0.75 J/cm^2 using single pulse irradiations. The beam position is centered at the corner of the mesas. The corresponding autocorrelation and theoretical intensity distribution are shown. The colorbar denotes intensity normalized to the laser amplitude.

CHAPTER VI

High Spatial Frequency Laser Induced Periodic Surface Structure Formation in Silicon: Laser Coupling with Point Defect Induced Islands

HSFL occurrence on silicon is rarely reported in the literature. The earliest observation of silicon HSFL is reported by Costache et al. using an 800 nm laser with 100 fs pulse duration and 1kHz repetition rate [95]. In the study, HSFL is reported to form parallel to the laser polarization. The details of the report, however, were not well described. Only a single low resolution SEM image of the nanostructure is presented. Within our study, we have not been able to reproduce the HSFL observed in [95] using similar laser parameters and irradiation conditions¹. Note that our experiments were only done in a high vacuum ($\sim 10^{-5}$ mbar) instead of an ultra-high vacuum. In a more recent study, parallel HSFL formation is reported using an 800 nm high repetition rate (76 MHz) laser [154]. The HSFL orientation, however, has been shown to be a function of raster irradiation speed, which adds another parameter to the already complicated formation mechanism.

The first observations of perpendicular HSFL formation on silicon were done by

¹The equivalent reported irradiation parameters for HSFL formation in [95] are: $F = 0.065$ J/cm², 60000 exposures. Silicon (100) surface were treated with HF to remove initial native oxide layer. The irradiations were done under ultra-high vacuum condition (10^{-9} mbar)

Le Harzic et al. [89, 97].² This is accomplished using an 80 MHz repetition rate femtosecond laser in the NIR wavelength range. Since then, the formation of perpendicular silicon HSFL have been reproduced in other studies, all using high repetition rate (MHz range) femtosecond lasers [154, 158]. The corresponding mechanism of formation, however, is still largely under debate. Suggested mechanisms include second harmonic generation, surface plasmon generation, and heat accumulation.

From what we have discussed so far, the underlying consensus would be that the formation of HSFL on silicon requires either high repetition rate or environmental conditions besides ambient air. This certainly brings up the question as to why only those specific parameters result on silicon HSFL formations. In this chapter, we report yet another HSFL formation on silicon. The significance of our result lies in the observation of a direct correlation between the formation of HSFL with the growth of a novel precursor nanostructure below the threshold fluence of melt. So far, the nanostructure is observed to form in both air and vacuum using a 1KHz repetition rate laser at 390 nm wavelength but not at 780 nm. We propose that the increase in the photon energy at 390 nm results in a more efficient point defect generation due to the dominance of single photon absorption across the direct gap of silicon.

6.1 The Effect of Wavelength

Following single pulse laser irradiation above the ablation threshold, optical images of silicon show ablation crater and melt morphologies. A more distinct melt contrast is apparent at 390 nm wavelength compared to 780 nm (fig. 6.1b). The contrast indicates light scattering from a larger amorphized volume, which corresponds to a larger absorption length. This is rather counterintuitive since the linear absorption

²Irradiations were performed in air. As such, oxide layer is formed and has to be removed to observe HSFL. On a side note, HSFL has previously been observed on Si for irradiations in liquid environments [155–157]. The HSFL formation dynamics in liquid, however, is beyond the scope of this thesis.

length at 390 nm is 15 times smaller than at 780 nm to begin with. However, as we have already discussed in section 4.1, absorption becomes strongly nonlinear at 780 nm near the melt threshold, which contributes to a decrease in the absorption length. In addition, since the effective nonlinear absorption coefficient is intensity dependent, energy is spread out over a larger volume within the pulse duration resulting in an inefficient melting. In the case of 390 nm irradiation, strong linear absorption may already confine absorbed energy at a smaller volume. This, in turn, increases the average amount of energy absorbed per atom. As such, a higher degree of structural amorphization may occur at a lower intensity near the surface.

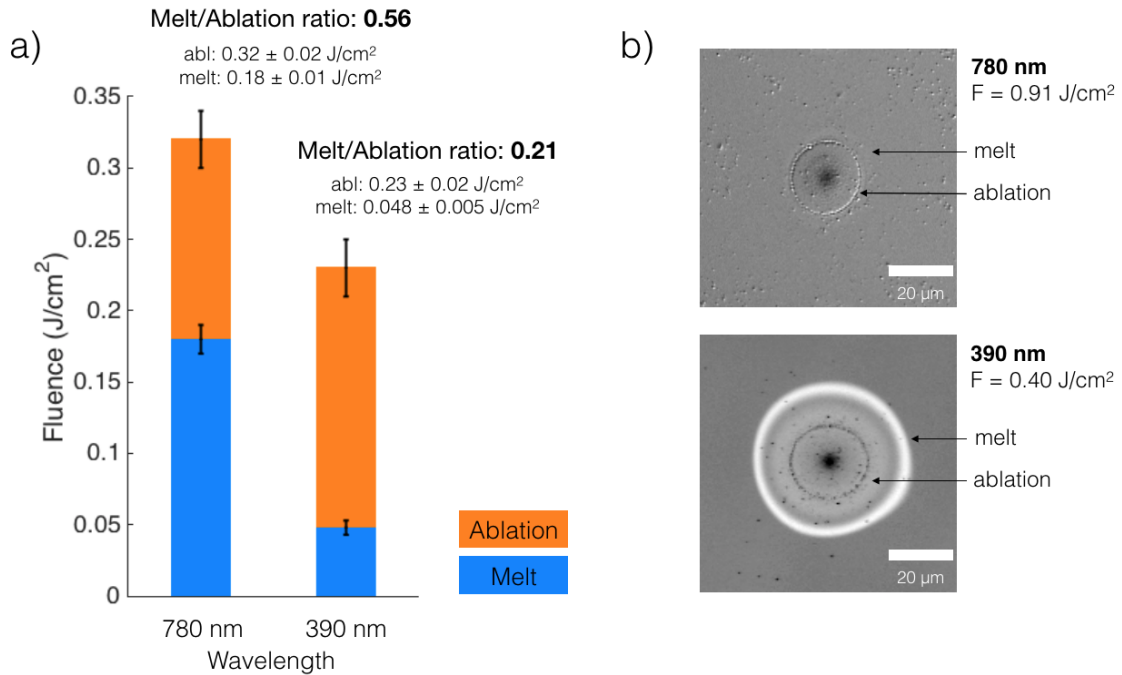


Figure 6.1: a) Ablation and melt thresholds of silicon at 390 nm and 780 nm wavelengths. A distinct ablation/melt threshold ratio is apparent between the two wavelengths. b) Optical images of single pulse laser damage morphology showing ablation crater and melt contrast.

A decrease in the single pulse ablation and melt thresholds of silicon is then expected at 390 nm compared to 780 nm wavelength. Surprisingly, however, the decrease in the thresholds observed in our experiment is also accompanied by a factor

of two decrease in the melt to ablation ratio (fig. 6.1a). While ultrafast laser ablation on silicon is a rapid thermal process [103] (section 2.1.1), the accompanying ultrafast laser melting has been strongly hypothesized to be non-thermally induced [159]. The decrease in the melt to ablation ratio then implies that more efficient non-thermal melting dynamics occur at 390 nm compared to 780 nm. Considering that the photon energy at 390 nm (3.18 eV) is comparable to the band gap energy at the Γ -point and along the L-valleys (~ 3.4 eV [160]), significant promotion of electrons to the anti-bonding states may occur without momentum transfer, taking into account band-gap renormalization [5]. Hence, the excited carrier density required for non-thermal melting³ can be achieved at a lower intensity [159], consistent with our earlier discussion, since TPA is no longer required for a direct band transition. Note again that at fluences above the ablation threshold, rapid phase transformation leading to material removal is still thermally induced. Therefore, the ablation threshold depends more on the total energy rather than the density of the excited carriers, which further explains the decrease in melt/ablation thresholds ratio at 390 nm.

6.1.1 Point Defect Generation

Below the melt threshold, a significant disruption to the lattice may still occur, characterized by the band-gap collapse phenomenon [1]. Although reversible lattice deformation is observed after a single pulse irradiation below melt [8, 44], it has been suggested that point defects may still be generated and accumulate over multiple pulses [10, 11]. The proposed mechanism for laser induced point defect generation is depicted in fig. 6.2.

A decrease in the bonding state charge density due to carrier absorption weakens the attractive part of the interatomic potential [6]. At the same time, the charge density populates the interstitial region of the lattice [4, 6]. While the lattice is

³For now, it is reasonable to assume that at least 10% of the valence electrons has to be excited for non-thermal melting to occur at 390 nm irradiation.

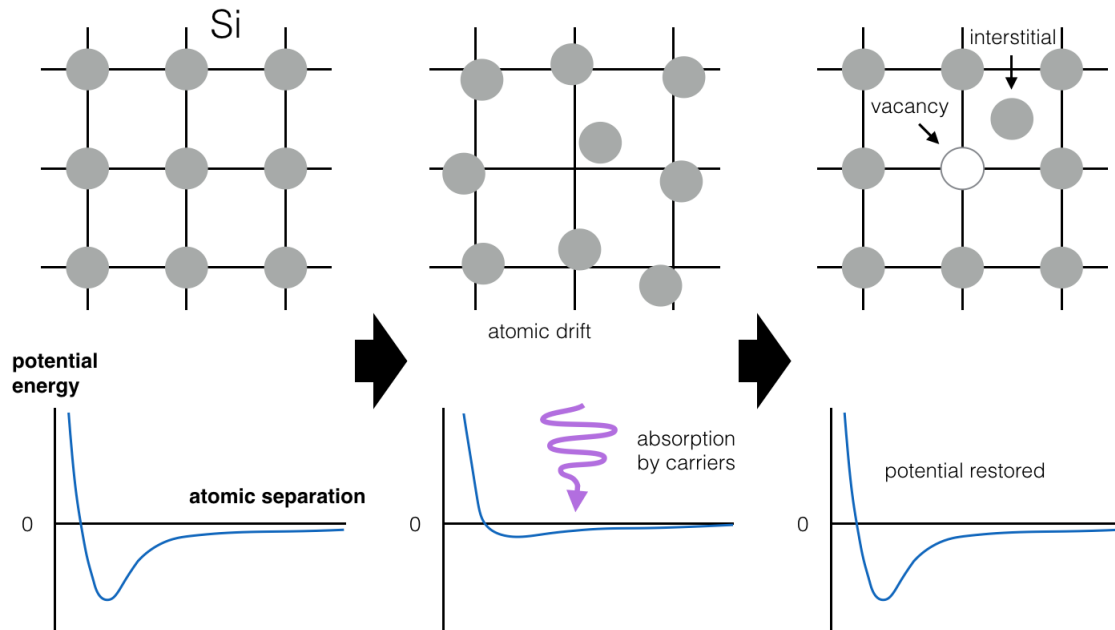


Figure 6.2: Simplified point defect generation scheme via ultrafast laser induced transient order-disorder transition of the lattice.

still at room temperature, the decrease in the attractive potential barrier causes an increase in the average interatomic spacing. As further absorption occurs, and the potential barrier effectively disappears, "free" ions may drift from its lattice site at a constant near room temperature velocity⁴. The subsequent atomic displacement may reach up to 1 angstrom in a picosecond [9, 159]. As excited carriers relax to the ground state, the interatomic potential is restored, but the material does not melt. Nevertheless, the recombination of carriers may effectively occur at interstitial sites where the noted charge density is high [4, 6]. In such case, vacancy-interstitial pair formations are probable.

Generated point defects will create local high stress states within the lattice [161], which may manifest into a variety of periodic surface nanostructures via diffusion and strain relaxation mechanisms [11, 24]. So far, such nanostructure formations are not observed for 780 nm laser irradiation on silicon. However, the accelerated linear

⁴Note that a small energy transfer to the lattice by phonon coupling, absent in the idealized two temperature model, has been shown to induce further noticeable acceleration of the ions [6].

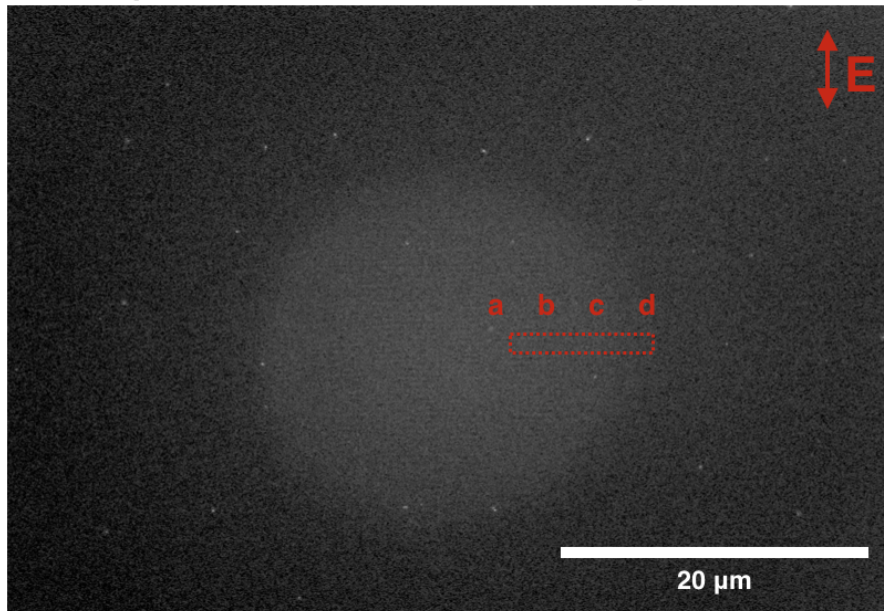
carrier excitation process at 390 nm wavelength may be suitable for an efficient point defect generation. We have indeed observed the formation of high stress state periodic surface nanostructures using 390 nm laser irradiations. The details, of which, will be presented below.

6.2 Modified Silicon Surface Morphologies in Vacuum

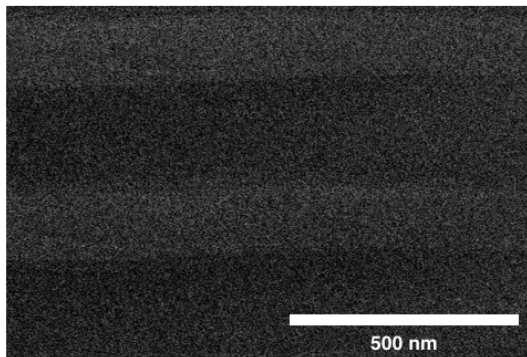
Multiple pulse irradiation of silicon is performed in a vacuum environment in order to suppress any laser induced oxidation due to elevated temperature [162]. A variety of nanostructures are observed near and below the melt threshold of silicon at 390 nm using multiple exposures. Figure 6.3 shows irradiation at a peak fluence of 52 mJ/cm² and 5000 exposures. The local fluence decreases away from the spot center and follows a Gaussian spatial intensity distribution. Close to the center of the spot at a local fluence of 50 mJ/cm² (fig. 6.3a), above the single pulse melt threshold, LSFL contrast with an average period of 360 nm is observed. This is expected considering that SPP mode is supported as the silicon optical properties would turn metallic above the melt threshold (section 4.3.1). The bright contrast also indicates that the surface undergoes amorphization post irradiation. The amorphized layer occurs due to the rapid resolidification of the laser induced melt [163]. Note that the melting of silicon would essentially disrupt any existing surface morphology, which explains why no other nanostructures beside LSFL form at this region.

At the edge of the modified surface region, at a local fluence of 37 mJ/cm² (fig. 6.3d), we observe a periodic nanostructure formation we refer to as islands. The occurrence of islands has been observed in a wide range of semiconductors using ultrafast laser irradiations [10, 11, 164]. Interestingly, such structure has also been well studied to occur in semiconductors using ion sputtering techniques [23, 165, 166]. Within the ion beam literature, the islands (or nanodots) formation has been agreed to be the result of competition between roughening due to surface curvature depen-

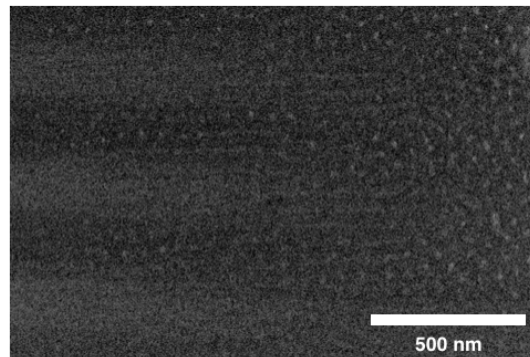
peak fluence: 52 mJ/cm² 5000 exposures



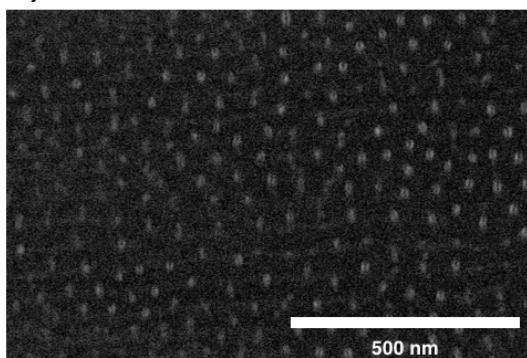
a) LSFL $F_l = 50 \text{ mJ/cm}^2$



b) HSFL $F_l = 45 \text{ mJ/cm}^2$



c) bifurcated islands $F_l = 40 \text{ mJ/cm}^2$



d) islands $F_l = 37 \text{ mJ/cm}^2$

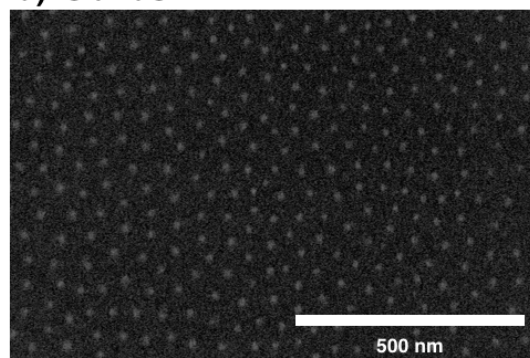


Figure 6.3: SEM images of silicon irradiated by 5000 pulses at 390 nm in vacuum showing a) LSFL b) HSFL c) bifurcated islands d) island formation near the threshold of melt. The local fluence F_l of each region (a-d) is calculated assuming a quasi-symmetrical Gaussian beam shape. The spot size of the beam is 24 μm .

dent sputtering and smoothing via surface relaxation mechanisms⁵ [165, 167, 168]. It has been pointed out, however, that an additional roughening mechanism involving point defect generation and diffusion may play a significant role within the formation kinetics of the nanodots [24]. The hypothesis stems from the discrepancy between the experimentally measured residual stress and the theoretical value involving only ion implantation formalism [24, 169]. Indeed, an experiment involving Mo seeded silicon samples concludes that additional stress state enhances the efficacy of nanodots pattern formation [170].

The concept of point defect induced stress state leading to periodic islands formation has been echoed within the laser community [10, 11]. Most recently, these island structures has been observed to evolve into HSFL via light coupling in GaAs [11]. Further bifurcation of the observed HSFL structure indicates a high stress state at the periodic surface consistent with the point defect model. Curiously, in our experiment with silicon, we observe bifurcation perpendicular to the HSFL formation (fig. 6.3c). We will discuss the bifurcation of silicon island structure further in section 6.2.2.

6.2.1 The Region of Silicon HSFL Formation

Interesting morphologies are observed at the local fluence of 45 mJ/cm^2 close to the melt threshold (fig. 6.3b). First off, we find the extent of LSFL formation we had seen previously above the fluence of melt. Due to intensity redistribution via interference and multiple irradiation pulses applied, we still see melt contrast below the conventional single pulse value [171]. However, in between the melt contrast region, the distributed fluence will drop to lower than average. Here, we observe island formation. The island formation extends through lower local fluence regions, where the LSFL is no longer apparent. Interestingly, at regions where the modulated intensity is slightly higher but not quite to the point of melt, we observe the alignment

⁵e.g. surface adatom diffusion and amorphization by ion bombardment

of the islands into HSFL. These HSFL alignments continue to be seen at a lower local fluence of 40 mJ/cm^2 (fig. 6.3c), albeit slightly less apparent.

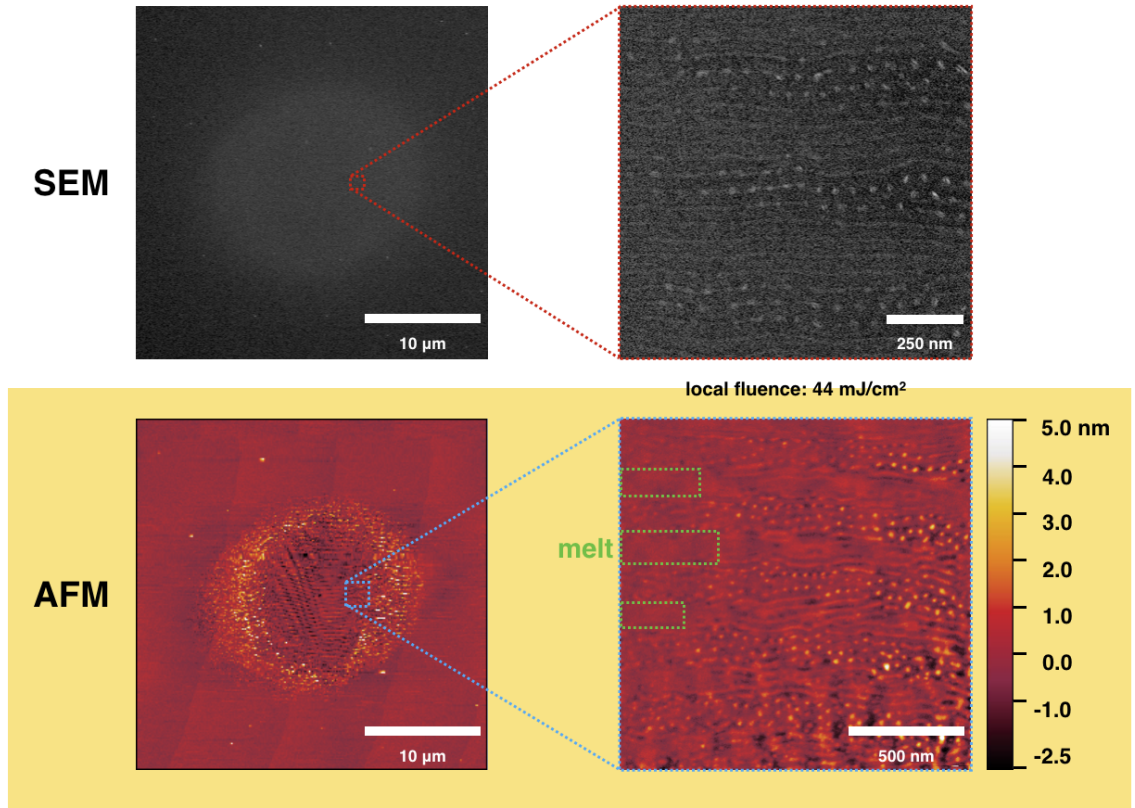


Figure 6.4: Silicon surface morphology after irradiation using $F_p = 46 \text{ mJ/cm}^2$ and 10000 exposures. The corresponding AFM height profiles map the region of HSFL and islands formation. 2D FFT image of the HSFL region is presented highlighting the HSFL and islands distribution

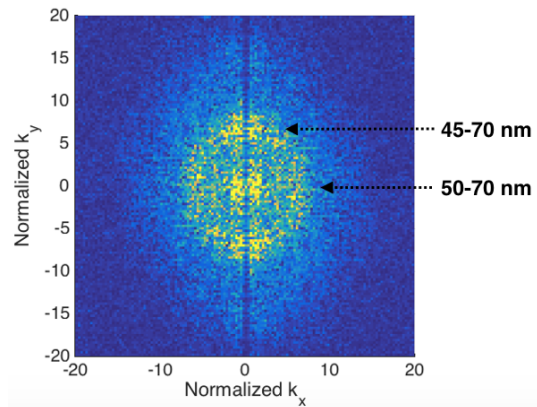


Figure 6.4 shows another instance of HSFL formation at a local fluence of 44 mJ/cm^2 and 10000 exposures. Looking at the magnified SEM and AFM profiles, a more well-defined HSFL is formed in this case. We can clearly distinguish the alternating occurrence between the islands and the HSFL, as we have previously seen

in fig. 6.3b. This is again due to a modulated intensity arriving on the surface caused by the SPP-laser interference. In this case, the intensity distribution does not quite reach the level required for melt except for the regions indicated by the green boxes, where the surface undulations diminish. Extrapolation of the predicted intensity distribution suggests that HSFL form at a slightly higher intensity than that of a pure island distribution, which is again consistent with the behavior shown in fig. 6.3.

The height profile shows that both islands and HSFL grow in the range of 1-5 nm above the perceived original surface. Darker regions in between the nanostructure formations indicate depression, which may preliminarily suggest mass redistribution process within the formation kinetics. Looking at the periodic distribution obtained via 2D FFT⁶, a fairly uniform ring with a period range of 50-70 nm describes the periodic island distribution. Interestingly, sharp peaks in the direction parallel to the HSFL wavevector indicate that the HSFL distribution is similar to the islands. This, again, shows a strong correlation between the HSFL and the islands formation (i.e. HSFL needs an existing island distribution to form). We will revisit this hypothesis in section 2.2.3, where we apply the Sipe model for inhomogeneous absorption to our analysis (section 2.2.1).

6.2.2 Island Growth and Bifurcation

At a local fluence of 37 mJ/cm², much lower than the observed fluence of HSFL formation, islands continue to grow with increasing number of exposures (fig. 6.5a to c). Surprisingly, the corresponding 2D FFT images indicate a fairly consistent period distribution throughout the growth (fig. 6.5d to f). Here, the islands form with a period range of 40-60 nm, which is similar to the period distribution shown in fig. 6.4. The fairly consistent islands period distributions across fluences and number of exposures may suggest that an additional non-electromagnetically driven mech-

⁶ k_x and k_y axes are normalized to $2\pi/\lambda = 1$, where $\lambda = 390$ nm.

anism is responsible for the periodic characteristics of the islands. As the islands continue grow in size and intensity, we begin to observe bifurcations at the island peaks(fig. 6.5b and c). At 10000 exposures, The bifurcations are accompanied by a preferential alignment of the islands parallel to the polarization of the beam.

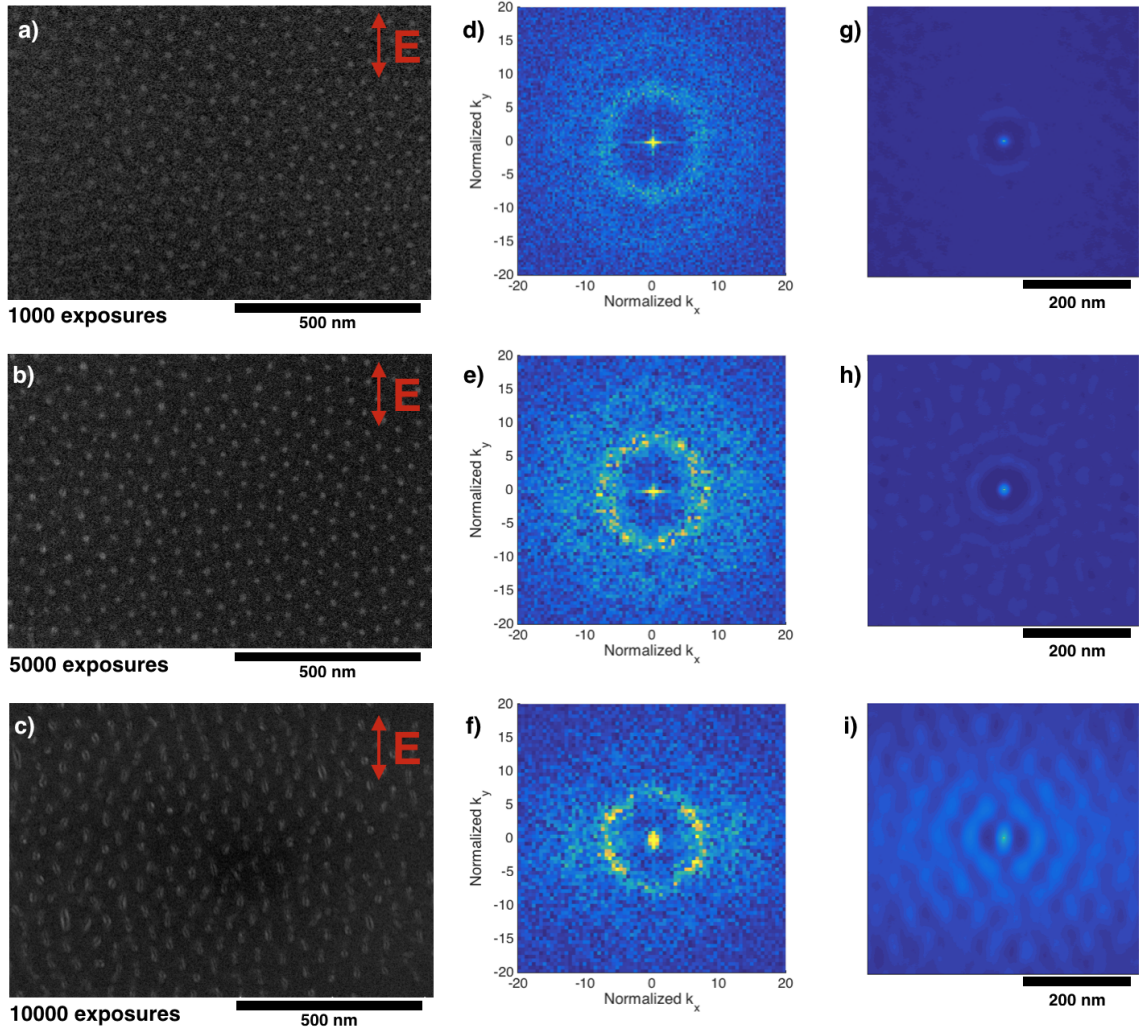


Figure 6.5: The formation of islands using a) 1000 b) 5000 c) 10000 exposures at local fluence = 37 mJ/cm^2 . The corresponding 2D FFT (d,e,f) and autocorrelation (g,h,i) of the images are presented. As the islands grow, their distribution becomes more hexagonally aligned.

Further analysis via autocorrelation reveals that the arrangement of the islands are initially random at 1000 exposures (fig. 6.5g). However, upon additional exposures, we begin to observe a shift toward a quasi-hexagonal islands distribution (fig. 6.5h

and i). Similar nanodot formation on silicon has been observed by Gago et al. using Ar^+ ion beam irradiation, in which a hexagonal arrangement of the nanostructures is reported [23]. Moreover, the periods of the silicon nanodots are also reported to saturate at around 52-60 nm for a 6 min or longer irradiation. This, again, matches remarkably with the island formation in our study. Note that in [23], no nanodot bifurcation is observed despite the similar sized nanostructure formed. We would argue that in the case of energetic ion beam irradiation, the accumulated stress at the surface can be relieved via induced collateral damage. Case in point, surface amorphization is observed in [23] via cross-sectional TEM. Note that, in the case of laser induced island formation in GaAs, no significant surface amorphization is observed [11]. Instead, stress is reported to accumulate at the surfaces of the formed periodic structures, which later induces bifurcation. From our observation of islands bifurcation, we then hypothesize that the lattice arrangement of the formed islands on silicon would remain crystalline. We argue that strain relaxation on silicon occurs at a much earlier stage compared to GaAs.

Figure 6.6 shows the extent of the island growth and bifurcation at 100000 exposures. Further alignment and mass accumulation of the islands parallel to the laser polarization is observed⁷. Within our initial prediction, a polarization dependent field enhancement along the polarization axis may have caused an inhomogeneous energy absorption leading to the anisotropic growth. This will be discussed further in section 6.3. FFT analysis shows a broadening of the islands period distribution and an increase in the upper limit of the distribution to about 120 nm, which also directly correlates to a broadening of the size distribution. These patterns may indicate a competition for growth between the islands. The corresponding AFM image shows a

⁷A low spatial frequency periodic intensity modulation related to the LSFL mechanism can be seen in the image. In this case, the central part of the irradiated region experiences surface modifications and material removal (not shown) due to the high number of exposures leading to incubation and damage accumulations effects [171, 172]. The subsequent field enhancement may have caused SPP to be excited at a much lower fluence.

bifurcated islands growth up to 10 nm with a trench depth of about 2-3 nm. The bifurcation occurs along the long axis of the mature island, which is consistent with our initial prediction of stress accumulation and subsequent strain relaxation. The strain relaxation mechanism has been suggested to be vacancy and interstitial diffusion [11]. This will be a subject for further studies.

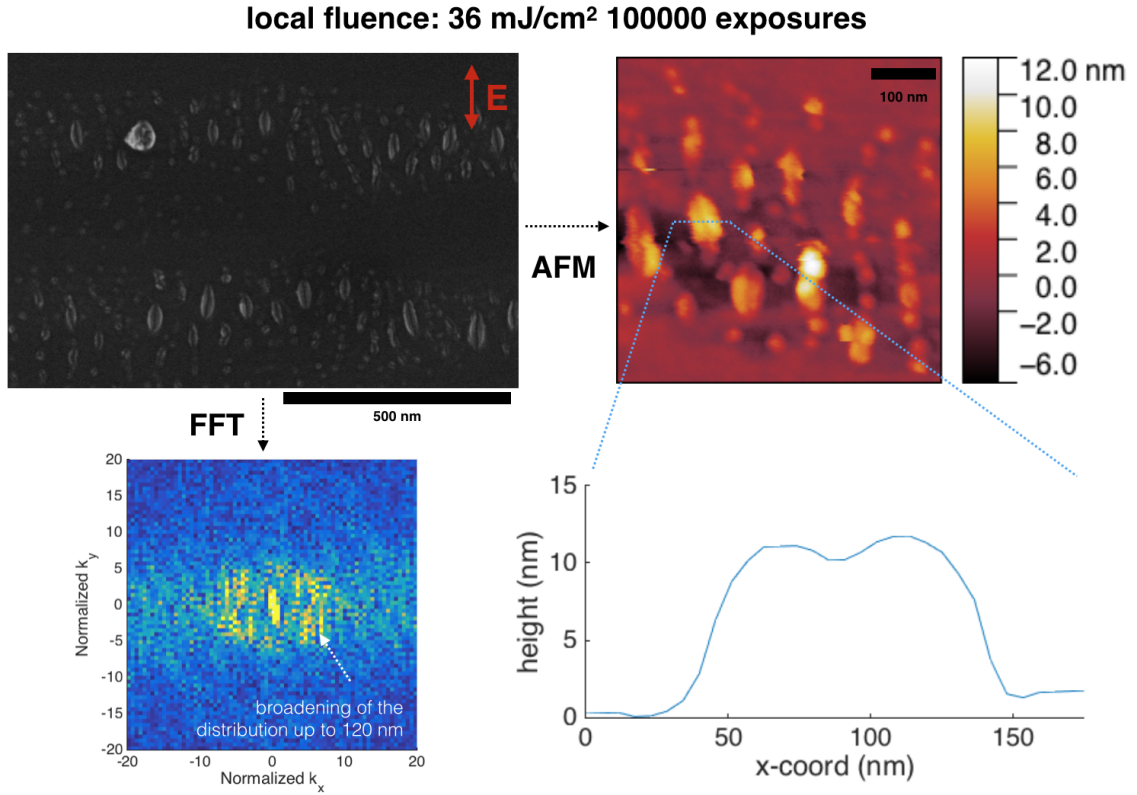


Figure 6.6: SEM (top left) and AFM (top right) images of fully formed bifurcated islands at $F_l = 36 \text{ mJ/cm}^2$ and 100000 exposures. FFT analysis (bottom left) on the SEM image shows a broadening of the island distribution up to 120 nm. The AFM trace of a bifurcated island (bottom right) shows an island height in the order of 10 nm with a trench depth of about 2-3 nm.

6.2.3 The Influence of Silicon Native Oxide

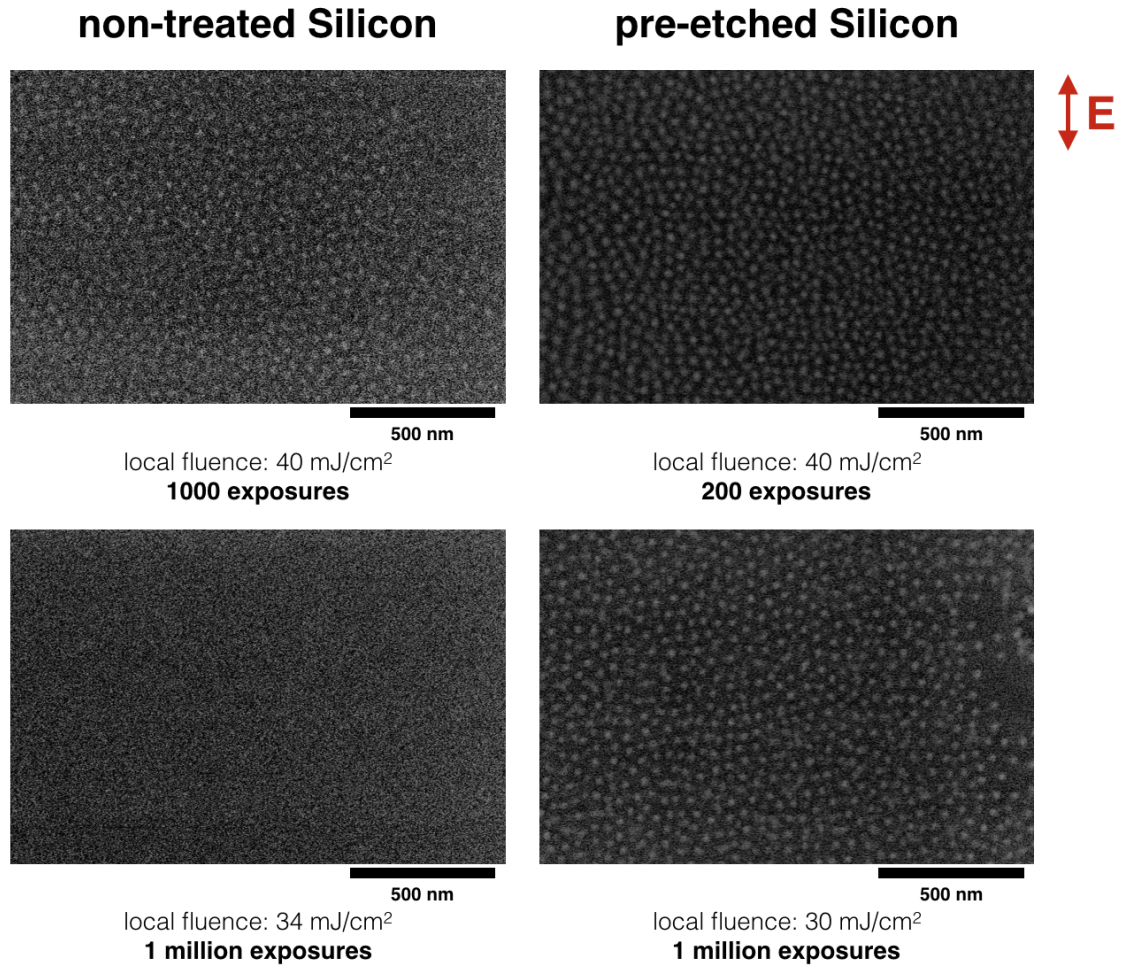


Figure 6.7: The effect of native oxide etching on silicon island formation in vacuum. In general, island formation occurs at lower fluences and number of shots for a pre-etched silicon.

Following our point defect based hypothesis, an existing native oxide layer on silicon may obstruct interstitial diffusion process to the surface. Hence, we examine the implication by eliminating the native oxide layer pre-irradiation via chemical etching process, as outlined in section 3.5.3. The subsequent irradiations were done in vacuum to prevent any re-formation of oxide layer as well as further laser induced oxidation (see section 3.6). Figure 6.7 compares the formation of islands between pre-etched and non-treated samples after irradiation. At a local fluence of 40 mJ/cm², islands

appear on the pre-etched samples after 200 exposures. No islands were observed at 100 exposures or lower at the same local fluence. The islands continue to be observed at a much lower local fluence of 30 mJ/cm² using 1 million exposures.

For the non-treated samples, island formation are shown to require a higher fluence and/or number of exposures in general. Now, at a local fluence of 40 mJ/cm², the minimum number of exposures for island formation is between 500 to 1000. While at 1 million exposures, islands are not observed at a higher local fluence of 34 mJ/cm² compared to the pre-etched samples. These observed patterns clearly suggest that the silicon native oxide layer negatively affects the formation of the islands. Considering that silicon self-interstitial diffusivity in SiO₂ (with activation energy $E_a \sim 5.34$ eV [173]) is lower than in single crystal silicon ($E_a \sim 1.86 - 4.3$ eV [174]), we argue that point defect diffusion to the surface is being inhibited by the native oxide layer. This is, again, consistent with the hypothesis of point defect generation and diffusion being responsible for the island formation.

6.3 HSFL Formation Mechanism: Sipe Model Interpretation

In the prior sections, we have observed a direct correlation between islands and HSFL formation; they have been shown to form in an alternating manner as well as having very similar periodic distribution. The question remains of whether HSFL forms under the same point defect principle we have proposed throughout this chapter. And, if so, through what process does the preferential alignment of islands into HSFL occur. As HSFL structure forms under multiple pulse irradiation, the effect of intra-pulse feedback has to be taken into account [175]. Particularly, considering the fairly large number of pulses applied in our experiment (in the order of 1000), the formed HSFL, by correlation, has to sustain or reinforce its surface features between incident laser pulses. In other words, HSFL formation mechanism is likely to have a steady state characteristic.

As islands growth yields prominent surface roughness, incident light scattering with the features may yield inhomogeneous energy absorption [25]. According to the Sipe theory (section 2.2.1), the inhomogeneous intensity distribution $I(\vec{k})$ would be proportional to the amplitude of surface roughness $|b(\vec{k})|$ and the efficacy factor $\eta(\vec{k}; \vec{k}_x)$ (eq. (2.3)). As such, considering the characteristic spatial distribution of the islands, there will be a tendency for energy to be distributed at wavevectors where the intensity of the islands distribution is high. The enhancement in energy absorption will then, in principle, generate more point defects through carrier excitations.

The efficacy factor $\eta(\vec{k}; \vec{k}_x)$, which describes the degree of absorption at a particular frequency coordinate below the surface, depends on several factors: the complex material permittivity ϵ , the filling factor F and the shape factor s . The later two factors simulate surface roughness via the selvedge region formalism (see fig. 2.2). The filling factor denotes the fraction of surface filled with "islands", while the shape factor is defined by $s = l_t/l_s$, where l_t is the average size or correlation distance of islands and l_s is selvedge layer depth [57]. Assuming our island structure has an average height of 3 nm, an average diameter of 18 nm, and an average period of 50 nm when the HSFL alignment starts to occur (fig. 6.4), we determine F and s to be 0.11 and 6, respectively⁸.

In contrast to the near-infrared regime, the change in the dielectric response of silicon at 390 nm will no longer be adequately described by the Drude model due to near-resonance dispersion behavior [176]. For the sake of simplicity, we will assume that the imaginary part of the permittivity remains constant in our calculation, thereby not accounting for the change in optical losses. As such, the dynamics of the efficacy factor will be presented qualitatively through changing real part of the complex permittivity of the material $Re[\epsilon]$. The intrinsic permittivity of silicon at

⁸The calculated s value is much larger than 0.4 used in [57] due to the tall island formation compared to average semiconductor wafer roughness. In our case, we assume that the selvedge region includes the entire height of the protruding islands.

390 nm used in our calculation is $35.064 + 6.674i$ [116].

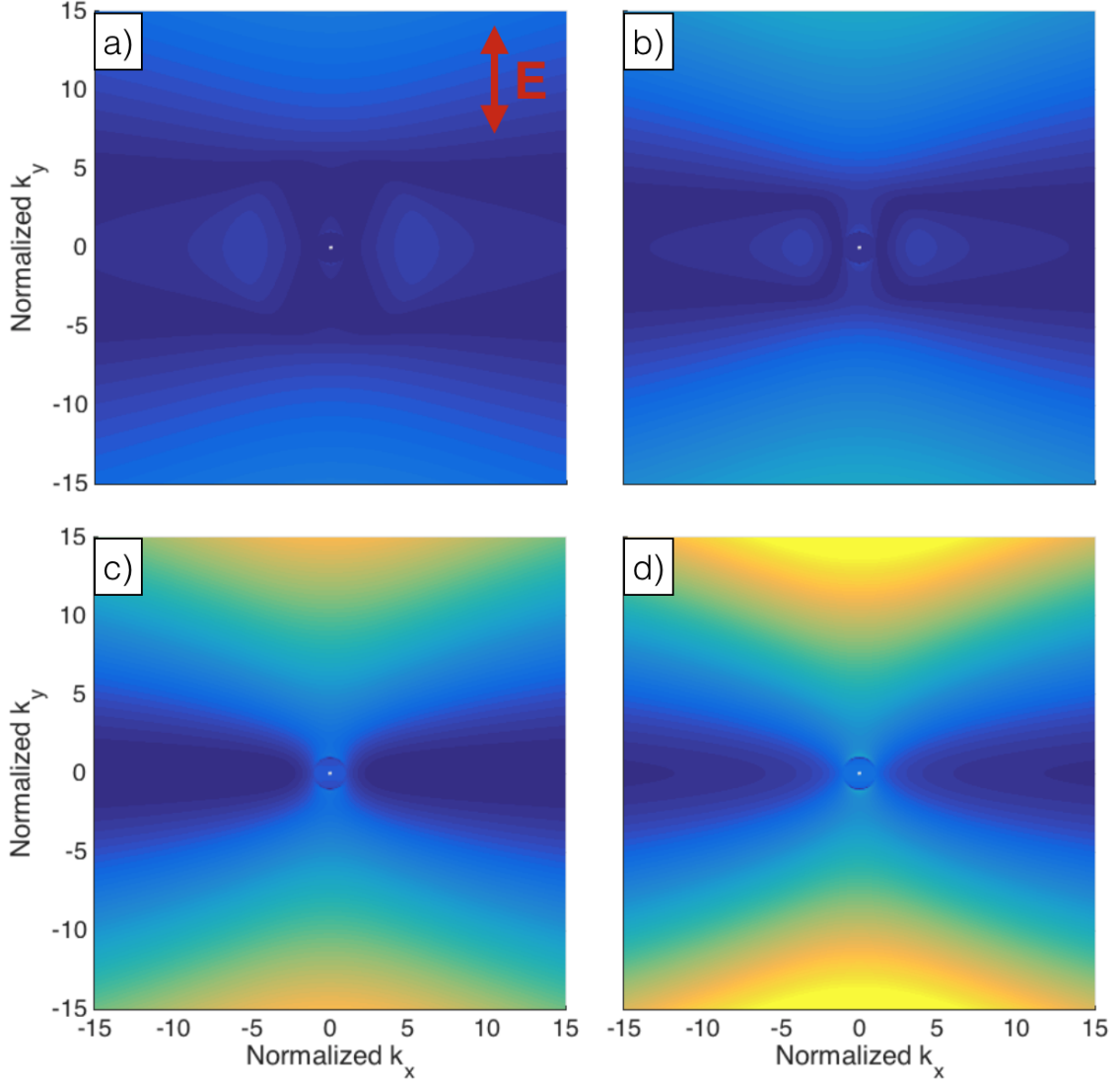


Figure 6.8: Efficacy factor maps of silicon at 390 nm using $F = 0.11$ and $s = 6$ for $Re[\epsilon] =$ a) 35.064 b) 15 c) 2 d) -5. $Im[\epsilon] = 6.674$ is assumed to be constant. Blue-yellow color transition represents increasing values. The wavevector coordinates are normalized to $2\pi/\lambda$.

Figure 6.8 shows the efficacy maps $\eta(\vec{k}; \vec{k}_x)$ calculated at $k_x = 0$ (normal incidence) using p-polarized incident fields. A complete derivation of the efficacy factor is presented in appendix E. In general, $\eta(\vec{k}; \vec{k}_x)$ shows components parallel and perpendicular to the polarization with comparable intensities at intrinsic permittivity

value (fig. 6.8a). As the permittivity drops to represent a more conductive behavior, significant enhancement of components perpendicular to the polarization can be observed, while parallel features effectively vanish (fig. 6.8c and d). Notice the increase in amplitude at frequency component near unity perpendicular to the polarization as $Re[\epsilon]$ becomes negative (fig. 6.8d). This enhancement accounts for SPP mode coupling [25], which may subsequently yield LSFL (fig. 4.2).

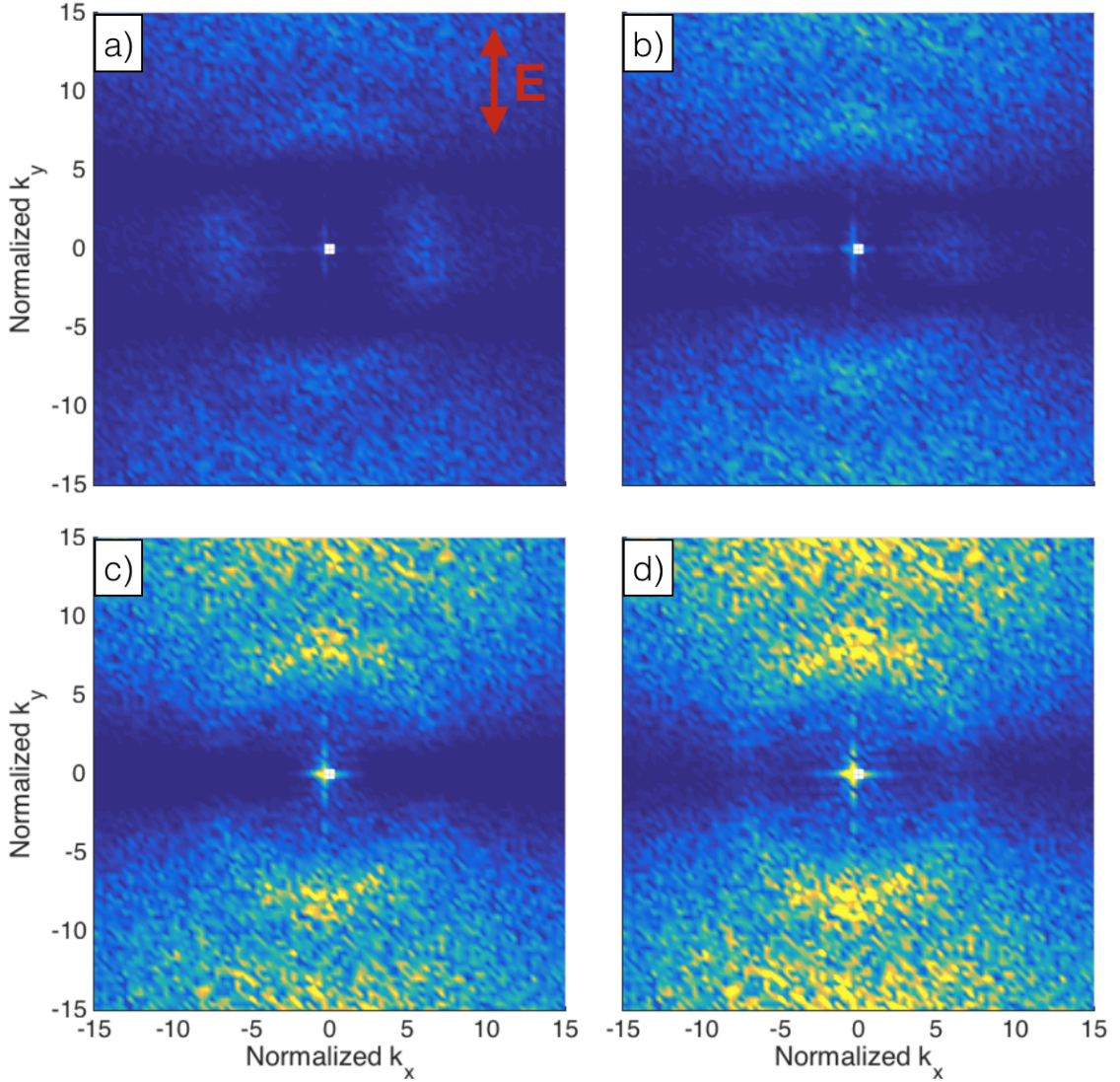


Figure 6.9: Maps showing the products of $\eta(\vec{k}; \vec{k}_x)$ and $|b(\vec{k})|$ indicating Inhomogeneous intensity distribution for $Re[\epsilon] =$ a) 35.064 b) 15 c) 2 d) -5. Blue-yellow color transition represents increasing values.

Following eq. (2.3), the inhomogeneous intensity distributions $I(\vec{k})$ due to islands scattering using p-polarized laser irradiations are calculated and shown in fig. 6.9. The islands periodic distribution $|b(\vec{k})|$ used in the calculations follows fig. 6.5e (with local fluence = 37 mJ/cm² and 5000 exposures). At low carrier excitation, the $I(\vec{k})$ maps reveal absorption at wavevector components perpendicular and parallel to the polarization (fig. 6.9a and b), mirroring the efficacy factor shown in fig. 6.8a and b. The features indicate a slight anisotropic growth of the islands with periods resembling the initial pre-irradiation distribution. The observed distinct peaks parallel to the polarization implies periodic alignment in the same direction, which resembles the alignment of bifurcated islands shown in fig. 6.5e. Meanwhile, frequency components perpendicular to the polarization does not quite show any strong discernible peaks, which implies a rather uniform absorption enhancement along the direction, promoting further island growth.

As the permittivity reaches near critical value ($Re[\epsilon] = 0$), we observe massive enhancement of $I(\vec{k})$ perpendicular to the polarization (fig. 6.9c and d). Concurrently, peaks parallel to the polarization disappears, signifying the termination of parallel islands alignment. Strong distinct peaks perpendicular to the polarization with periods of 40-60 nm can be clearly observed, which matches with the HSFL period distribution shown in fig. 6.4. This is a clear indication of the preferential alignment of islands into HSFL via anisotropic inhomogeneous energy absorption. Notice that fig. 6.9d still shows peaks at $k_y \sim 1$. The peaks indicate intensity modulation with period equaling the SPP wavelength, consistent with our observation.

CHAPTER VII

Summary and Future Work

Femtosecond laser irradiation of semiconductors yields a large variety of surface structures with characteristic periods close to and/or much smaller than the laser wavelength. The formation mechanisms of such periodic structures rely heavily on the interactions between the intense laser field and the concurrent dynamically changing material's carrier and lattice properties. The theory of LSFL formation on silicon based on the probability of SPP excitation within the pulse duration is examined. A simulated carrier behavior on a silicon surface shows a fairly good agreement with experimentally observed material parameters. A more accurate silicon carrier dynamics, however, requires additional work, especially via sub-femtosecond time-resolved studies. Nevertheless, the observed LSFL characteristics in our study suggest that the occurrence of SPP-laser interference is probable. For instance, the LSFL period slightly below the laser wavelength formed using a normal incidence irradiation correlates strongly with the SPP wavelength. In addition, SPP-laser interference based calculations predict the corresponding LSFL wavelengths at varying incidence angles fairly accurately.

The formed LSFL period has been demonstrated to depend on the transient optical properties of the silicon surface, which depends, for the most part, on the free carrier response due to a large excited carrier density. Field enhancements due to the presence

of a strong plasmonic material such as gold increases the amount of laser energy absorbed. This results in an increase in the formed LSFL amplitude and wavelength on an irradiated silicon substrate alongside a gold step edge structure. The effect becomes more apparent when the gold step edge's surface area is large. In addition, a phase matching condition affected by the geometry of the gold step edge is established, which causes a variation in the coupled SPP intensity on the gold surface. Consistent with the SPP-laser interference theory, LSFL wavelength is shown to increase with fluence when the laser polarization is perpendicular to the step-edge. This, however, is not apparent in the case of laser polarization parallel to the step-edge. Instead, we observe a correlation between a possible near field diffraction modulated intensity and the corresponding LSFL characteristics. Finally, the formation of nanojets on thin gold film is observed and is suggested to be result of multiple SPP sources interference with the laser.

A novel HSFL formation on silicon is observed using a low repetition rate laser at 390 nm wavelength. The structure forms after a high number of exposures at fluences below the melt threshold. The HSFL formation is accompanied by the occurrence of periodic island-like nanostructures, which is linked to the generation and diffusion of point defects due to a laser induced lattice instability. In addition, observations of bifurcated islands suggest a strain relaxation process, which implies a crystalline island structure. This is further supported by the observation of a quasi-hexagonal alignment of the islands. A steady state calculation based on light scattering in the near field is applied to model the periodic alignment of islands into HSFL. At an excited material state, the anisotropic alignment of the islands into HSFL are shown to be probable. The formation of periodic nanostructures on silicon yields wide technological interests, especially considering the possibility of the surface features being crystalline. Nevertheless, additional work has to be done to in order to determine the actual crystal structure of the modified surface. This topic, as well as other future

work related to the thesis will be discussed in the following sections.

7.1 Structural Characterization of HSFL Formation on Silicon

As discussed in chapter VI, a high stress state due to point defect generation and diffusion has been suggested to be responsible for the formation periodic islands on silicon. This argument is supported by a similar observation of islands and a subsequent HSFL formation in GaAs [11]. Figure 7.1 shows the cross-section of an HSFL formed on GaAs, of which the structure is shown to grow above the original surface. The resulting bright-field contrast and electron diffraction pattern indicate a strained nanocrystalline arrangement of the HSFL crystal structure. The above surface structure is also reported to be epitaxial with the bulk (not shown). In addition, bifurcation of the GaAs HSFL is observed, which is very likely due to a strain relaxation mechanism.

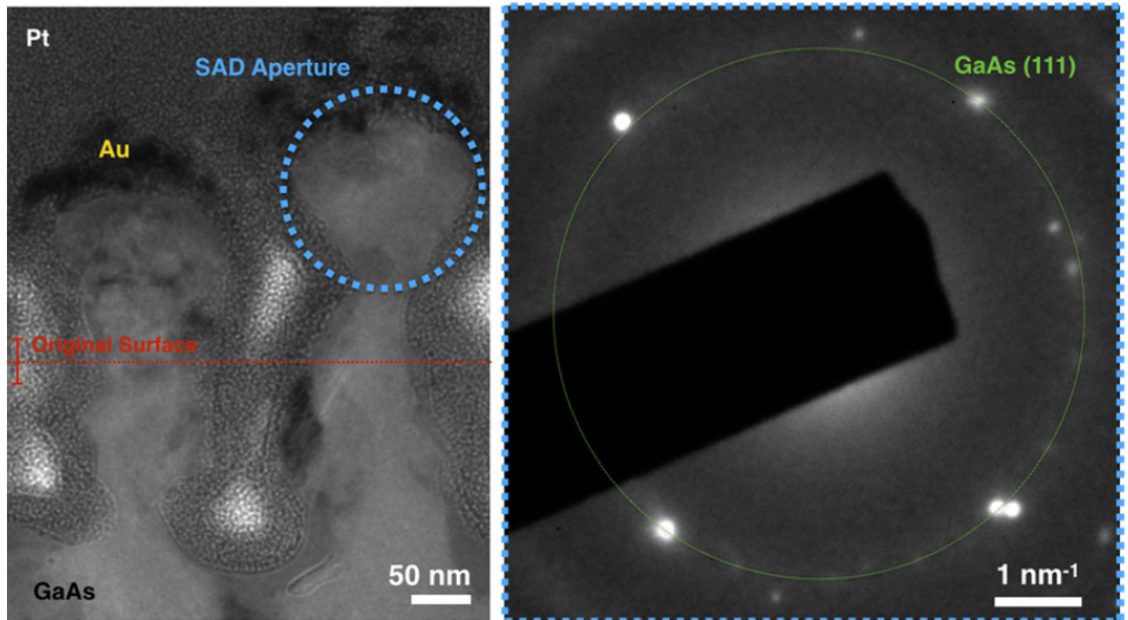


Figure 7.1: Bright-field TEM (left) and selective area electron diffraction pattern (right) of a GaAs HSFL cross-section. Adapted from [11].

In silicon, we have observed similar island and HSFL formation characteristics to the GaAs HSFL formation in [11], namely below melt threshold formation, island growth above the original surface, and nanostructure bifurcation. To a first approximation then, we would expect the silicon islands and HSFL to have a crystalline structure. Cross-sectional analysis via high-resolution TEM and selective area electron diffraction is crucial in determining the crystal structure of the silicon islands and HSFL. In addition, an observation of a high density silicon vacancy and interstitial within these structures may further confirm the general hypothesis of laser-induced point-defect generation. For instance, injection of silicon interstitials by ion implantation has been well-studied to form a cluster along the $\{311\}$ plane [177]. We would expect that the same $\{311\}$ defects formation would occur at a high silicon interstitial density generated by a laser irradiation.

7.2 Laser Induced Oxidation

Multi-pulse laser irradiation at 390 nm below the melt threshold (41 mJ/cm^2) shows the formation of protruding surface structure reaching up to $5 \mu\text{m}$ in height using 1 million exposures (fig. 7.2c and d). A subsequent energy dispersive spectroscopy (EDS) mapping indicates that the structure consists of a Si-O type chemistry (fig. 7.2c and d), which is likely to be nonstoichiometric [178]. Laser induced oxidation on silicon has been mainly explained as a thermally accelerated process [162]. The conventional oxidation kinetics involve the diffusion of oxygen ions into the silicon-oxide interface followed by a subsequent reaction of the ions with the silicon substrate [179]. An accelerated kinetics below melt temperature induced by a nanosecond laser heating has indeed been shown to yield a rapid rate of silicon oxidation [178]. However, no femtosecond laser induced silicon oxidation at the scale of our observed structure has been reported in the literature.

peak fluence: 41 mJ/cm² 1 million exposures

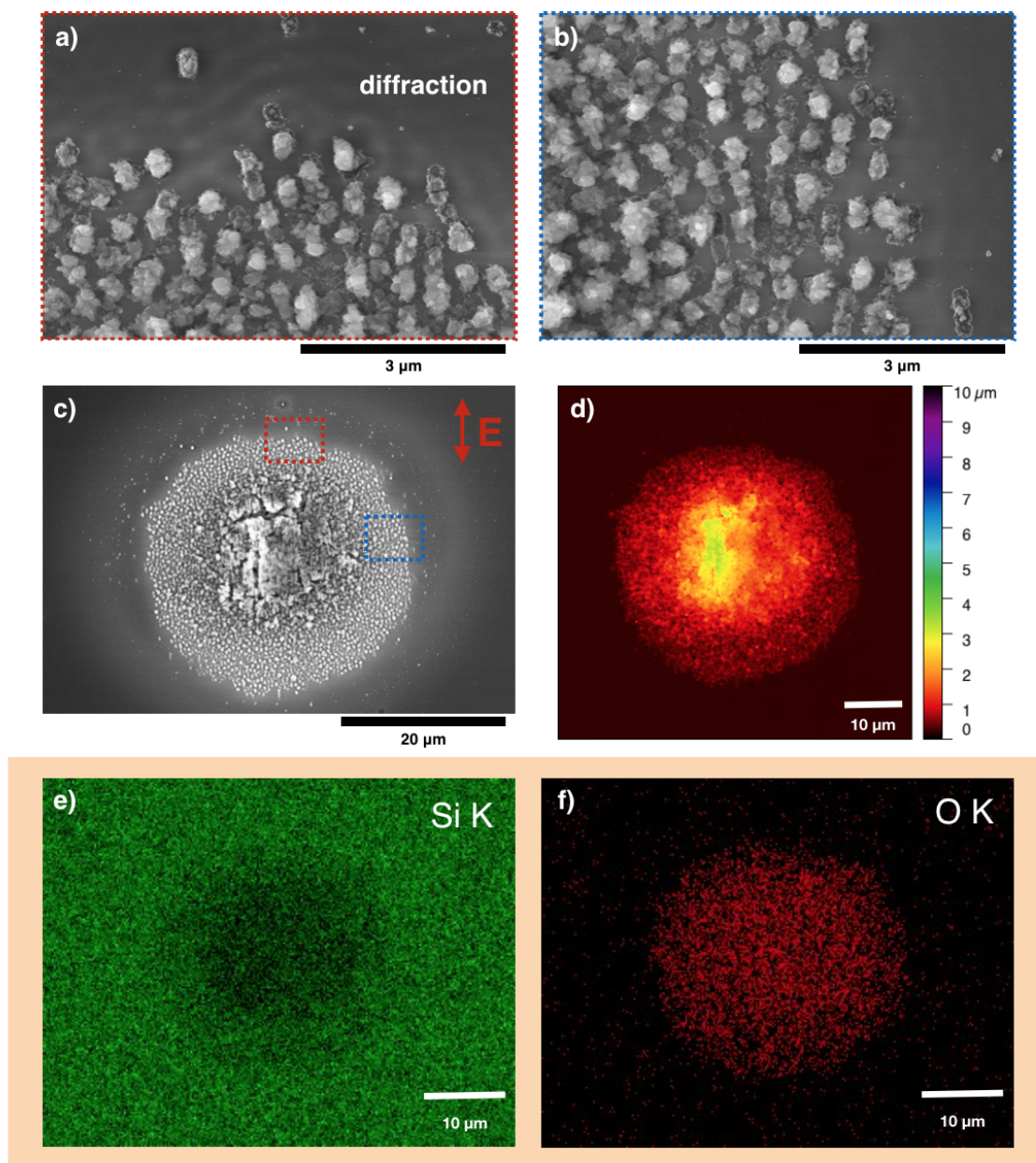


Figure 7.2: Tall oxide formation by irradiation in air below the melt threshold. Periodic localized arrangement of the oxide growth is observed in the SEM images (a-c). Confocal microscopy indicates oxide growth reaching up to 5 μm in height (d). Subsequent EDS mapping shows silicon and oxygen traces on the structure (e-f).

Besides the large oxidation volume observed, fig. 7.2 also shows periodic arrangement of the oxide formation in the order of the laser wavelength. Further examination of fig. 7.2a and b indicates that a diffraction modulated intensity may be generated

by an incident laser scattering with the tall oxide features. Although the localized growth patterns shown in fig. 7.2a and b are seemingly a direct result of the intensity modulation at the surface, we are still seeing clusters instead of a smoothly varying oxide growth. This indicates that additional processes might be involved within the oxide growth kinetics. For instance, it is possible that silicon interstitial diffusion to the surface may have enhanced the reaction rate of the oxidation process.

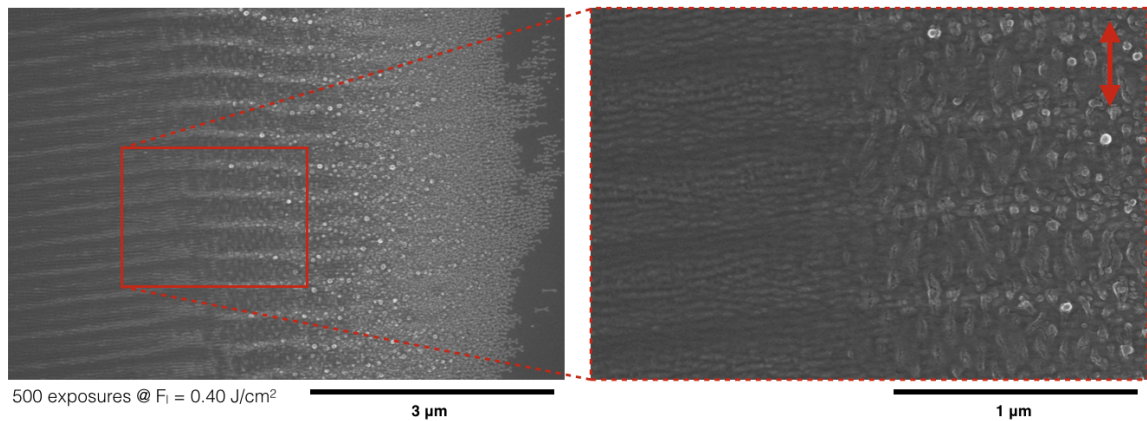


Figure 7.3: The formation of islands and HSFL using 390 nm wavelength in air at a local fluence of 0.40 J/cm^2 . A similar nanostructure formation compared to the irradiation in vacuum is observed with the addition of a possible surface oxide layer formation.

At a much lower number of exposures, we observe HSFL and island formation on silicon in air (fig. 7.3). The formed nanostructures, however, are not as distinct as in the case of a vacuum irradiation. Considering the degree of oxidation occurring at 1 million exposures we have observed prior, it is very likely that an oxide layer form on top of the HSFL and the islands. The laser induced oxide layer may obscure our observation of the island and HSFL formation dynamics. More work need to be done in order to determine the structural composition of the nanostructures formed in air through TEM and chemical characterization methods such as EDS and X-ray photoelectron spectroscopy (XPS). This is important considering the intricate technological challenges surrounding laser irradiation in vacuum.

7.3 HSFL Formation in Wide Band Gap Semiconductors: The Role of Coulomb Explosion

Since SiC has a large band gap (~ 3.23 eV for 4H-SiC) compared to the photon energy at 780 nm laser wavelength, multiphoton absorption is essential for carrier excitation. To a first approximation, the highly nonlinear nature of the carrier excitation in SiC may induce an abrupt increase in the carrier density and may lead to an electrostatic type carrier-lattice interactions such as the coulomb explosion. This is consistent with our observation of the absence of SiC melting in the case of single pulse femtosecond laser irradiation. Alas, the ultrafast laser induced carrier dynamics in SiC still require more studies in order to verify this phenomenon.

A shift from the previously hypothesized HSFL formation mechanism is observed on SiC. As shown in fig. 7.4, HSFL form on random localized regions with no accompanying island nanostructure. In addition, material removal is evident from looking at the subsurface features and the amount of surrounding debris generated. This is interesting considering that the single pulse ablation threshold is at a much higher value of 0.78 ± 0.05 J/cm². The large decrease in the material removal threshold has been attributed to the increase in the multi-pulse laser absorption by structural defects such as color centers and stacking faults [14, 180]. This partly explains the localized nature of the HSFL formation in fig. 7.4. In addition, Coulomb explosion has been suggested to be the mechanism of femtosecond laser induced material removal at low fluence in SiC due to a lack of thermal characteristics in the ablated nanoparticles [14, 181]. Meanwhile, nanoablation induced by Mie scattering has been argued to be the HSFL formation mechanism [79].

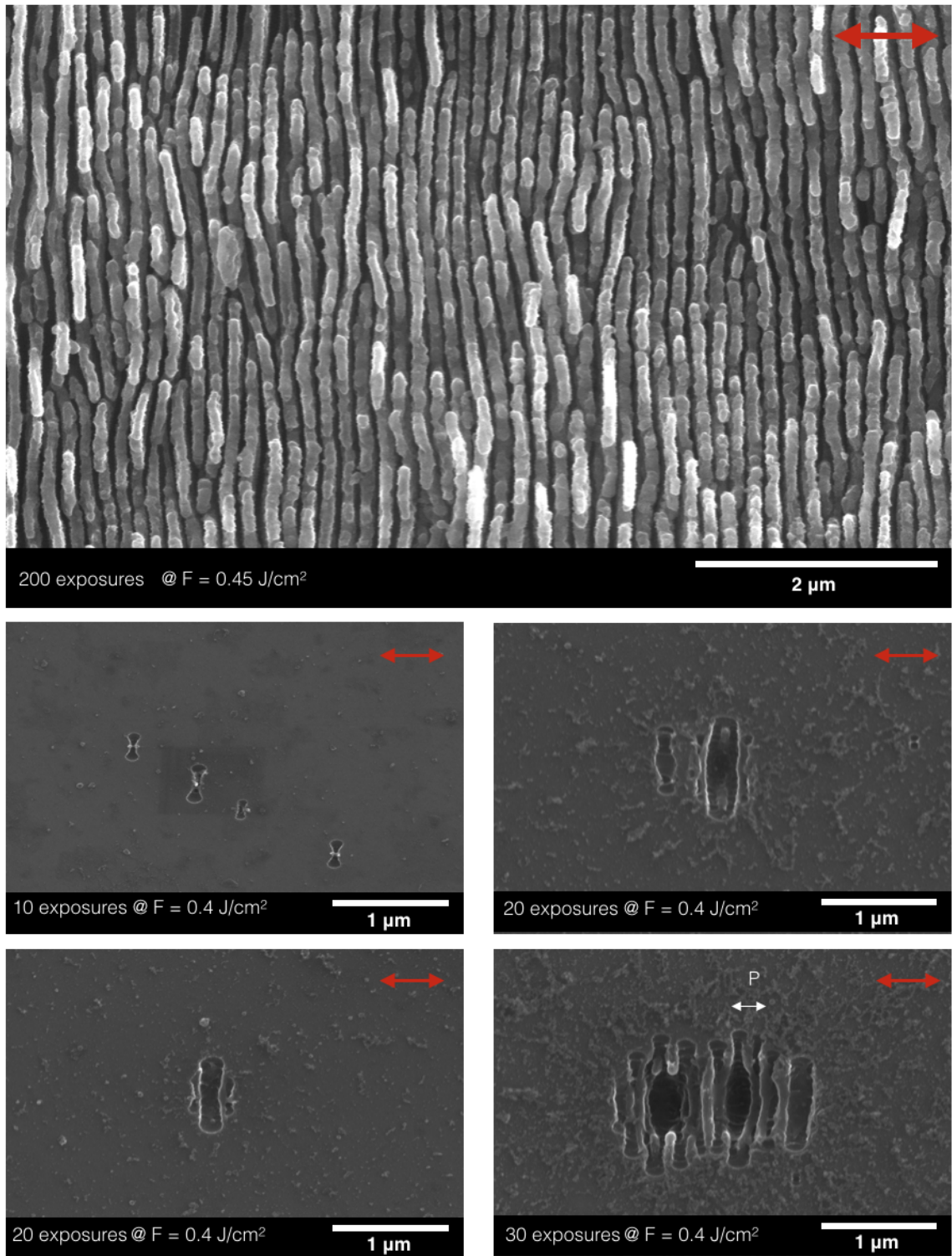


Figure 7.4: HSFL formation in SiC using multiple pulse irradiations at 780 nm wavelength showing a fully formed structure (top panel) and localized growth (bottom panels) at fluences much lower than the single pulse ablation threshold. The HSFL period $P \sim 200 \text{ nm}$.

An interesting shift in the single pulse irradiation morphology is observed at 390 nm wavelength. Figure 7.5a shows a decrease in the ablation threshold at 390 nm compared to 780 nm laser irradiation. More importantly, however, an indication of melting is observed at 390 nm (fig. 7.5b), in which the change in optical contrast suggests a phase transformation. This might be due to a change in the dominant carrier excitation mechanism. Mainly, since the photon energy is now close to the SiC band gap energy, linear absorption mechanism is probable. Additional irradiation study using 260 nm wavelength (frequency tripled) may be necessary to further observe the effect of linear absorption on the structural modification of SiC. In summary, material removal in SiC below the single pulse ablation threshold is likely to be electronically induced. Hence, we suggest that coulomb explosion drives the HSFL formation in SiC instead of a point defect accumulation mechanism such as in the case of low band gap semiconductors.

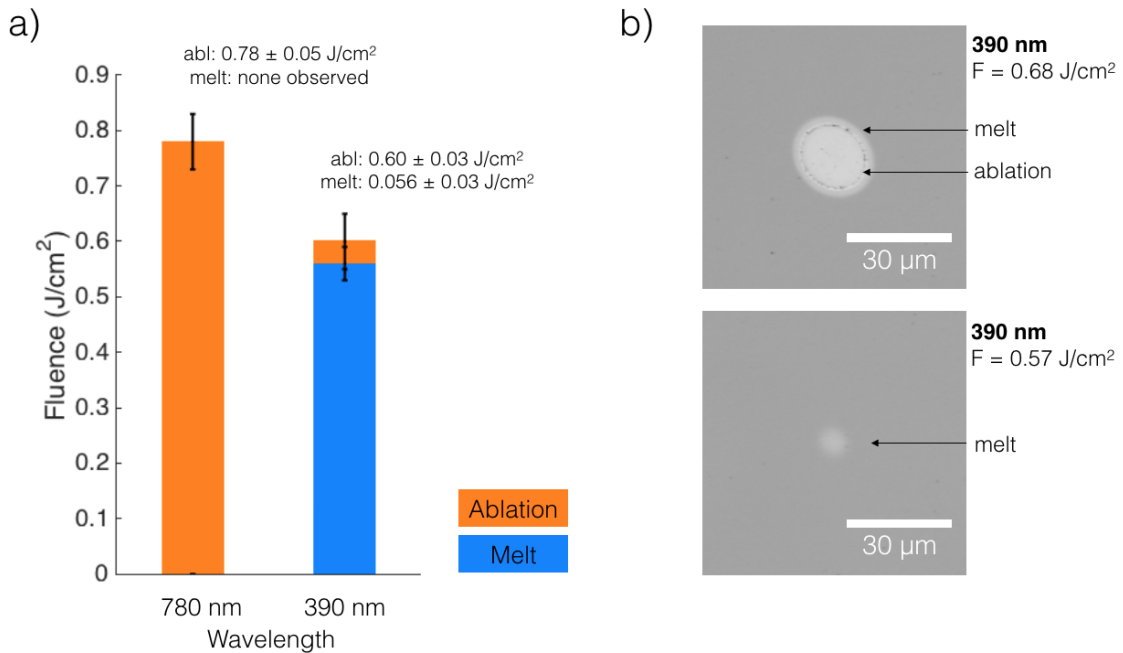


Figure 7.5: a) Ablation and melt thresholds of SiC at 390 nm and 780 nm wavelengths. No melt threshold is observed in the case of 780 nm irradiation. b) Distinct melt and ablation contrasts are shown for 390 nm irradiation.

APPENDICES

APPENDIX A

Derivation of the Electric Field for Surface TM Wave Propagation

Starting with Ampere's law:

$$\nabla \times \vec{H} = \frac{\partial \vec{D}}{\partial t} + \vec{J} \quad (\text{A.1})$$

where \vec{H} = magnetic field strength, \vec{D} = electric displacement, and \vec{J} = current density. Since we are dealing with an oscillating field source, we can treat \vec{J} as $\frac{\partial \vec{P}}{\partial t}$, where \vec{P} denotes the polarization density. Assuming a linear response, $\vec{P} = \epsilon_0 \chi \vec{E}$, where ϵ_0 = vacuum permittivity and χ = electric susceptibility. Hence:

$$\nabla \times \vec{H} = \epsilon_i \frac{\partial \vec{E}}{\partial t} \quad (\text{A.2})$$

where ϵ_i is the permittivity of medium i , which equals to $\epsilon_0(1 + \chi_i)$. Assuming a time harmonic field source, the electric field can be written as:

$$\vec{E} = E_0 e^{-i\omega t} \quad (\text{A.3})$$

Hence,

$$\frac{\partial \vec{E}}{\partial t} = -i\omega \vec{E} \quad (\text{A.4})$$

The left hand side of eq. (A.1) follows:

$$\nabla \times \vec{H} = \left(\frac{\partial H_z}{\partial y} - \frac{\partial H_y}{\partial z} \right) \hat{x} + \left(\frac{\partial H_x}{\partial z} - \frac{\partial H_z}{\partial x} \right) \hat{y} + \left(\frac{\partial H_y}{\partial x} - \frac{\partial H_x}{\partial y} \right) \hat{z} \quad (\text{A.5})$$

From eq. (A.5), eqs. (2.7a) and (2.7b) yield:

$$\nabla \times \vec{H}_{SPP}^{(1)}(x, y, t) = A(k_{SPP,y}^{(1)}, -ik_{SPP,x}, 0) e^{i(k_{SPP,x}x + k_{SPP,y}^{(1)}y - \omega t)} \quad (\text{A.6a})$$

$$\nabla \times \vec{H}_{SPP}^{(2)}(x, y, t) = B(-ik_{SPP,y}^{(2)}, -ik_{SPP,x}, 0) e^{i(k_{SPP,x}x - k_{SPP,y}^{(2)}y - \omega t)} \quad (\text{A.6b})$$

Finally, combining eqs. (A.2) and (A.3) with eqs. (A.6a) and (A.6b) generate the expressions below for TM propagating fields in medium (1) and (2):

$$\vec{E}_{SPP}^{(1)}(x, y, t) = -\frac{A}{\omega \epsilon_1} (k_{SPP,y}^{(1)}, -k_{SPP,x}, 0) e^{i(k_{SPP,x}x + k_{SPP,y}^{(1)}y - \omega t)} \quad (\text{A.7a})$$

$$\vec{E}_{SPP}^{(2)}(x, y, t) = -\frac{B}{\omega \epsilon_2(\omega)} (-k_{SPP,y}^{(2)}, -k_{SPP,x}, 0) e^{i(k_{SPP,x}x - k_{SPP,y}^{(2)}y - \omega t)} \quad (\text{A.7b})$$

which equals to eqs. (A.7a) and (A.7b) in section 2.3.2

APPENDIX B

Threshold Regression Curve Algorithm

```
1 % Gaussian Threshold Fitting
2 clear
3 clc
4
5 n = 11; % number of data points
6 xlrage = ['R13:T' num2str(13+n-1)]; % load range
7 A = xlsread('...',1,xlrage); % load spreadsheet file
8 r = A(:,1);
9 p = A(:,2);
10 S = A(:,3);
11
12 NT = 0.19; % approximate threshold
13 NA = 0.35; % approximated radius
14
15 s = fitoptions('Method','NonlinearLeastSquares',...
16             'Lower',[-Inf,-Inf],...
17             'Upper',[Inf,Inf],...
18             'Startpoint',[NA NT]);
19 f = fittype('a*sqrt(0.5*log(x/b))','options',s);
20
21 %Fitting Function
22 [C,gof] = fit(p,r,f);
23
24 % Area Correction
25 Fitr = C.a;
26 FitTh = C.b;
27 R2 = gof.rsquare;
28 FitA = (24.15^2)*pi*1E-8 % measured spot area
29 FN = (2*(p/1000)/(FitA*1000));
30 FitThR = (2*(FitTh/1000)/(FitA*1000))
31 % New Fit
32 x = 0.2:0.001:0.45;
```




```
33 y = Fitr*sqrt(0.5*log(x/FitThR)); % best fit curve
34
35 % Graphing
36 figure(2)
37 errorbar(FN,r,S,'o')
38 hold on
39 plot(x,y,'r')
40 hold off
41 box off
42 axis([0 0.5 0 25])
43 set(gcf,'units','pixels','Position',[200,200,750,750])
44 set(gca,'FontSize',20)
45 xlabel('Fluence (J/cm^2)')
46 ylabel('Effective Radius (\mum)')
```

APPENDIX C

0-Dimensional Silicon Carrier Dynamics Calculation Algorithm

```
1 % Approximation to the Ultrafast Carrier Dynamics of Silicon
2 % 03/08/2017
3 % Assumptions:
4 % - 0D spatial system at peak fluence
5 % - Neglect carrier diffusion within pulse duration
6 % - Neglect thermal conduction (carrier thermalization) during ...
   pulse duration
7 % - Surface calculation only
8 % -- Neglect carrier dynamics below surface, Sokolowski-Tinten ...
   result
9 %     shows overestimation in reflectivity, may result in lower ...
   carrier
10 %     density in total
11 % - Ionization happens instantaneously
12 % - Two-temperature model
13 % - Assume constant carrier scatterign time
14 % - Assume degenerate semiconductor to begin with
15 % - Assume free electron gas model
16
17
18 %
19 %
20 %
21 % n1
22 % ----- y =0
23 % n2
24 %
25
26 clear
```



```

27 clc
28
29
30 % Global Parameters
31 ec = 1.602E-19; % electron charge (C)
32 me = 9.11E-31; % electron rest mass (Kg)
33 med = 1.08; % effective mass for density of states calculation
34 c = 2.998E8 ; % speed of light (m/s)
35 e0 = 8.854E-12; % vacuum permittivity (F/m)
36 h = 6.626E-34; % Planck's constant (m^2.Kg/s)
37 hbar = h/(2*pi); % modified Planck's constant (m^2.Kg/s)
38 kb = 8.617E-5; % Boltzmann constant eV/K
39
40 % Laser Parameters
41 lambda = 780E-9; % laser wavelength (m)
42 f = c/lambda; % laser frequency (Hz)
43 w = 2*pi*f; % laser angular frequency (Hz)
44 F0 = 0.6; % fluence (J/cm^2)
45 tp = 150E-15; % pulse width (s)
46 ainc = 0; % angle of incidence (deg)
47 I0 = F0*sqrt(4*log(2))/(tp*sqrt(pi())); % pulse peak intensity ...
    (W/cm^2)
48
49 % Materials Parameters
50 ed = 1; % dielectric medium permittivity
51 em0 = 13.764 + 0.056i; % initial permittivity (Constant for ...
    initialization)
52 a0 = 1208.3; % linear absorption coefficient (cm^-1)
53 b0 = 15.5; % two-photon absorption coefficient (cm/GW)
54 N0 = 2E23; % valence electron density (cm^-3)
55 n22 = 5E-15; % Kerr refractive index (cm^2/W)
56 mk = 3.22E-5; % slope of optical mass linear regression (K^-1)
57 Eg = 1.115; % band gap (eV)
58 td = 1.5E-15; % fs Drude carrier scattering time (s) (assumption)
59 Im = 21.2; % impact ionization coefficient (cm^2/J)
60
61 % Time Domain and Step
62 dt = 1; % time resolution (fs)
63 t = [-300:dt:250]*1E-15; % simulation time (s)
64 lt = length(t); % domain length
65 % energy integration range
66 Eint = [Eg:0.01:40]; % (eV)
67
68 % Parameters Initialization
69 em = 13.764 + 0.056i; % current silicon permittivity
70 Net = 1E16; % approximate initial carrier density (intrinsic) (cm^-3)
71 Te = 300; % electron temperature (K)
72
73 %% Chemical Potential (Parabolic DOS)
74 muint = [0.8:0.01:3]; % Chemical potential range for ...
    interpolation calculation (eV)
75 for k = 1:length(muint)
76     for j = 1:length(Eint)
77         nF(j) = ...

```

```

78         8*pi*sqrt(2)/h^3*(med*me)^1.5*sqrt(Eint(j)*ec-Eg*ec)*...
           1/(1+exp((Eint(j)-muint(k))/(kb*Te))); % Carrier ...
           density term
79     end
80     Ne3(k) = trapz(Eint*ec,nF)*1E-6; % integration
81 end
82 mu = interp1(Ne3,muint,Net,'linear'); % carrier chemical ...
           potential (eV)
83 %% Initial Carrier Heat Capacity
84 Teu = Te + 0.001*Te; % upper limit Te for differentiation (K)
85 Tel = Te - 0.001*Te; % lower limit Te for differentiation (K)
86 for ii = 1:length(Eint)
87     duel(ii) = ...
           8*pi*sqrt(2)/h^3*(med*me)^1.5*sqrt(Eint(ii)*ec-Eg*ec)*...
           (Eint(ii)*ec-Eg*ec)*1/(1+exp((Eint(ii)-mu)/(kb*Teu))); % ...
           Carrier density term
88     due2(ii) = ...
           8*pi*sqrt(2)/h^3*(med*me)^1.5*sqrt(Eint(ii)*ec-Eg*ec)*...
           (Eint(ii)*ec-Eg*ec)*1/(1+exp((Eint(ii)-mu)/(kb*Tel))); % ...
           Carrier density term
89 end
90 ue1 = trapz(Eint*ec,duel)*1E-6; % integration
91 ue2 = trapz(Eint*ec,due2)*1E-6; % integration
92 Ce = (ue1-ue2)/(Teu-Tel); % carrier heat capacity (J.cm^-3.K^-1)
93 %%
94 U = Net*Eg*ec + Ce*Te; % free carrier initial total energy ...
           density (J.cm^-3)
95 mopt = 0.144; % initial optical mass (mopt/me)
96 nm = sqrt((abs(em)+real(em))/2); % real part of refractive index ...
           of silicon
97 km = sqrt((abs(em)-real(em))/2); % imaginary part of refractive ...
           index of silicon
98 n1 = sqrt(ed); % refractive index of air/dielectric
99 n2 = nm + km*1i; % complex refractive index of silicon
100 rpb = (n1*sqrt(1-(n1/n2*sind(ainc))^2)-n2*cosd(ainc))/...
           (n1*sqrt(1-(n1/n2*sind(ainc))^2)+n2*cosd(ainc)); % Fresnel ...
           reflection coefficient
101 Rpb = abs(rpb).^2; % initial Fresnel reflectivity
102 It = I0*(1-Rpb(1))*exp(-4*log(2)*(t(1)/tp)^2); % initial ...
           intensity at the surface (W/cm^2)
103 E2 = It/(0.5*e0*c*real(n2)); % corresponding square electric ...
           field (V/cm^2)
104 aex = 4*pi()*km/(lambda*100); % effective absorption coefficient ...
           (includes fca and interband transitions) (cm^-1)
105 XR3 = 4/3*nm(1)^2*e0*c*n22; % real part of third order ...
           susceptibility (cm^2/V^2)
106 XI3 = 2/3*nm(1)^2*c^2*e0/w*b0*1E-7; % imaginary part of third ...
           order susceptibility (cm^2/V^2)
107 X3 = XR3 + XI3*1i; % third order susceptibility (cm^2/V^2)
108
109 % Calculation Loop
110 for i = 2:lt
111     % Intensity Function

```

```

116 It(i) = I0*(1-Rpb(i-1))*exp(-4*log(2)*(t(i)/tp)^2); % time ...
      dependent intensity (W/cm^2)
117 % Electric Field Magnitude
118 E2(i) = It(i)/(0.5*e0*c*real(n2(i-1))); % corresponding ...
      square electric field (V/cm^2)
119 % Absorbed Intensity
120 aex(i) = 4*pi()*km(i-1)/(lambda*100); % effective absorption ...
      coefficient (includes fca and interband transitions) (cm^-1)
121 du(i) = (aex(i)*It(i) + aex(i-1)*It(i-1))/2*dt*1E-15; % ...
      incremental absorbed energy density (J.cm^-3)
122 U(i) = U(i-1) + du(i); % total energy density in the carrier ...
      system (J.cm^-3)
123 % Carrier Density Calculation
124 Nei(i) = ((a0 + 1/2*b0*1E-9*It(i) + ...
      Im*Net(i-1)*(hbar*w))*It(i)/...
125      (hbar*w)+(a0 + 1/2*b0*1E-9*It(i-1) + ...
      Im*Net(i-1)*(hbar*w))*...
126      It(i-1)/(hbar*w))/2*dt*1E-15;
127 Net(i) = Net(i-1) + Nei(i);
128 % Chemical Potential (parabolic DOS)
129 EgS = 1.5E-8; % Band gap modification coefficient
130 Eg(i) = Eg(1) - EgS*Net(i)^(1/3); % modified (see van Driel 1986)
131 Eint = [Eg(i):0.01:40];
132 muint = [round(0.9*mu(i-1),2):0.01:round(1.1*mu(i-1),2)]; % ...
      Chemical potential range for interpolation calculation
133 for k = 1:length(muint)
134     for j = 1:length(Eint)
135         nF(j) = 8*pi*sqrt(2)/h^3*(med*me)^1.5*sqrt(Eint(j)*ec-...
136             Eg(i)*ec)*1/(1+exp((Eint(j)-muint(k))/...
137             (kb*Te(i-1)))); % Carrier density term
138     end
139     Ne4(k) = trapz(Eint*ec,nF)*1E-6; % integration
140 end
141 mu(i) = interp1(Ne4,muint,Net(i),'linear'); % carrier ...
      chemical potential (eV)
142 clear Ne4
143 % Carrier Heat Capacity
144 Teu = Te(i-1) + 0.001*Te(i-1); % upper limit Te for ...
      differentiation
145 Tel = Te(i-1) - 0.001*Te(i-1); % lower limit Te for ...
      differentiation
146 for ii = 1:length(Eint)
147     due1(ii) = 8*pi*sqrt(2)/h^3*(med*me)^1.5*sqrt(Eint(ii)*ec-...
148         Eg(i)*ec)*(Eint(ii)*ec-Eg(i)*ec)*1/(1+exp((Eint(ii)-...
149         mu(i))/(kb*Teu))); % Carrier density term
150     due2(ii) = 8*pi*sqrt(2)/h^3*(med*me)^1.5*sqrt(Eint(ii)*ec-...
151         Eg(i)*ec)*(Eint(ii)*ec-Eg(i)*ec)*1/(1+exp((Eint(ii)-...
152         mu(i))/(kb*Tel))); % Carrier density term
153 end
154 ue1 = trapz(Eint*ec,due1)*1E-6; % integration (J.cm^-3)
155 ue2 = trapz(Eint*ec,due2)*1E-6; % integration (J.cm^-3)
156 Ce(i) = (ue1-ue2)/(Teu-Tel); % carrier heat capacity ...
      (J.cm^-3.K^-1)
157 % Iterated Carrier Temperature

```

```

158 Te(i) = (U(i)-Net(i)*Eg(i)*ec)/Ce(i);
159 % Optical Mass
160 mopt(i) = mopt(1) + mk*Te(i); % no unit, linear regression ...
    from (Riffe 2001)
161 % Drude Model
162 eD = - Net(i)*1E6*ec^2/(e0*mopt(i)*me*w^2)*1/(1+li*(1/(w*td)));
163 % Non-Linear Susceptibility Term
164 eNL(i) = 3/4*X3(i-1)*E2(i);
165 % Total Permittivity
166 em(i) = em0 + eD + eNL(i);
167 % Reflectivity Recalculation
168 nm(i) = sqrt((abs(em(i))+real(em(i)))/2);
169 km(i) = sqrt((abs(em(i))-real(em(i)))/2);
170 n1 = sqrt(ed); % recalculated refractive index
171 n2(i) = nm(i) + km(i)*li; % recalculated refractive index
172 rpb = (n1*sqrt(1-(n1/n2(i)*sind(ainc))^2)-n2(i)*cosd(ainc))/...
173     (n1*sqrt(1-(n1/n2(i)*sind(ainc))^2)+n2(i)*cosd(ainc));
174 Rpb(i) = abs(rpb).^2; % recalculated reflectivity
175 XR3 = 4/3*nm(i)^2*e0*c*n22; % real part of third order ...
    susceptibility (cm^2/V^2)
176 XI3 = 2/3*nm(i)^2*c^2*e0/w*b0*1E-7; % imaginary part of ...
    third order susceptibility (cm^2/V^2)
177 X3(i) = XR3 + XI3*li; % third order susceptibility (cm^2/V^2)
178 comp = i/lt*100 % calculation completion percentage
179 end

```

APPENDIX D

Fast Fourier Transform and Autocorrelation Algorithms

1-D FFT Periodicity (Histogram)

```
1 clear
2 clc
3 I = imread('...tiff'); % load image file
4 I = rgb2gray(I); % grayscale conversion
5 I = im2double(I); % double precision conversion
6
7 [G1 G2] = size(I);
8 scale = 43/1024; % image scale (distance/pixels)
9 a = 440; % analysis window lower boundary
10 b = 500; % analysis window upper boundary
11
12 for i = 1:G1
13     c = I(i,:); % 1-D profile extraction (top to bottom)
14     c = c - 1.1*mean(c); % averaging function to -0
15     p = zeros(1,8192-length(c)); % zero-padding to specified length
16     c = horzcat(c,p);
17     Y = fft(c); % fft function
18     Y(1) = [];
19     N = length(Y);
20     YY = abs(Y(1:floor(N/2))).^2; nyquist = 1/2; % optimization ...
        sequence
21     f = (1:N/2)/(N/2)*nyquist; % optimization sequence
22     FF = scale./f; % frequency spectrum domain
23     eps = 0.00001;
```

```

24     pos = find(Y(a:b) ≥ max(Y(a:b))-eps); % peak finding
25     Ex(i) = FF(pos+a-1); % extracted periodicity
26 end
27
28 % visualization
29 figure(2)
30 edges = [650:3:850]; % period window (nm)
31 histogram(Ex*1000,edges, 'FaceColor', 'r', 'EdgeColor', 'k')
32 axis([650 850 0 100])
33 box off
34 set(gcf, 'units', 'pixels', 'Position', [200,200,500,300])
35 set(gca, 'FontSize', 20)
36 xlabel('Period (nm)')
37 ylabel('Counts')

```

2-D FFT Image

```

1 clear
2 clc
3
4 A = imread('....tif'); % load image file
5 A = rgb2gray(I); % grayscale conversion
6 A = im2double(I); % double precision conversion
7
8 scale = 43/1024; % image scale (distance/pixels)
9
10 % image size (pixels)
11 px = 128;
12 py = 128;
13
14 % FFT operation
15 rectshifted=fftshift(rect);
16 rectfft=fft2(rectshifted);
17 shiftedrectfft=fftshift(rectfft);
18 OPA = shiftedrectfft;
19
20 % axes position correction
21 [G1 G2]=find(max(max(abs(shiftedrectfft)))-1<abs(shiftedrectfft));
22 shiftedrectfft(G1,G2) = 0;
23 T = max(max(abs(shiftedrectfft)));
24 shiftedrectfft(G1,G2) = T;
25 OPB = shiftedrectfft;
26
27 % axes scaling
28 [H1 H2] = size(A);
29 y(G1) = 0;
30 x(G2) = 0;
31 y(G1+1:H1) = (1:(H1-G1))*1/scale/H1;
32 x(G2+1:H2) = (1:(H2-G2))*1/scale/H2;

```



```

33 y(1:G1-1) = fliplr(1:(G1-1))*-1/scale/H1;
34 x(1:G2-1) = fliplr(1:(G1-1))*-1/scale/H2;
35
36 K = 1; % normalization factor
37
38 % visualization
39 figure(5)
40 surf(x/K,-y/K,abs(OPB), 'LineStyle', 'none')
41 shading interp
42 set(gca,'zscale','log')
43 axis([-5 5 -5 5 0 10000])
44 set(gcf,'units','pixels','Position',[200,200,500,480])
45 set(gca,'box','off','FontSize',20)
46 xlabel('Normalized k_x')
47 ylabel('Normalized k_y')
48 view(0,90)

```

2-D Autocorrelation

```

1 clear
2 clc
3
4 A = imread('...tiff'); % load image file
5 A = im2double(A); % double precision conversion
6
7 scale = 2/94; % image scale (distance/pixels)
8 % image size and scaling
9 [n m] = size(A);
10 x = [1:1:m]*scale;
11 y = [1:1:n]*scale;
12
13 % Autocorrelation function
14 function B=autocorr2d(H)
15 [n m]=size(H); % image size
16 B=abs(fftshift(iff2(fft2(H).*conj(fft2(H)))))./(n*m);
17
18 B = autocorr2d(A);
19
20 % visualization
21 figure(3)
22 surf(x,y,B);
23 colormap gray
24 shading interp;
25 set(gcf,'units','pixels','Position',[200,200,500,476])
26 set(gca,'box','off','FontSize',20,'visible','off')
27 axis([0 3 0 3 0 100])
28 view(0,90)

```

APPENDIX E

Sipe Efficacy Factor Formalism

The efficacy factor $\eta(\vec{k}, \vec{k}_x)$ is defined as [25]:

$$\eta(\vec{k}, \vec{k}_x) = 2\pi |v(\vec{k}_+) + v^*(\vec{k}_-)| \quad (\text{E.1})$$

where $\vec{k}_\pm = \vec{k}_x \pm \vec{k}$ and \vec{k}_x is the beam wavevector component parallel to the surface (see fig. 2.2), which indirectly determine the incidence angle of the beam θ . The superscript (*) represents a complex conjugate. In the case of an s-polarized incident beam,

$$v(\vec{k}_\pm) = [h_{ss}(k_\pm)(\hat{k}_\pm \cdot \hat{x})^2 + h_{kk}(k_\pm)(\hat{k}_\pm \cdot \hat{y})^2] \gamma_t |t_s(k_x)|^2 \quad (\text{E.2})$$

while for a p-polarized incident beam,

$$\begin{aligned} v(\vec{k}_\pm) = & [h_{ss}(k_\pm)(\hat{k}_\pm \cdot \hat{y})^2 + h_{kk}(k_\pm)(\hat{k}_\pm \cdot \hat{x})^2] \gamma_t |t_x(k_x)|^2 \\ & + h_{kz}(k_\pm)(\hat{k}_\pm \cdot \hat{x}) \gamma_z \epsilon t_x^* t_z \\ & + h_{zk}(k_\pm)(\hat{k}_\pm \cdot \hat{x}) \gamma_t \epsilon t_z^* t_x \\ & + h_{zz}(k_\pm) \gamma_z \epsilon |t_z|^2 \end{aligned} \quad (\text{E.3})$$

Here, k_{\pm} and k_x are the norm of vector \vec{k}_{\pm} and \vec{k}_x , respectively. Meanwhile, the accent ($\hat{}$) represents a unit vector. The set of $h(k_{\pm})$ functions is given by

$$h_{ss}(k_{\pm}) = \frac{2i\nu}{\sqrt{\nu^2 - k_{\pm}^2} + \sqrt{\nu^2\epsilon - k_{\pm}^2}} \quad (\text{E.4})$$

$$h_{zz}(k_{\pm}) = \frac{2i}{\nu} \frac{\sqrt{\nu^2 - k_{\pm}^2} \sqrt{\nu^2\epsilon - k_{\pm}^2}}{\epsilon \sqrt{\nu^2 - k_{\pm}^2} + \sqrt{\nu^2\epsilon - k_{\pm}^2}} \quad (\text{E.5})$$

$$h_{kz}(k_{\pm}) = \frac{2ik_{\pm}}{\nu} \frac{\sqrt{\nu^2\epsilon - k_{\pm}^2}}{\epsilon \sqrt{\nu^2 - k_{\pm}^2} + \sqrt{\nu^2\epsilon - k_{\pm}^2}} \quad (\text{E.6})$$

$$h_{zk}(k_{\pm}) = \frac{2ik_{\pm}}{\nu} \frac{\sqrt{\nu^2 - k_{\pm}^2}}{\epsilon \sqrt{\nu^2 - k_{\pm}^2} + \sqrt{\nu^2\epsilon - k_{\pm}^2}} \quad (\text{E.7})$$

$$h_{zz}(k_{\pm}) = \frac{2ik_{\pm}^2}{\epsilon \sqrt{\nu^2 - k_{\pm}^2} + \sqrt{\nu^2\epsilon - k_{\pm}^2}} \quad (\text{E.8})$$

where ν is the norm of vector $2\pi/\lambda\vec{u}$. In our calculation we set ν to be 1 in order to normalized the frequency coordinate. In addition, ϵ denotes the complex permittivity of the material (in excited or unexcited states). The set of $t(k_{\pm})$ complex functions is defined as follows:

$$t_s(k_x) = \frac{2\sqrt{\nu^2 - k_x^2}}{\sqrt{\nu^2 - k_x^2} + \sqrt{\nu^2\epsilon - k_x^2}} \quad (\text{E.9})$$

$$t_x(k_x) = \frac{2}{\nu} \frac{\sqrt{\nu^2 - k_x^2} \sqrt{\nu^2\epsilon - k_x^2}}{\epsilon \sqrt{\nu^2 - k_x^2} + \sqrt{\nu^2\epsilon - k_x^2}} \quad (\text{E.10})$$

$$t_z(k_x) = \frac{2}{\nu} \frac{k_x \sqrt{\nu^2\epsilon - k_x^2}}{\epsilon \sqrt{\nu^2 - k_x^2} + \sqrt{\nu^2\epsilon - k_x^2}} \quad (\text{E.11})$$

The surface roughness is taken into account in parameters $\gamma_z(F, s)$ and $\gamma_t(F, s)$ and are given as follows:

$$\gamma_z(F, s) = \frac{1}{4\pi} \frac{\epsilon - 1}{\epsilon - (1 - F)(\epsilon - 1)(h(s) + Rh_i(s))} \quad (\text{E.12})$$

$$\gamma_t(F, s) = \frac{1}{4\pi} \frac{\epsilon - 1}{1 + \frac{1}{2}(1 - F)(\epsilon - 1)(h(s) - Rh_i(s))} \quad (\text{E.13})$$

where, the reflectivity R is expressed by:

$$R = \frac{\epsilon - 1}{\epsilon + 1} \quad (\text{E.14})$$

and the scalar functions $h(s)$ and $h_I(s)$ are given by:

$$h(s) = (s^2 + 1)^{1/2} - s \quad (\text{E.15})$$

$$h_I(s) = \frac{1}{2}[(s^2 + 4)^{1/2} + s] - (s^2 + 1)^{1/2} \quad (\text{E.16})$$

BIBLIOGRAPHY

BIBLIOGRAPHY

- [1] S. K. Sundaram and E. Mazur. Inducing and probing non-thermal transitions in semiconductors using femtosecond laser pulses. *Nature Materials*, 1(4):217–224, December 2002.
- [2] K. Sokolowski-Tinten and D. Von der Linde. Generation of dense electron-hole plasmas in silicon. *Physical Review B*, 61(4):2643, 2000.
- [3] P. P. Pronko, P. A. VanRompay, C. Horvath, F. Loesel, T. Juhasz, X. Liu, and G. Mourou. Avalanche ionization and dielectric breakdown in silicon with ultrafast laser pulses. *Physical Review B*, 58(5):2387–2390, August 1998.
- [4] Martin Schultze, Krupa Ramasesha, C. D. Pemmaraju, S. A. Sato, D. Whitmore, A. Gandman, James S. Prell, L. J. Borja, D. Prendergast, K. Yabana, Daniel M. Neumark, and Stephen R. Leone. Attosecond band-gap dynamics in silicon. *Science*, 346(6215):1348–1352, December 2014.
- [5] Muneaki Hase, Masayuki Katsuragawa, Anca Monia Constantinescu, and Hrvoje Petek. Frequency comb generation at terahertz frequencies by coherent phonon excitation in silicon. *Nature Photonics*, 6(4):243–247, April 2012.
- [6] Chao Lian, S. B. Zhang, and Sheng Meng. Ab initio evidence for nonthermal characteristics in ultrafast laser melting. *Physical Review B*, 94(18):184310, November 2016.
- [7] P. Stampfli and K. H. Bennemann. Theory for the instability of the diamond structure of Si, Ge, and C induced by a dense electron-hole plasma. *Physical Review B*, 42(11):7163–7173, October 1990.
- [8] E. N. Glezer, Y. Siegal, L. Huang, and E. Mazur. Laser-induced band-gap collapse in GaAs. *Physical Review B*, 51(11):6959, 1995.
- [9] A. M. Lindenberg, J. Larsson, K. Sokolowski-Tinten, K. J. Gaffney, C. Blome, O. Synnergren, J. Sheppard, C. Coleman, A. G. MacPhee, D. Weinstein, D. P. Lowney, T. K. Allison, T. Matthews, R. W. Falcone, A. L. Cavalieri, D. M. Fritz, S. H. Lee, P. H. Bucksbaum, D. A. Reis, J. Rudati, P. H. Fuoss, C. C. Kao, D. P. Siddons, R. Pahl, J. Als-Nielsen, S. Duesterer, R. Ischebeck, H. Schlarb, H. Schulte-Schrepping, Th Tschentscher, J. Schneider, D. von der Linde, O. Hignette, F. Sette, H. N. Chapman, R. W. Lee, T. N. Hansen, S. Techert, J. S. Wark, M. Bergh, G. Huldt, D. van der Spoel, N. Timneanu,

- J. Hajdu, R. A. Akre, E. Bong, P. Krejčík, J. Arthur, S. Brennan, K. Luening, and J. B. Hastings. Atomic-Scale Visualization of Inertial Dynamics. *Science*, 308(5720):392–395, April 2005.
- [10] V. I. Emel’yanov. Self-organization of ordered nano- and microstructures on the semiconductor surface under the action of laser radiation. *Laser Physics*, 18(6):682–718, June 2008.
- [11] Michael J. Abere, Ben Torralva, and Steven M. Yalisove. Periodic surface structure bifurcation induced by ultrafast laser generated point defect diffusion in GaAs. *Applied Physics Letters*, 108(15):153110, April 2016.
- [12] D.A. Reis, K.J. Gaffney, G.H. Gilmer, and B. Torralva. Ultrafast Dynamics of Laser-Excited Solids. *MRS Bulletin*, 31(08):601–606, August 2006.
- [13] Leonid V. Zhigilei, Zhibin Lin, and Dmitriy S. Ivanov. Atomistic Modeling of Short Pulse Laser Ablation of Metals: Connections between Melting, Spallation, and Phase Explosion. *The Journal of Physical Chemistry C*, 113(27):11892–11906, July 2009.
- [14] Yuanyuan Dong and Pal Molian. Coulomb explosion-induced formation of highly oriented nanoparticles on thin films of 3C–SiC by the femtosecond pulsed laser. *Applied Physics Letters*, 84(1):10–12, January 2004.
- [15] R. Stoian, D. Ashkenasi, A. Rosenfeld, and E. E. B. Campbell. Coulomb explosion in ultrashort pulsed laser ablation of Al_2O_3 . *Physical Review B*, 62(19):13167, November 2000.
- [16] J. Bonse, J. Krüger, S. Höhm, and A. Rosenfeld. Femtosecond laser-induced periodic surface structures. *Journal of Laser Applications*, 24(4):042006, 2012.
- [17] A. Borowiec and H. K. Haugen. Subwavelength ripple formation on the surfaces of compound semiconductors irradiated with femtosecond laser pulses. *Applied Physics Letters*, 82(25):4462, 2003.
- [18] Min Huang, Fuli Zhao, Ya Cheng, Ningsheng Xu, and Zhizhan Xu. Origin of Laser-Induced Near-Subwavelength Ripples: Interference between Surface Plasmons and Incident Laser. *ACS Nano*, 3(12):4062–4070, December 2009.
- [19] Jörn Bonse, Arkadi Rosenfeld, and Jörg Krüger. On the role of surface plasmon polaritons in the formation of laser-induced periodic surface structures upon irradiation of silicon by femtosecond-laser pulses. *Journal of Applied Physics*, 106(10):104910, 2009.
- [20] A. Y. Vorobyev and Chunlei Guo. Colorizing metals with femtosecond laser pulses. *Applied Physics Letters*, 92(4):041914, 2008.

- [21] Tommaso Baldacchini, James E. Carey, Ming Zhou, and Eric Mazur. Superhydrophobic Surfaces Prepared by Microstructuring of Silicon Using a Femtosecond Laser. *Langmuir*, 22(11):4917–4919, May 2006.
- [22] Ryan D. Murphy, Ben Torralva, David P. Adams, and Steven M. Yalisove. Polarization dependent formation of femtosecond laser-induced periodic surface structures near stepped features. *Applied Physics Letters*, 104(23):231117, June 2014.
- [23] Raúl Gago, Luis Vázquez, Rodolfo Cuerno, Mariá Varela, Carmen Ballesteros, and José Mariá Albella. Production of ordered silicon nanocrystals by low-energy ion sputtering. *Applied Physics Letters*, 78(21):3316–3318, May 2001.
- [24] N. V. Medhekar, W. L. Chan, V. B. Shenoy, and E. Chason. Stress-enhanced pattern formation on surfaces during low energy ion bombardment. *Journal of Physics: Condensed Matter*, 21(22):224021, 2009.
- [25] J. E. Sipe, Jeff F. Young, J. S. Preston, and H. M. Van Driel. Laser-induced periodic surface structure. I. Theory. *Physical Review B*, 27(2):1141, 1983.
- [26] L. Bányai, D. B. Tran Thoai, E. Reitsamer, H. Haug, D. Steinbach, M. U. Wehner, M. Wegener, T. Marschner, and W. Stolz. Exciton-LO-phonon quantum kinetics evidence of memory effects in bulk gaas. *Physical Review Letters*, 75(11):2188–2191, September 1995.
- [27] W. Z. Lin, R. W. Schoenlein, J. G. Fujimoto, and E. P. Ippen. Femtosecond absorption saturation studies of hot carriers in GaAs and AlGaAs. *IEEE Journal of Quantum Electronics*, 24(2):267–275, February 1988.
- [28] J. K. Chen, D. Y. Tzou, and J. E. Beraun. A semiclassical two-temperature model for ultrafast laser heating. *International Journal of Heat and Mass Transfer*, 49(1–2):307–316, January 2006.
- [29] Sergei I. Anisimov and Baerbel Rethfeld. Theory of ultrashort laser pulse interaction with a metal. In *Proceedings of SPIE*, volume 3093, pages 192–203, 1997.
- [30] B. Rethfeld, K. Sokolowski-Tinten, D. von der Linde, and S. I. Anisimov. Timescales in the response of materials to femtosecond laser excitation. *Applied Physics A*, 79(4-6):767–769, September 2004.
- [31] Lan Jiang and Hai-Lung Tsai. Improved Two-Temperature Model and Its Application in Ultrashort Laser Heating of Metal Films. *Journal of Heat Transfer*, 127(10):1167–1173, June 2005.
- [32] J. A. Kash, J. C. Tsang, and J. M. Hvam. Subpicosecond Time-Resolved Raman Spectroscopy of LO Phonons in GaAs. *Physical Review Letters*, 54(19):2151–2154, May 1985.

- [33] X. Y. Wang, D. M. Riffe, Y.-S. Lee, and M. C. Downer. Time-resolved electron-temperature measurement in a highly excited gold target using femtosecond thermionic emission. *Physical Review B*, 50(11):8016–8019, September 1994.
- [34] C. W White. *Laser and Electron Beam Processing of Materials*. Elsevier Science, Oxford, 1980. OCLC: 836401462.
- [35] N. Bloembergen. Pulsed Laser Interactions With Condensed Matter. *MRS Online Proceedings Library Archive*, 51, January 1985.
- [36] D von der Linde, K Sokolowski-Tinten, and J Bialkowski. Laser–solid interaction in the femtosecond time regime. *Applied Surface Science*, 109–110:1–10, February 1997.
- [37] J.A. Van Vechten, R. Tsu, and F.W. Saris. Nonthermal pulsed laser annealing of Si; plasma annealing. *Physics Letters A*, 74(6):422–426, December 1979.
- [38] J. A. Van Vechten, R. Tsu, F. W. Saris, and D. Hoonhout. Reasons to believe pulsed laser annealing of Si does not involve simple thermal melting. *Physics Letters A*, 74(6):417–421, December 1979.
- [39] C. V. Shank, R. Yen, and C. Hirlimann. Time-Resolved Reflectivity Measurements of Femtosecond-Optical-Pulse-Induced Phase Transitions in Silicon. *Physical Review Letters*, 50(6):454–457, February 1983.
- [40] M. C. Downer, R. L. Fork, and C. V. Shank. Femtosecond imaging of melting and evaporation at a photoexcited silicon surface. *JOSA B*, 2(4):595–599, April 1985.
- [41] C. V. Shank, R. Yen, and C. Hirlimann. Femtosecond-Time-Resolved Surface Structural Dynamics of Optically Excited Silicon. *Physical Review Letters*, 51(10):900–902, September 1983.
- [42] P. Saeta, J.-K. Wang, Y. Siegal, N. Bloembergen, and E. Mazur. Ultrafast electronic disordering during femtosecond laser melting of GaAs. *Physical Review Letters*, 67(8):1023–1026, August 1991.
- [43] H. W. K. Tom, G. D. Aumiller, and C. H. Brito-Cruz. Time-resolved study of laser-induced disorder of Si surfaces. *Physical Review Letters*, 60(14):1438–1441, April 1988.
- [44] Li Huang, J. Paul Callan, Eli N. Glezer, and Eric Mazur. GaAs under Intense Ultrafast Excitation: Response of the Dielectric Function. *Physical Review Letters*, 80(1):185–188, January 1998.
- [45] Y. Siegal, E. N. Glezer, and E. Mazur. Dielectric constant of GaAs during a subpicosecond laser-induced phase transition. *Physical Review B*, 49(23):16403–16406, June 1994.

- [46] J. P. Callan, A. M.-T. Kim, C. A. D. Roeser, and E. Mazur. Universal dynamics during and after ultrafast laser-induced semiconductor-to-metal transitions. *Physical Review B*, 64(7), July 2001.
- [47] K. Sokolowski-Tinten, J. Bialkowski, M. Boing, A. Cavalleri, and D. von der Linde. Thermal and nonthermal melting of gallium arsenide after femtosecond laser excitation. *Physical Review B*, 58(18):R11805–R11808, November 1998.
- [48] J. S. Graves and Roland E. Allen. Response of GaAs to fast intense laser pulses. *Physical Review B*, 58(20):13627, 1998.
- [49] Don H. Kim, H. Ehrenreich, and E. Runge. Band structure of femtosecond-laser-pulse excited GaAs. *Solid State Communications*, 89(2):119–122, January 1994.
- [50] K. Sokolowski-Tinten, J. Bialkowski, and D. von der Linde. Ultrafast laser-induced order-disorder transitions in semiconductors. *Physical Review B*, 51(20):14186–14198, May 1995.
- [51] D. H. Lowndes and G. E. Jellison. Chapter 6 Time-Resolved Measurements During Pulsed Laser Irradiation of Silicon. *Semiconductors and Semimetals*, 23:313–404, January 1984.
- [52] Neil W. Ashcroft and N. David Mermin. *Solid State Physics*. Holt, Rinehart and Winston, New York, 1976.
- [53] P. C. Becker, H. L. Fragnito, C. H. Brito Cruz, R. L. Fork, J. E. Cunningham, J. E. Henry, and C. V. Shank. Femtosecond Photon Echoes from Band-to-Band Transitions in GaAs. *Physical Review Letters*, 61(14):1647–1649, October 1988.
- [54] D. M. Riffe. Temperature dependence of silicon carrier effective masses with application to femtosecond reflectivity measurements. *JOSA B*, 19(5):1092–1100, May 2002.
- [55] Milton Birnbaum. Semiconductor Surface Damage Produced by Ruby Lasers. *Journal of Applied Physics*, 36(11):3688–3689, November 1965.
- [56] J. Bonse, S. Höhm, S. V. Kirner, A. Rosenfeld, and J. Krüger. Laser-Induced Periodic Surface Structures #x2014; A Scientific Evergreen. *IEEE Journal of Selected Topics in Quantum Electronics*, 23(3):1–15, May 2017.
- [57] Jeff F. Young, J. S. Preston, H. M. Van Driel, and J. E. Sipe. Laser-induced periodic surface structure. II. Experiments on Ge, Si, Al, and brass. *Physical Review B*, 27(2):1155, 1983.
- [58] R. J. Nemanich, D. K. Biegelsen, and W. G. Hawkins. Aligned, coexisting liquid and solid regions in laser-annealed Si. *Physical Review B*, 27(12):7817–7819, June 1983.

- [59] S. E. Clark and D. C. Emmony. Ultraviolet-laser-induced periodic surface structures. *Physical Review B*, 40(4):2031–2041, August 1989.
- [60] A. V. Demchuk and V. A. Labunov. Surface morphology and structure modification of silicon layers induced by nanosecond laser radiation. *Applied Surface Science*, 86(1):353–358, February 1995.
- [61] Y. F. Lu, W. K. Choi, Y. Aoyagi, A. Kinomura, and K. Fujii. Controllable laser-induced periodic structures at silicon–dioxide/silicon interface by excimer laser irradiation. *Journal of Applied Physics*, 80(12):7052, 1996.
- [62] P. M. Fauchet and A. E. Siegman. Observations of higher-order laser-induced surface ripples on $\langle 111 \rangle$ germanium. *Applied Physics A*, 32(3):135–140, 1983.
- [63] Zhou Guosheng, P. M. Fauchet, and A. E. Siegman. Growth of spontaneous periodic surface structures on solids during laser illumination. *Physical Review B*, 26(10):5366, 1982.
- [64] D. Ashkenasi, A. Rosenfeld, H. Varel, M. Wähler, and E. E. B. Campbell. Laser processing of sapphire with picosecond and sub-picosecond pulses. *Applied Surface Science*, 120(1):65–80, 1997.
- [65] J. Bonse, S. Baudach, J. Krüger, W. Kautek, and M. Lenzner. Femtosecond laser ablation of silicon—modification thresholds and morphology. *Applied Physics A*, 74(1):19–25, January 2002.
- [66] A.Y. Vorobyev and Chunlei Guo. Effects of nanostructure-covered femtosecond laser-induced periodic surface structures on optical absorptance of metals. *Applied Physics A*, 86(3):321–324, January 2007.
- [67] X.C. Wang, G.C. Lim, F.L. Ng, W. Liu, and S.J. Chua. Femtosecond pulsed laser-induced periodic surface structures on GaN/sapphire. *Applied Surface Science*, 252(5):1492–1497, December 2005.
- [68] Jörn Bonse, Arkadi Rosenfeld, and Jörg Krüger. Femtosecond laser-induced periodic surface structures: Recent approaches to explain their sub-wavelength periodicities. In Vladislav Panchenko, Gérard Mourou, and Aleksei M. Zheltikov, editors, *Proceedings of SPIE*, pages 79940M–79940M–10, September 2010.
- [69] F. Garrelie, J. P. Colombier, F. Pigeon, S. Tonchev, N. Faure, M. Bounhalli, S. Reynaud, and O. Parriaux. Evidence of surface plasmon resonance in ultrafast laser-induced ripples. *Optics Express*, 19(10):9035–9043, May 2011.
- [70] P. Audebert, Ph. Daguzan, A. Dos Santos, J. C. Gauthier, J. P. Geindre, S. Guizard, G. Hamoniaux, K. Krastev, P. Martin, G. Petite, and A. Antonetti. Space-time observation of an electron gas in SiO_2 . *Physical Review Letters*, 73(14):1990–1993, October 1994.

- [71] Quan Sun, Hongbing Jiang, Yi Liu, Zhaoxin Wu, Hong Yang, and Qihuang Gong. Measurement of the collision time of dense electronic plasma induced by a femtosecond laser in fused silica. *Optics Letters*, 30(3):320–322, February 2005.
- [72] Jürgen Reif, Florenta Costache, Matthias Henyk, and Stanislav V. Pandelov. Ripples revisited: Non-classical morphology at the bottom of femtosecond laser ablation craters in transparent dielectrics. *Applied Surface Science*, 197:891–895, 2002.
- [73] M. Rohloff, S. K. Das, S. Höhm, R. Grunwald, A. Rosenfeld, J. Krüger, and J. Bonse. Formation of laser-induced periodic surface structures on fused silica upon multiple cross-polarized double-femtosecond-laser-pulse irradiation sequences. *Journal of Applied Physics*, 110(1):014910, 2011.
- [74] S. Höhm, A. Rosenfeld, J. Krüger, and J. Bonse. Femtosecond laser-induced periodic surface structures on silica. *Journal of Applied Physics*, 112(1):014901, 2012.
- [75] J. E. Sipe, H. M. van Driel, and Jeff F. Young. Surface electrodynamics: Radiation fields, surface polaritons, and radiation remnants. *Canadian Journal of Physics*, 63:104, January 1985.
- [76] Ryan D. Murphy, Ben Torralva, David P. Adams, and Steven M. Yalisove. Laser-induced periodic surface structure formation resulting from single-pulse ultrafast irradiation of Au microstructures on a Si substrate. *Applied Physics Letters*, 102(21):211101, 2013.
- [77] V. R. Bhardwaj, P. P. Rajeev, P. B. Corkum, and D. M. Rayner. Strong field ionization inside transparent solids. *Journal of Physics B: Atomic, Molecular and Optical Physics*, 39(13):S397, 2006.
- [78] D. Dufft, A. Rosenfeld, S. K. Das, R. Grunwald, and J. Bonse. Femtosecond laser-induced periodic surface structures revisited: A comparative study on ZnO. *Journal of Applied Physics*, 105(3):034908, 2009.
- [79] Go Obara, Hisashi Shimizu, Taira Enami, Eric Mazur, Mitsuhiro Terakawa, and Minoru Obara. Growth of high spatial frequency periodic ripple structures on SiC crystal surfaces irradiated with successive femtosecond laser pulses. *Optics Express*, 21(22):26323–26334, November 2013.
- [80] Min Huang, Fuli Zhao, Ya Cheng, Ningsheg Xu, and Zhizhan Xu. Mechanisms of ultrafast laser-induced deep-subwavelength gratings on graphite and diamond. *Physical Review B*, 79(12), March 2009.
- [81] Takuro Tomita, Ryota Kumai, Shigeki Matsuo, Shuichi Hashimoto, and Makoto Yamaguchi. Cross-sectional morphological profiles of ripples on Si, SiC, and HOPG. *Applied Physics A*, 97(2):271–276, November 2009.

- [82] Feng Liang, Réal Vallée, and See Leang Chin. Mechanism of nanograting formation on the surface of fused silica. *Optics Express*, 20(4):4389–4396, February 2012.
- [83] E. M. Hsu, T. H. R. Crawford, C. Maunders, G. A. Botton, and H. K. Haugen. Cross-sectional study of periodic surface structures on gallium phosphide induced by ultrashort laser pulse irradiation. *Applied Physics Letters*, 92(22):221112, 2008.
- [84] V. R. Bhardwaj, E. Simova, P. P. Rajeev, C. Hnatovsky, R. S. Taylor, D. M. Rayner, and P. B. Corkum. Optically Produced Arrays of Planar Nanostructures inside Fused Silica. *Physical Review Letters*, 96(5), February 2006.
- [85] Xxx Sedao, Maxim V. Shugaev, Chengping Wu, Thierry Douillard, Claude Esnouf, Claire Maurice, Stéphanie Reynaud, Florent Pigeon, Florence Garrelie, Leonid V. Zhigilei, and Jean-Philippe Colombier. Growth Twinning and Generation of High-Frequency Surface Nanostructures in Ultrafast Laser-Induced Transient Melting and Resolidification. *ACS Nano*, 10(7):6995–7007, July 2016.
- [86] J. Bonse, M. Munz, and H. Sturm. Structure formation on the surface of indium phosphide irradiated by femtosecond laser pulses. *Journal of Applied Physics*, 97(1):013538, 2005.
- [87] N. Yasumaru, K. Miyazaki, and J. Kiuchi. Fluence dependence of femtosecond-laser-induced nanostructure formed on TiN and CrN. *Applied Physics A*, 81(5):933–937, October 2005.
- [88] R. Le Harzic, M. Menzel, S. Henning, A. Heilmann, F. Stracke, and H. Zimmermann. Cross-sectional study of high spatial frequency ripples performed on silicon using nanojoule femtosecond laser pulses at high repetition rate. *Applied Surface Science*, 305:670–673, June 2014.
- [89] R. Le Harzic, D. Dörr, D. Sauer, F. Stracke, and H. Zimmermann. Generation of high spatial frequency ripples on silicon under ultrashort laser pulses irradiation. *Applied Physics Letters*, 98(21):211905, 2011.
- [90] Juergen Reif, Olga Varlamova, Sergej Varlamov, and Michael Bestehorn. The role of asymmetric excitation in self-organized nanostructure formation upon femtosecond laser ablation. *Applied Physics A*, 104(3):969–973, September 2011.
- [91] Wai Lun Chan and Eric Chason. Making waves: Kinetic processes controlling surface evolution during low energy ion sputtering. *Journal of Applied Physics*, 101(12):121301, 2007.
- [92] Jonah Erlebacher, Michael J. Aziz, Eric Chason, Michael B. Sinclair, and Jerrold A. Floro. Spontaneous Pattern Formation on Ion Bombarded Si(001). *Physical Review Letters*, 82(11):2330–2333, March 1999.

- [93] Ari-David Brown, Jonah Erlebacher, Wai-Lun Chan, and Eric Chason. Transient Topographies of Ion Patterned Si(111). *Physical Review Letters*, 95(5), July 2005.
- [94] T. Q. Jia, H. X. Chen, M. Huang, F. L. Zhao, J. R. Qiu, R. X. Li, Z. Z. Xu, X. K. He, J. Zhang, and H. Kuroda. Formation of nanogratings on the surface of a ZnSe crystal irradiated by femtosecond laser pulses. *Physical Review B*, 72(12), September 2005.
- [95] F. Costache, S. Kouteva-Arguirova, and J. Reif. Sub damage threshold femtosecond laser ablation from crystalline Si: Surface nanostructures and phase transformation. *Applied Physics A*, 79(4-6), September 2004.
- [96] J. Bonse, S. Höhm, A. Rosenfeld, and J. Krüger. Sub-100-nm laser-induced periodic surface structures upon irradiation of titanium by Ti:sapphire femtosecond laser pulses in air. *Applied Physics A*, 110(3):547–551, March 2013.
- [97] R. Le Harzic, D. Dörr, D. Sauer, M. Neumeier, M. Epple, H. Zimmermann, and F. Stracke. Large-area, uniform, high-spatial-frequency ripples generated on silicon using a nanojoule-femtosecond laser at high repetition rate. *Optics letters*, 36(2):229–231, 2011.
- [98] R. Le Harzic, F. Stracke, and H. Zimmermann. Formation mechanism of femtosecond laser-induced high spatial frequency ripples on semiconductors at low fluence and high repetition rate. *Journal of Applied Physics*, 113(18):183503, 2013.
- [99] Max Born and Emil Wolf. *Principles of Optics: Electromagnetic Theory of Propagation, Interference and Diffraction of Light*. Cambridge University Press, Cambridge ; New York, 7th expanded ed edition, 1999.
- [100] H. Raether. *Surface Plasmons on Smooth and Rough Surfaces and on Gratings*, volume 111 of *Springer Tracts in Modern Physics*. Springer Berlin Heidelberg, 1988.
- [101] Anatoly V. Zayats, Igor I. Smolyaninov, and Alexei A. Maradudin. Nano-optics of surface plasmon polaritons. *Physics Reports*, 408(3-4):131–314, March 2005.
- [102] Ryan D. Murphy. *Femtosecond Laser Interactions at Interfaces and Their Applications*. PhD thesis, University of Michigan, 2013.
- [103] K. Sokolowski-Tinten, J. Bialkowski, A. Cavalleri, D. Von der Linde, A. Oparin, J. Meyer-ter Vehn, and S. I. Anisimov. Transient states of matter during short pulse laser ablation. *Physical Review Letters*, 81(1):224, 1998.
- [104] J. M. Liu. Simple technique for measurements of pulsed Gaussian-beam spot sizes. *Optics Letters*, 7(5):196–198, May 1982.

- [105] Robert W. Boyd. *Nonlinear Optics*. Academic Press, Amsterdam ; Boston, 3rd ed edition, 2008.
- [106] <http://www.as-photonics.com/snlo>.
- [107] Zuofei Hong, Qingbin Zhang, and Peixiang Lu. Compact dual-crystal optical parametric amplification for broadband IR pulse generation using a collinear geometry. *Optics Express*, 21(8):9491–9504, April 2013.
- [108] K.R. Williams, K. Gupta, and M. Wasilik. Etch rates for micromachining processing-part II. *Journal of Microelectromechanical Systems*, 12(6):761–778, December 2003.
- [109] M. Morita, T. Ohmi, E. Hasegawa, M. Kawakami, and M. Ohwada. Growth of native oxide on a silicon surface. *Journal of Applied Physics*, 68(3):1272, 1990.
- [110] D Eaglesham. 370 °C clean for Si molecular beam epitaxy using a HF dip. *Applied Physics Letters*, 59(6):685–687, August 1991.
- [111] M. Hersam. Atomic-level study of the robustness of the Si(100)-2×1:H surface following exposure to ambient conditions. *Applied Physics Letters*, 78(7):886–888, February 2001.
- [112] Dev Alok and B. J. Baliga. A novel method for etching trenches in silicon carbide. *Journal of Electronic Materials*, 24(4):311–314, April 1995.
- [113] Christopher S. Roper, Roger T. Howe, and Roya Maboudian. Room-Temperature Wet Etching of Polycrystalline and Nanocrystalline Silicon Carbide Thin Films with HF and HNO₃. *Journal of The Electrochemical Society*, 156(3):D104–D107, January 2009.
- [114] <http://www.ehs.columbia.edu/hydrofluoricacid.pdf>.
- [115] T. E. Orlowski and H. Richter. Ultrafast laser-induced oxidation of silicon: A new approach towards high quality, low-temperature, patterned SiO₂ formation. *Applied Physics Letters*, 45(3):241–243, August 1984.
- [116] Edward D. Palik and Gorachand Ghosh, editors. *Handbook of Optical Constants of Solids*. Academic Press, San Diego, 1998.
- [117] Simin Feng and Herbert G. Winful. Physical origin of the Gouy phase shift. *Optics letters*, 26(8):485–487, 2001.
- [118] Richard Lee Sutherland, Daniel Garth McLean, and Sean Kirkpatrick. *Handbook of Nonlinear Optics*. Number 82 in Optical engineering. Marcel Dekker, New York, 2nd ed., rev. and expanded edition, 2003.
- [119] Alan Bristow. Two-photon absorption and Kerr coefficients of silicon for 850–2200nm. *Applied Physics Letters*, 90(19):191104, May 2007.

- [120] A. J. Sabbah and D. M. Riffe. Femtosecond pump-probe reflectivity study of silicon carrier dynamics. *Physical Review B*, 66(16), October 2002.
- [121] D P Korfiatis, K-A Th Thoma, and J C Vardaxoglou. Conditions for femtosecond laser melting of silicon. *Journal of Physics D: Applied Physics*, 40(21):6803–6808, November 2007.
- [122] D. H. Reitze, T. R. Zhang, Wm M. Wood, and M. C. Downer. Two-photon spectroscopy of silicon using femtosecond pulses at above-gap frequencies. *JOSA B*, 7(1):84–89, January 1990.
- [123] Waldemar Kuett, Anton Esser, Klaus Seibert, Uli Lemmer, and Heinrich Kurz. Femtosecond studies of plasma formation in crystalline and amorphous silicon. In *Proceedings of SPIE*, volume 1268, pages 154–165, 1990.
- [124] J Bonse, K.-W Brzezinka, and A.J Meixner. Modifying single-crystalline silicon by femtosecond laser pulses: An analysis by micro Raman spectroscopy, scanning laser microscopy and atomic force microscopy. *Applied Surface Science*, 221(1-4):215–230, January 2004.
- [125] Hao Zhang, S. A. Wolbers, D. M. Krol, J. I. Dijkhuis, and D. van Oosten. Modeling and experiments of self-reflectivity under femtosecond ablation conditions. *JOSA B*, 32(4):606–616, April 2015.
- [126] B. C. Stuart, M. D. Feit, S. Herman, A. M. Rubenchik, B. W. Shore, and M. D. Perry. Nanosecond-to-femtosecond laser-induced breakdown in dielectrics. *Physical Review B*, 53(4):1749–1761, January 1996.
- [127] Monique Combescot and Roland Combescot. Conductivity relaxation time due to electron-hole collisions in optically excited semiconductors. *Physical Review B*, 35(15):7986–7992, May 1987.
- [128] Bo E. Sernelius. Intraband relaxation time in highly excited semiconductors. *Physical Review B*, 43(9):7136–7144, March 1991.
- [129] D. Hulin, M. Combescot, J. Bok, A. Migus, J. Y. Vinet, and A. Antonetti. Energy Transfer during Silicon Irradiation by Femtosecond Laser Pulse. *Physical Review Letters*, 52(22):1998–2001, May 1984.
- [130] H. M. Van Driel. Optical effective mass of high density carriers in silicon. *Applied Physics Letters*, 44(6):617–619, March 1984.
- [131] Guo-Zhen Yang and N. Bloembergen. Effective mass in picosecond laser-produced high-density plasma in silicon. *IEEE Journal of Quantum Electronics*, 22(1):195–196, January 1986.
- [132] J. Leuthold, C. Koos, and W. Freude. Nonlinear silicon photonics. *Nature Photonics*, 4(8):535–544, August 2010.

- [133] Q. Lin, Oskar J. Painter, and Govind P. Agrawal. Nonlinear optical phenomena in silicon waveguides: Modeling and applications. *Optics Express*, 15(25):16604–16644, 2007.
- [134] P. A. Wolff. Theory of the Band Structure of Very Degenerate Semiconductors. *Physical Review*, 126(2):405–412, April 1962.
- [135] A. Oschlies, R. W. Godby, and R. J. Needs. First-principles self-energy calculations of carrier-induced band-gap narrowing in silicon. *Physical Review B*, 45(23):13741–13744, June 1992.
- [136] Henry M. van Driel. Kinetics of high-density plasmas generated in Si by 1.06- and 0.53- μm picosecond laser pulses. *Physical Review B*, 35(15):8166–8176, May 1987.
- [137] S.M. Goodnick. Subpicosecond dynamics of electron injection into GaAs/Al-GaAs quantum wells. *Applied Physics Letters*, 51(8):584–586, August 1987.
- [138] W. H. Knox, D. S. Chemla, G. Livescu, J. E. Cunningham, and J. E. Henry. Femtosecond Carrier Thermalization in Dense Fermi Seas. *Physical Review Letters*, 61(11):1290–1293, September 1988.
- [139] Ellen J. Yoffa. Screening of hot-carrier relaxation in highly photoexcited semiconductors. *Physical Review B*, 23(4):1909–1919, February 1981.
- [140] Ryan D. Murphy, Ben Torralva, David P. Adams, and Steven M. Yalisove. Pump-probe imaging of laser-induced periodic surface structures after ultrafast irradiation of Si. *Applied Physics Letters*, 103(14):141104, 2013.
- [141] Pier Luigi Silvestrelli, Ali Alavi, Michele Parrinello, and Daan Frenkel. Ab initio Molecular Dynamics Simulation of Laser Melting of Silicon. *Physical Review Letters*, 77(15):3149–3152, October 1996.
- [142] J. Bonse, A. Rosenfeld, and J. Krüger. Implications of transient changes of optical and surface properties of solids during femtosecond laser pulse irradiation to the formation of laser-induced periodic surface structures. *Applied Surface Science*, 257(12):5420–5423, April 2011.
- [143] Howard R. Stuart and Dennis G. Hall. Island size effects in nanoparticle-enhanced photodetectors. *Applied Physics Letters*, 73(26):3815–3817, December 1998.
- [144] D. M. Schaadt, B. Feng, and E. T. Yu. Enhanced semiconductor optical absorption via surface plasmon excitation in metal nanoparticles. *Applied Physics Letters*, 86(6):063106, February 2005.
- [145] C. Fourment, F. Deneuille, D. Descamps, F. Dorchies, S. Petit, O. Peyrusse, B. Holst, and V. Recoules. Experimental determination of temperature-dependent electron-electron collision frequency in isochorically heated warm dense gold. *Physical Review B*, 89(16):161110, April 2014.

- [146] J. Zhang, L. Zhang, and W. Xu. Surface plasmon polaritons: Physics and applications. *Journal of Physics D: Applied Physics*, 45(11):113001, March 2012.
- [147] H.A. Jamid and S.J. Al-Bader. Reflection and transmission of surface plasmon mode at a step discontinuity. *IEEE Photonics Technology Letters*, 9(2):220–222, February 1997.
- [148] J. Krüger, D. Dufft, R. Koter, and A. Hertwig. Femtosecond laser-induced damage of gold films. *Applied Surface Science*, 253(19):7815–7819, July 2007.
- [149] F. Korte, J. Koch, and B.N. Chichkov. Formation of microbumps and nanojets on gold targets by femtosecond laser pulses. *Applied Physics A*, 79(4-6), September 2004.
- [150] V. K. Valev, D. Denkova, X. Zheng, A. I. Kuznetsov, C. Reinhardt, B. N. Chichkov, G. Tsutsumanova, E. J. Osley, V. Petkov, B. De Clercq, A. V. Silhanek, Y. Jeyaram, V. Volskiy, P. A. Warburton, G. A. E. Vandenbosch, S. Russev, O. A. Aktsipetrov, M. Ameloot, V. V. Moshchalkov, and T. Verbiest. Plasmon-Enhanced Sub-Wavelength Laser Ablation: Plasmonic Nanojets. *Advanced Materials*, 24(10):OP29–OP35, March 2012.
- [151] Claudia Unger, Jrgen Koch, Ludger Overmeyer, and Boris N. Chichkov. Time-resolved studies of femtosecond-laser induced melt dynamics. *Optics express*, 20(22):24864–24872, 2012.
- [152] A. I. Kuznetsov, J. Koch, and B. N. Chichkov. Laser-induced backward transfer of gold nanodroplets. *Optics Express*, 17(21):18820–18825, October 2009.
- [153] M. Bonn, D. N. Denzler, S. Funk, M. Wolf, S.-Svante Wellershoff, and J. Hohlfeld. Ultrafast electron dynamics at metal surfaces: Competition between electron-phonon coupling and hot-electron transport. *Physical Review B*, 61(2):1101, 2000.
- [154] C. Xie, X. Li, K. Liu, M. Zhu, R. Qiu, and Q. Zhou. Direct writing of sub-wavelength ripples on silicon using femtosecond laser at high repetition rate. *Applied Surface Science*, 360, Part B:896–903, January 2016.
- [155] R. Le Harzic, H. Schuck, D. Sauer, T. Anhut, I. Riemann, and K. König. Sub-100 nm nanostructuring of silicon by ultrashort laser pulses. *Optics Express*, 13(17):6651–6656, August 2005.
- [156] G. Daminelli, J. Krüger, and W. Kautek. Femtosecond laser interaction with silicon under water confinement. *Thin Solid Films*, 467(1–2):334–341, November 2004.
- [157] G. Miyaji, K. Miyazaki, K. Zhang, T. Yoshifuji, and J. Fujita. Mechanism of femtosecond-laser-induced periodic nanostructure formation on crystalline silicon surface immersed in water. *Optics express*, 20(14):14848–14856, 2012.

- [158] M. Straub, M. Afshar, D. Feili, H. Seidel, and K. König. Surface plasmon polariton model of high-spatial frequency laser-induced periodic surface structure generation in silicon. *Journal of Applied Physics*, 111(12):124315, June 2012.
- [159] Maher Harb, Ralph Ernstorfer, Christoph T. Hebeisen, Germán Sciaini, Weina Peng, Thibault Dartigalongue, Mark A. Eriksson, Max G. Lagally, Sergei G. Kruglik, and R. J. Dwayne Miller. Electronically Driven Structure Changes of Si Captured by Femtosecond Electron Diffraction. *Physical Review Letters*, 100(15):155504, April 2008.
- [160] J. B. Renucci, R. N. Tyte, and M. Cardona. Resonant Raman scattering in silicon. *Physical Review B*, 11(10):3885–3895, May 1975.
- [161] NuoFu Chen, Yutian Wang, Hongjia He, and Lanying Lin. Effects of point defects on lattice parameters of semiconductors. *Physical Review B*, 54(12):8516–8521, September 1996.
- [162] D. Bäuerle. *Laser Processing and Chemistry*. Springer, Heidelberg ; New York, fourth edition edition, 2011.
- [163] P. L. Liu, R. Yen, N. Bloembergen, and R. T. Hodgson. Picosecond laser-induced melting and resolidification morphology on Si. *Applied Physics Letters*, 34(12):864–866, June 1979.
- [164] M. J. Abere, C. Chen, D. R. Rittman, M. Kang, R. S. Goldman, J. D. Phillips, B. Torralva, and S. M. Yalisove. Nanodot formation induced by femtosecond laser irradiation. *Applied Physics Letters*, 105(16):163103, October 2014.
- [165] S. Facsko, T. Dekorsy, C. Koerdt, C. Trappe, H. Kurz, A. Vogt, and H. L. Hartnagel. Formation of Ordered Nanoscale Semiconductor Dots by Ion Sputtering. *Science*, 285(5433):1551–1553, September 1999.
- [166] F. Frost, A. Schindler, and F. Bigl. Roughness Evolution of Ion Sputtered Rotating InP Surfaces: Pattern Formation and Scaling Laws. *Physical Review Letters*, 85(19):4116, November 2000.
- [167] F. Frost, B. Ziberi, A. Schindler, and B. Rauschenbach. Surface engineering with ion beams: From self-organized nanostructures to ultra-smooth surfaces. *Applied Physics A*, 91(4):551–559, June 2008.
- [168] Mario Castro, Rodolfo Cuerno, Luis Vázquez, and Raúl Gago. Self-Organized Ordering of Nanostructures Produced by Ion-Beam Sputtering. *Physical Review Letters*, 94(1):016102, January 2005.
- [169] W. L. Chan and E. Chason. Stress evolution and defect diffusion in Cu during low energy ion irradiation: Experiments and modeling. *Journal of Vacuum Science & Technology A: Vacuum, Surfaces, and Films*, 26(1):44–51, January 2008.

- [170] Gozde Ozaydin, Karl F. Ludwig, Hua Zhou, and Randall L. Headrick. Effects of Mo seeding on the formation of Si nanodots during low-energy ion bombardment. *Journal of Vacuum Science & Technology B: Microelectronics and Nanometer Structures*, 26(2):551, 2008.
- [171] J. Byskov-Nielsen, J. Savolainen, M. S. Christensen, and P. Balling. Ultra-short pulse laser ablation of metals: Threshold fluence, incubation coefficient and ablation rates. *Applied Physics A*, 101(1):97–101, October 2010.
- [172] A. Rosenfeld, M. Lorenz, R. Stoian, and D. Ashkenasi. Ultrashort-laser-pulse damage threshold of transparent materials and the role of incubation. *Applied Physics A: Materials Science & Processing*, 69(7):S373–S376, December 1999.
- [173] D. Mathiot, J. P. Schunck, M. Perego, M. Fanciulli, P. Normand, C. Tsamis, and D. Tsoukalas. Silicon self-diffusivity measurement in thermal SiO₂ by ³⁰Si/²⁸Si isotopic exchange. *Journal of Applied Physics*, 94(3):2136–2138, July 2003.
- [174] David J. Fisher, editor. *Diffusion in Silicon: 10 Years of Research*. Number 153/155 in Diffusion and defect data Pt. A, Defect and diffusion forum. Scitec, Zuerich-Uetikon, 1998. OCLC: 246106740.
- [175] Jeff F. Young, J. E. Sipe, and H. M. Van Driel. Laser-induced periodic surface structure. III. Fluence regimes, the role of feedback, and details of the induced topography in germanium. *Physical Review B*, 30(4):2001, 1984.
- [176] J. T. Foley and U. Landman. Model dielectric function for semiconductors: Si. *Physical Review B*, 14(4):1597, August 1976.
- [177] P. A. Stolk, H.-J. Gossmann, D. J. Eaglesham, D. C. Jacobson, C. S. Rafferty, G. H. Gilmer, M. Jaraíz, J. M. Poate, H. S. Luftman, and T. E. Haynes. Physical mechanisms of transient enhanced dopant diffusion in ion-implanted silicon. *Journal of Applied Physics*, 81(9):6031–6050, May 1997.
- [178] T. E. Orłowski and D. A. Mantell. Ultraviolet laser-induced oxidation of silicon: The effect of oxygen photodissociation upon oxide growth kinetics. *Journal of Applied Physics*, 64(9):4410–4414, November 1988.
- [179] B. E. Deal and A. S. Grove. General Relationship for the Thermal Oxidation of Silicon. *Journal of Applied Physics*, 36(12):3770–3778, December 1965.
- [180] Hisashi Shimizu, Shuhei Yada, Go Obara, and Mitsuhiro Terakawa. Contribution of defect on early stage of LIPSS formation. *Optics Express*, 22(15):17990–17998, July 2014.
- [181] Michael A. Capano. Time-of-flight analysis of the plume dynamics of laser-ablated 6H-silicon carbide. *Journal of Applied Physics*, 78(7):4790–4792, October 1995.